© 2012 Seung Jun Kim

AN EXPERIMENTAL STUDY OF CRITICAL HEAT FLUX WITH SURFACE MODIFICATION AND ITS ANALYTIC PREDICTION MODEL DEVELOPMENT

BY

SEUNG JUN KIM

DISSERTATION

Submitted in partial fulfillment of the requirements
for the degree of Doctor of Philosophy in Nuclear Engineering
in the Graduate College of the
University of Illinois at Urbana-Champaign, 2012

Urbana, Illinois

Doctoral Committee:

Emeritus Professor Barclay G. Jones, Chair
Emeritus Professor Ty A. Newell
Professor Roy A. Axford
Professor Rizwan Uddin

ABSTRACT

The critical heat flux (CHF) condition causes a drastic reduction of heat transfer coefficient and sometimes involves physical failure of the heating surface in heat flux-controlled systems. Understanding of CHF phenomena and reliable CHF prediction model development are necessary to design various heat transfer systems including nuclear fission reactors, fossil-fueled boilers, thermo-nuclear fusion reactors, etc. Many aspects of CHF phenomena are well understood and reasonable prediction models have been developed. However, due to the complex natures of phenomena, CHF in sub-cooled flow boiling is still an active research topic. This experimental study examines the effects of various operating system conditions including; system pressure, mass flow rate, sub-cooled temperature, and surface wettability upon CHF under sub-cooled flow boiling conditions. An analytical CHF prediction model also has been proposed using the bubble force balance. Sub-cooled flow boiling is generally characterized by high heat transfer rate and low wall superheat, which is essential for cooling applications requiring high heat transfer rates, such as in nuclear reactors and fossil power plants.

In this study, sub-cooled flow boiling tests were conducted using R-134a coolant in a rectangular channel (half inch by half inch) with one uniformly heated surface. This is a surface heat flux controlled system. This refrigerant is selected as a stimulant fluid for water due to its small surface tension, low latent heat, and low boiling temperature. The

experiments were conducted under the following conditions: (1) inlet pressure (P) of 400 ~ 800 KPa, (2) specific mass flow rate (G) of 124 ~ 248 kg/m^2-s, (3) inlet sub-cooling enthalpy (ΔH_i) of 9 ~ 45kJ/kg. By varying experimental operating conditions, CHF was identified by monitoring a sudden rise in heated wall temperature. It was found that CHF in a rectangular channel increases with increasing mass flow rate, increasing inlet sub-cooling, and increasing system pressure. The parametric trend of the CHF data using R-134a in a rectangular channel is consistent with classic understanding of CHF in round tubes using water in relatively low pressure (less than 0.2 reduced pressures). In addition, a Fluid-to-Fluid scaling model was utilized to convert the test data obtained in the simulant fluid (R-134a) into the prototypical fluid (water). The comparison between the converted CHF of equivalent water and CHF look-up table with same operation conditions were conducted, and show good agreement.

In order to investigate heating surface feature effects on CHF, surface modification, applying Atmospheric Pressure Plasma (AP-Plasma) coating, was performed on the copper heating block. It is considered that the AP-Plasma treated surface does not affect boiling heat transfer directly, but rather via change in microscopic surface parameters such as wettability and static contact angle, parameters that the proposed CHF prediction model incorporates. The surface oxidation coating with AP-Plasma makes the surface features (static contact angle, oxidation layer thickness) become more hydrophilic and reduces the static contact angle from 80˚ to 10˚. 10~18% of CHF enhancement under flow boiling

conditions were found with AP-Plasma treated heating surfaces compared to those of non-treated heating surfaces. To understand the different flow boiling characteristics on these modified heating surfaces, the surface features such as static contact angle at the solid-fluid interface, the coating layer thickness were observed and measured for different experimental conditions utilizing advanced goniometer [Rame-hart model 500] and oxidation layer thickness measurement device [Sloan Dektak^3]. Liquid droplet contact angle reduction by AP-Plasma indicated that an 80˚ static contact angle with pure copper block and a 10˚ static contact angle with AP-Plasma treated surface. The thickness of oxidation layer ranges from 1 to 3 micro meters.

The analytic CHF prediction model based on physical bubble force balance with consideration of surface characteristics is also developed in this study. A comparative study of the proposed model with a previous model (Katto et al., 1984) was conducted over the range of the current experimental conditions. The Katto model predicts the CHF within 30% of maximum deviation for current experiment CHF data; however, the proposed model predicts the CHF within only 8% maximum deviation. In order to validate with other researcher's CHF measurement, author's proposed model is utilized to predict the CHF value with various operating conditions (total number of 155 CHF data points: working fluid: R134-a, water, Freon-113, FC72) provided by different research group's experimental CHF data. It shows good agreement. This proposed analytical model is the first correlation incorporating the surface feature variable (Static contact angle) into the CHF prediction in

flow boiling conditions. In current experimental tests, as the contact angle becomes smaller, the CHF become enhanced in flow boiling conditions. The surface wettability effect on CHF observed in experimental test (AP-Plasma treated surface vs. Non-treated surface) is well captured in analytical CHF prediction model.

Devoted to my beloved wife and two boys

Acknowledgements

I would like to express my sincere gratitude to my academic advisor, and committee chair, Professor Barclay G. Jones for unconditional support, inspiring discussions, and excellent advising with thoughtful encouragement that he gave me throughout the course work and PhD research. Without his help and guideline, I can imagine that this research would not have been completed. I would like to thank Dr. Ty A. Newell for his support on experimental facilities and his guidance on my thesis work. I would also like to express special thanks to Professor Roy A. Axford and Professor Rizwan Uddin for being my committee members and providing insights into several aspects of the problem on this research. A special thank goes to CFD division at Caterpillar-CSC and Dr Marsh at CERL for RA supporting on conducting PhD program. I would like to extend appreciation to colleagues – Dr. Ling Zou and Dr. Hyunjong Joe - for useful discussions and friendship here at the department. I would like to acknowledge all the faculties and staff of the NPRE for their enormous support, assistance, and understanding.

Finally, this work is dedicated to my wife, Min-sung, and my sons, Hyunoo and Jinoo. Without their supporting, long patience, and encouragement, my PhD work would never have been completed. I also wish to express my thanks to my family in South Korea for their support and encouragement.

TABLE OF CONTENTS

1. INTRODUCTION 1

1.1 Background and Motivation 1

1.2 Critical heat flux (CHF) in Sub-cooled Flow Boiling 2

1.3 Objectives and Scope 6

References 8

2. LITERATURE REVIEW 9

2.1 Characteristics of Sub-cooled Flow Boiling CHF 9

2.1.1 Boundary layer separation model (Hydrodynamic instability theory) 11

2.1.2 Bubble crowding model 12

2.1.3 Sub-layer (Macro layer) dryout model 14

2.1.4 Dry-spot model (Wall overheat theory) 15

2.2 Parametric Effects on CHF in Sub-cooled Flow Boiling 17

2.3 CHF Visualization Experiments and CHF Flow Regime Map 22

2.4 Prediction of CHF 25

2.4.1 Analytical prediction models 25

2.4.2 Empirical prediction models 30

2.4.3 Fluid-to-fluid scaling CHF prediction method 32

2.5 Enhancement of CHF 35

2.5.1 Nano-fluid application for CHF enhancement 36

2.5.2 Surface modification application for CHF enhancement 39

Nomenclature....41

References....43

3. EXPERIMENTAL DESCRIPTIONS....47

3.1 Sub-cooled Flow Boiling Experimental Test Facility....47

3.1.1 Overall test loop configuration....49

3.1.2 Test section....50

3.1.3 Data acquisition and flow visualization systems....57

3.2 Experimental Operating Conditions and Uncertainty Analysis....60

3.2.1 Experimental operating conditions....60

3.2.2 The uncertainty analysis and experimental condition....63

3.3 Surface Treatment (Atmospheric Pressure (AP) Plasma Coating)....65

3.2.1 Atmospheric pressure plasma coating....65

3.2.2 Contact angle measurement (surface wettability measurement)....68

3.2.3 Coating layer thickness measurement (Dektak stylus profilometer)....70

Nomenclature....72

References....73

4. EXPERIMENTAL RESULT....74

4.1 Critical heat flux (CHF) Measurement and Parametric Trend Study....74

4.1.1 Effect of sub-cooling inlet temperature on CHF....78

4.1.2 Effect of mass flux on CHF....82

4.1.3 Effect of system pressure on CHF....84

4.1.4 An empirical CHF prediction correlation based on R-134a flow boiling CHF experimental data 87

4.2 R134a-water Scaling Method and Comparison Work 92

4.2.1 Fluid-to-fluid scaling method of CHF 93

4.2.2 Comparison work between equivalent water CHF data and look-up table 97

Nomenclature 102

References 103

5. MODEL DEVELOPMENT AND VALIDATION WORK 105

5.1 CHF Prediction Model Development Using Force Balance 105

5.1.1 Katto CHF correlation (1984) for current experimental CHF result and comparison 111

5.1.3 Bowring CHF correlation (1972) for current experimental CHF result and comparison 114

5.2 Validation of Proposed Correlation with Other CHF Results from Open Literature 117

5.3 Enhancement of CHF under Flow Boiling Condition with Surface Modification by AP-Plasma 122

5.3.1 Observation on treated surface with SEM image and XPS 123

5.3.2 Surface features measurement (contact angle and coating layer thickness measurement) 126

5.3.3 Enhancement of CHF with AP-plasma treated surface under flow boiling condition 131

Nomenclature 137

References 139

6. CONCLUSIONS AND RECOMMENDATIONS 141

6.1 Conclusions 142

6.2 Recommendations for Future Work 144

APPENDIX A 149

A.1 Present CHF data (experimental Measurement, analytical prediction) 150

A.2 CHF data by Lee et al. (2008) 151

A.3 CHF data by Bang et al. (2002) 152

A.4 CHF data by Van der Mollen et al. (1978) 152

A.5 CHF data by Kim et al. (2009) 153

A.6 CHF data by Kim et al. (2010) 154

APPENDIX B 155

B.1 27% of CHF enhancement (80°→10 ° reduction of contact angle): 4bar, 124kg/m^2-s, 14.79 KJ/kg 155

B.2 22% of CHF enhancement (80 ° →10 ° reduction of contact angle): 4bar, 248kg/m^2-s, 9.42 KJ/kg 155

B.3 29% of CHF enhancement (80 ° →10 ° reduction of contact angle): 4bar, 0kg/m^2-s, 14.79 KJ/kg 156

B.4 4.8% of CHF enhancement (80 ° →10 ° reduction of contact angle): 4bar, 1000kg/m^2-s, 14.79 KJ/kg 156

B.5 Mass flux effect on CHF (0 kg/m^2-s → 350 kg/m^2-s): 4bar, 14.79 KJ/kg, 80 ° of contact angle 157

B.6 Sub-cooled enthalpy effect on CHF (0 KJ/Kg →70 KJ/kg): 4bar, 124 kg/m^2-s, 80 ° of contact angle 157

B.7 Pressure effect on CHF (200 kPa →1200 kPa): 124 kg/m^2-s, 14.79 KJ/kg , 80 ° of contact angle 158

APPENDIX C: CHF PREDICTION USING KATTO CORRELATION 159

APPENDIX D: EMPIRICAL CHF CORRELATION CALCULATION 160

List of figures

Figure 1.1 Boiling curve of a heat flux controlled surface in forced flow boiling water (Shim et al., 1997). 3

Figure 2.1 Heat transfer regions and CHF occurrence in a uniformly heated tube for conditions of low and high mass velocity flows (Issam Mudawar, 1998). 10

Figure 2.2 Flow boiling CHF mechanism according to (a) boundary layer separation model, (b) bubble crowding model (Issam Mudawar, 1998). 13

Figure 2.3 Dry spot developments on a burnout surface (Ha et al., 2008). 16

Figure 2.4 The dependence of critical heat flux on the contact angle (Liehard and Dhir, 1973). 19

Figure 2.5 The effect of contact angle on boiling curve (Kolev, et al., 2001). 19

Figure 2.6 The experimental results of measured CHF values for both flat plates and thin wires (Kim, H.D., 2011). 21

Figure 2.7 The CHF visualization in bubbly flow (Celata et al., 1998), Type 1. 23

Figure 2.8 The CHF visualization with near-wall vapor clots (Bang et al., 2004), Type 2 .. 23

Figure 2.9 The CHF visualization in slug/churn flow (Fiori and Bergles, 1970), Type 3 23

Figure 2.10 A part of 2006 CHF look-up table (Groeneveld, D.C., et al., 2006). 32

Figure 2.11 A comparison of the water equivalent CHF converted from Freon-12 data with the 1996 CHF look-up table (Cheng, X., 2003). 35

Figure 2.12 The experimental results of CHF values for both plates and thin wires (Kim H.D., 2011). 38

Figure 3.1 The schematic diagram of the R-134a forced convection boiling test loop. 48

Figure 3.2 An exploded view of the test section assembly. 52

Figure 3.3 The temperature profile on heating block walls at 100 seconds after critical heat flux occurring with power on (Zou, Ling, 2010). 53

Figure 3.4 Pictures of static contact angle of liquid drop test with/ without AP-plasma treatment on copper surface..... 55

Figure 3.5 The schematic diagram of the detail design information of the test section. 56

Figure 3.6 The schematic drawings of test sections and locations of thermocouples in side/ top view..... 57

Figure 3.7 A Camera and light arrangement for flow visualization tests (Top View). 60

Figure 3.8 The schematic diagram of atmospheric pressure plasma coating device..... 65

Figure 3.9 A picture of atmospheric pressure plasma coating device 67

Figure 3.10 A picture of AP-plasma coating on copper test section from side view. 67

Figure 3.11 A picture of Rame-Hart model 500, Advanced goniometer/ tensiometer 69

Figure 3.12 A picture of static contact angle measurement software. (www.psm.co.kr). 70

Figure 3.13 A picture of the model DEKTAK III- Stylus profilometer..... 71

Figure 4.1 The visualization of bubble behavior from isolate bubble regime (nuclear boiling) to coalesced bubble regime (near CHF). 76

Figure 4.2 A sudden temperature rise (a) and sudden heat flux drop (b) at the critical heat flux point. 77

Figure 4.3 A general boiling curve with highlighted single-phase region, two-phase region, CHF point under system pressure of 5 bar, inlet sub-cooled temperature of 4C$^{\circ}$, and mass flux of 186 kg/m2-s. 78

Figure 4.4 The linear relationships between CHF (q_c) and Δh_i for fixed mass flux, pressure (katto, Y., 1979). 79

Figure 4.5 Boiling curves with different sub-cooled inlet temperatures at P=500Kpa, G=186 kg/m^2-s..... 81

Figure 4.6 The effect of sub-cooling level on critical heat flux at fixed G=186 kg/m^2-s..... 81

Figure 4.7 CHF variation according to the mass flux; extracted from 1995 CHF look-up table (Kim et al., 2009). 82

Figure 4.8 Boiling curves with different mass fluxes at P=500Kpa, sub-cooled inlet temperature = 17C° 83

Figure 4.9 The effect of mass flux on critical heat flux with fixed pressure sub-cooling enthalpy. 84

Figure 4.10 The CHF variation according to system pressure; extracted from 2006 CHF look-up table. 85

Figure 4.11 Effect of system pressure on critical heat flux. 86

Figure 4.12 Comparison of predicted CHF values and measured CHF data points 91

Figure 4.13 Corresponding relationships between density ratios of R-134a and that of water along with pressure (Chen, et al., 2010). 96

Figure 4.14 A schematic diagram of equivalent water CHF converting process and comparison with CHF look-up table. 97

Figure 4.15 Ratios of the water-equivalent CHF data converted from the CHF data in R-134a to the CHF data from Look-up table with identical operating condition along with pressure 100

Figure 5.1 A force balance acting on a bubble parallel to the heating surface. 106

Figure 5.2 The comparison of CHF predicted from proposed model and experimental CHF data 111

Figure 5.3 The comparison of CHF predicted from Katto correlation and experimental CHF data 114

Figure 5.4 The comparison of the water-equivalent CHF data with the predicted CHF by Bowring correlation 116

Figure 5.5 The comparative study between proposed correlation prediction and Katto (1984) CHF prediction correlation 118

Figure 5.6 The comparison between CHF predictions by proposed correlation and 5 other researcher's CHF measurement (105 CHF data). 120

Figure 5.7 The comparative study between CHF prediction by the author's proposed correlation with contact angle and CHF prediction without contact angle. 121

Figure 5.8 Observation of copper surface with and without treatment (a) ×500 optical CCD image on untreated pure Cu surface, (b) SEM image for Cu surface before plasma treatment, (c) ×500 optical CCD image on plasma treated Cu surface, (b) SEM image for Cu surface. 124

Figure 5.9 The XPS spectra of untreated (a) and AP-plasma treated (b) copper surface... 125

Figure 5.10 The contact angle measurements along with AP-plasma treatment time (80~800Sec)..... 127

Figure 5.11 A series of picture of reduced contact angle along with increasing AP-plasma time. 128

Figure 5.12 A schematic diagram of static contact angle of liquid and calculated contact angle of water on copper surface by Yong's equation. 129

Figure 5.13 The oxidation layer thickness measurements along with AP-plasma treatment time (80~800Sec) 131

Figure 5.14 Comparison between CHF measurement with AP-plasma treatment and without treatment 133

Figure 5.15 Predicted CHF enhancements by proposed correlation along with decreasing contact angle. 134

Figure 5.16 The ratio of predicted CHF with different mass flux to CHF value at zero mass flux. 135

Figure 5.17 The ratio of predicted CHF with different sub-cooled level to CHF value at zero sub-cooled enthalpy. 135

Figure 5.18 The ratio of predicted CHF with different pressure to CHF value at 200kPa. 136

Figure 6.1 A conceptual diagram of surface wettability effect on CHF and CRUD induced wick boiling effect on CHF 145

Figure 6.2 (a) SEM image of nano-porous structure and fabrication process, (b) schematic of flow boiling test..... 146

Figure 6.3 The proposed future research pressure condition range (reduced pressure: 0.1 ~ 0.5). 147

List of tables

Table 2.1 The pool and flow boiling CHF enhancement studies with surface modifications. 37

Table 3.1 The physical and thermal properties of R134a at different pressures..... 50

Table 3.2 The lens Calibration and index ratio with respect to pixel. 60

Table 3.3 The summary of experimental opering conditions for CHF measurement test.... 61

Table 3.4 The operation condition of atmospheric pressure plasma coating..... 66

Table 4.1 The measured CHF data point in various experimental conditions..... 88

Table 4.2 The R-134a and water density ratios data along with pressure 96

Table 4.3 A selected conditions in R134a and the corresponding conditions in water..... 99

Table 4.4 A summary of R134a-water fluid-to-fluid modeling scaling factor..... 99

Table 4.5 Comparison between water-equivalent CHF value and 2006 CHF look-up table 100

Table 5.1 The summary of maximum deviation and MAD value for three CHF correlations. 116

1.Introduction

1.1 Background and Motivation

Sub-cooled nucleate boiling in forced convection and critical heat flux (CHF) have been drawing significant attention in many fields due to its good heat transfer efficiency and high heat removal capacity. Such advancement in sub-cooled nucleate boiling is the result of continuing efforts from both experimental and theoretical researchers, particularly focusing on CHF. A vapor film formed by excess bubble aggregation envelops on the heated surface, severely deteriorates heat transfer due to poor thermal conductivity of the vapor film, and eventually damaging the heating surface. Therefore, the designs of heat transfer systems that operate in the nucleate boiling regime are limited by CHF. In nuclear power plants, cladding material surrounds the radioactive nuclear fuel. It is crucial that nuclear reactors operate below CHF to prevent temperature excursions and subsequent failures of the heat transfer surfaces. Thus, increases in CHF provide a larger safety margin for the fuel and/or enable power uprates in commercial nuclear power plants. As a typical example, it has been demonstrated that a 32% increase in CHF would allow for 20% power density uprates in pressurized water reactors (PWR), thereby improving the economics of electricity generation (Jacopo *et al.*, 2008).

Boiling heat transfer is defined as a mode of heat transfer in which changes in phase occur in the liquid coolant. There are two basic types of boiling: pool boiling and flow boiling.

Pool boiling occurs on heating surfaces submerged in quiescent liquid, while flow boiling occurs on various geometries of heating surfaces in flowing channels. Both boiling conditions will incorporate phase change utilizing the enthalpy of evaporation (Tong et al., 1997). Researchers have investigated boiling heat transfer and two phase flow from different perspectives over several decades. The analysis of heat transfer in two-phase flow boiling conditions is quite complex because it involves fluid properties and flow characteristics of both liquid and vapor phases (McAdams et al., 1949; Bankoff et al., 1958; Chen et al., 1966; Collier et al., 1996). Therefore, most of the existing correlations of CHF are highly empirical and semi-analytical due to complexity of CHF mechanisms in both pool boiling and flow boiling conditions. In addition, in commercial thermal reactor industry applications and nuclear heat transfer systems utilize flow boiling heat transfer. It is worthwhile to investigate essential mechanisms of CHF, especially in flow boiling conditions. Thus, the aim of these experimental flow tests and analytical model developments in this present study were to establish better understanding of CHF, to advance CHF prediction model development and to enhance CHF with various operational conditions. This includes surface treatment using an atmospheric pressure plasma coating technique to modify boiling surfaces to increase their wettability (i.e. hydrophilic) in flow boiling conditions.

1.2 Critical heat flux (CHF) in Sub-cooled Flow Boiling

Critical Heat Flux (CHF), which is also known as burnout, dry-out, and boiling crisis which means departure from nucleate boiling (DNB). It represents a heat transfer phenomenon in

which there is a sudden decrease in the value of the heat transfer coefficient, and an abrupt increase in the surface temperature. CHF occurs when the heat flux of a heating surface increases or flow condition changes such that the generated vapor completely or partially blankets the heating surface, inhibiting good heat transfer. Thus, accurate prediction of (CHF) has been recognized to be a particularly important parameter in design and safety for heat exchanger equipment as well as in nuclear power plants.

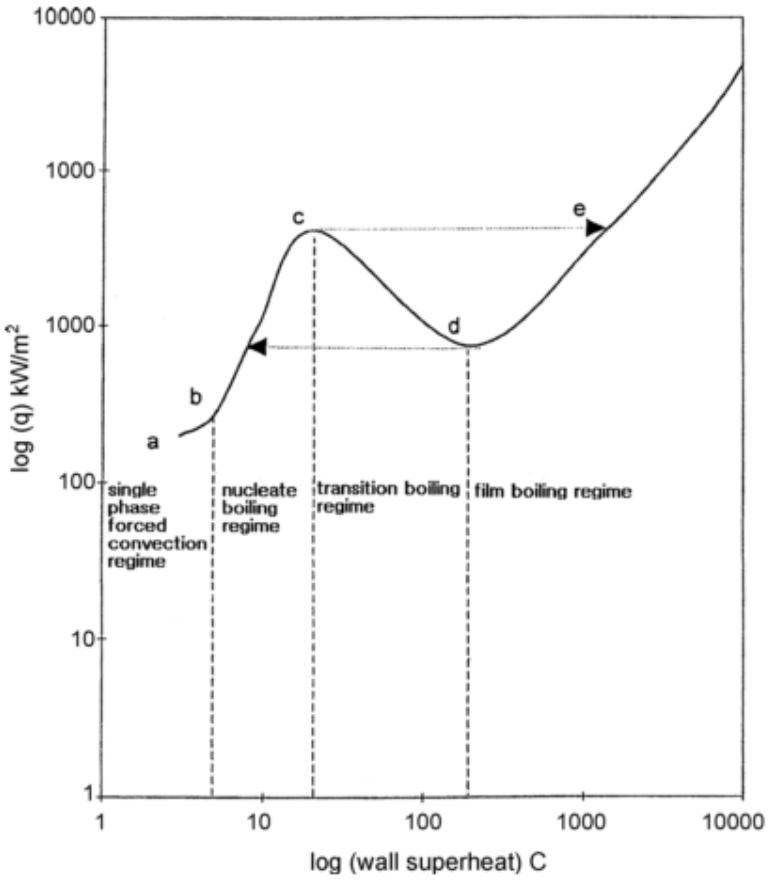


Figure 1.1 Boiling curve of a heat flux controlled surface in forced flow boiling water (Shim et

al., 1997).

A general boiling curve with uniform heat flux in flow boiling water conditions is shown in Fig. 1. The CHF is illustrated as the point “c,” which is the maximum value of heat flux on the plot of the heat flux versus the surface temperature. The maximum value is dependent on operating parameters such as system pressure, sub-cooled enthalpy, mass flux, and surface wetting condition. The regime, “a-b,” is the single phase sub-cooled forced convection regime, and “b-c” is the nucleation dominated boiling regime. The transition regime, “c-d,” is a normally unobservable regime, reached only by carefully controlling surface temperature. As the wall temperature is raised beyond the CHF point, unstable films of vapor form on the wall as well as large unstable bubbles. In “d” to “e” the regime is known as film boiling in which the surface temperature increases rapidly, whereas the heat flux increases insignificantly (see chapter 4). Therefore, when a stable vapor film is formed over the entire heating surface, it prevents significant heat transfer from the surface due to the poor conductivity of the vapor blanket covering the interface between liquid and solid, thus causing serious physical damage to the heating surface. It is also worthwhile to state that the nuclear power reactor is a heat flux controlled system rather than a surface temperature controlled system. In this resent study, all of CHF measurement or visualization experiments are conducted from the range of the nucleation dominated boiling regime to CHF point by gradual increments of heat flux.

Loss of coolant accidents (LOCA) in light water reactors, thermal safety performance analyses of nuclear power reactors, and safety evaluation of boilers are concerns of many researchers in recent years (Shim et al., 1997). As Mishima and Nishihara (1987) pointed out, the

prediction of CHF is complicated by the effect of buoyancy, flow instability, operating flow condition, and surface features. The flow becomes less stable due to the large specific volume of vapor at low pressure and the effect of buoyancy becomes significant at low flow conditions. Therefore, understanding for the CHF behavior in low pressure, low flow rate condition still needs further study.

In the literature, numerous studies on CHF with varying flow conditions, such as inlet sub-cooling level, pressure, and mass flux have been performed for flow boiling of water in round tube geometry. The studies have generated thousands of data sets, which led to numerous empirical correlations with limited success. These correlations used mainly system pressure, mass flux, inlet sub-cooling enthalpy (fixed inlet condition) or exit quality (fixed outlet condition) to predict the CHF over a wide range of operating conditions with various working fluids (e.g. water, R-12, R134a, and FC-72). However, despite these numerous efforts on understanding the CHF mechanism, a complete understanding of the nature of the CHF phenomenon has not been reached, and the surface effect on CHF in flow boiling conditions has not yet been attempted by the CHF technical community. This present study aimed to expand the understanding of CHF phenomenon with surface features as key variables of CHF prediction model development. The proposed model was validated through experimental CHF measurements with surface modification and various analytic approaches.

1.3 Objectives and Scope

The main objective of current research is to understand the sub-cooled flow boiling CHF characteristics under various operating conditions including mass flow rate, system pressure, inlet sub-cooled temperature, and surface wetting condition. The CHF data are obtained with various test conditions. A correlation, with taking in to account bubble force balance, is proposed for CHF prediction, and compared with current CHF experiment data and other CHF data from open literature for validation. In addition, the heating surface is modified by applying an atmospheric pressure (AP) plasma technique to increase wettability. The effect of surface wettability on CHF will be examined by both experimental data and author's proposed correlation.

Chapter 2 reports a literature review of characteristics of several existing CHF model in sub-cooled flow boiling. Analytical and empirical CHF prediction correlations in previous research are presented. It also includes the recent research activities of improved CHF with nano-fluid or the effect of surface treatment on CHF under the pool boiling condition.

Chapter 3 provides detailed information related to the experimental test facility with data acquisition system. In particular, this chapter deals with the sample preparation with atmospheric pressure plasma device. And the measurements of the static contact angle and oxidation layer thickness are explained.

Chapter 4 reports Boiling curves and CHF measurement that are generated with different

operating condition. The parametric trend (sub-cooled level, mass flux, and system pressure) study for CHF is presented. Fluid-to-fluid (R-134a to water) scaling model is utilized to compare the equivalent water CHF data with CHF look-up table under identical operational condition.

Chapter 5 proposes the analytical CHF prediction model using force balance with the consideration of surface characteristic. The current proposed model is benchmarked with other existing CHF correlation (Katto, Bowring), and validated with other open literature CHF data. Furthermore, In order to understand the effect of surface characteristic of heating plane on CHF, an atmospheric pressure plasma technic is utilized to generate oxidation films, which tender the surface to become more hydrophilic with reduced static contact angle compared to the reference surface (Non-AP-plasma treated surface).

The conclusions of the study are given in Chapter 6. The proposed analytical CHF predi ction model will be examined in extended operating conditions such as high pressure (more than 0.2 reduced pressure range) , high mass flux. In addition, thicker coating layer (50 micron~100 micron), which is identical to actual crud deposition, will be also examined to understand the wic k boiling effect on CHF in flow boiling condition.

References

Bankoff, S.G. 1958. “Entrapment of gas in the spreading of a liquid over a rough surface” AIChE.Journal 4:24-26

Chen, J.C. 1966. “Correlation for boiling heat transfer to saturated liquids in convective flow” Int. Eng. Chem. Process Design and Development 5:322-329

Collier, J.G. and Thome, J.R, 1996, “Convective boiling and condensation” 3rd edition, Oxford University Press

Jacopo, Buongiorno, Hu Lin-Wen, Seung-Joong Kim, Hannink Ryan, Truong Bao, Forrest Eric, 2008, “Nanofluids for enhanced economics and safety of nuclear reactors : an evaluation of the potential features, issues, and research gaps” Nuclear technology, vol. 162, pp. 80-91

McAdams, W.H., Minden, C.S., Carl, R., Picornell, D.M., and Dew, J.E. 1949. “Heat transfer at high rates to water with surface boiling” Ind. Eng. Chem. 41:1945-1953.

Mishima, K. and Nishihara, H., 1987, “Effect of Channel Geometry on Critical Heat Flux for Low Pressure Water,” Int. J. Heat Mass Transfer, 30(6), 1169

Shim, W. J., 1997, “On the Development of a Two-Phase Flow Meter for Vertical Upward Flow in Tubes,” Korean J. Chem. Eng., 14(6), 528

Tong L.S., Tang Y.S, 1997, “Boiling Heat Transfer and Two-Phase Flow (second ed.)”, Taylor and Francis, USA, pp. 391–398.

2.Literature Review

In this chapter, literature related to CHF will be reviewed. Theories related to sub-cooled flow boiling CHF will be discussed. Further, the prediction methods of CHF with analytical and empirical correlation (e.g. CHF look-up table) are discussed. Finally, the state-of-arts techniques, which leads to enhancement of CHF value either in pool boiling or flow boiling condition, are also presented.

2.1 Characteristics of Sub-cooled Flow Boiling CHF

The critical heat flux (CHF) condition is characterized by a sharp reduction of the local heat transfer coefficient that results from the replacement of liquid by vapor adjacent to the heat transfer surface (Collier and Thomes, 1996). A better understanding of CHF will form the basis for a reliable prediction model, and eventually, will provide insight into CHF enchantment strategies. It is usually understood that critical heat flux (CHF) represents the upper limit of boiling heat transfer performance and marks the termination of efficient heat transfer mechanism condition on the heated surface. Under different conditions of coolant mass flux, two types of CHF behavior in sub-cooled condition can be observed. One of them is *Dry-out (DO)*, which occurs in low mass velocities, low sub-cooling level or close to saturation temperature and large length-to-diameter ratio channels. It constitutes relatively small excursions in the wall temperature. *Departure from nucleate boiling* (DNB) is a more severe form of CHF because it precipitates abrupt rise in the heating surface temperature in the presence of abundant sub-cooled

bulk flow condition. Figure 2.1 shows the existence of two significant CHF behaviors.

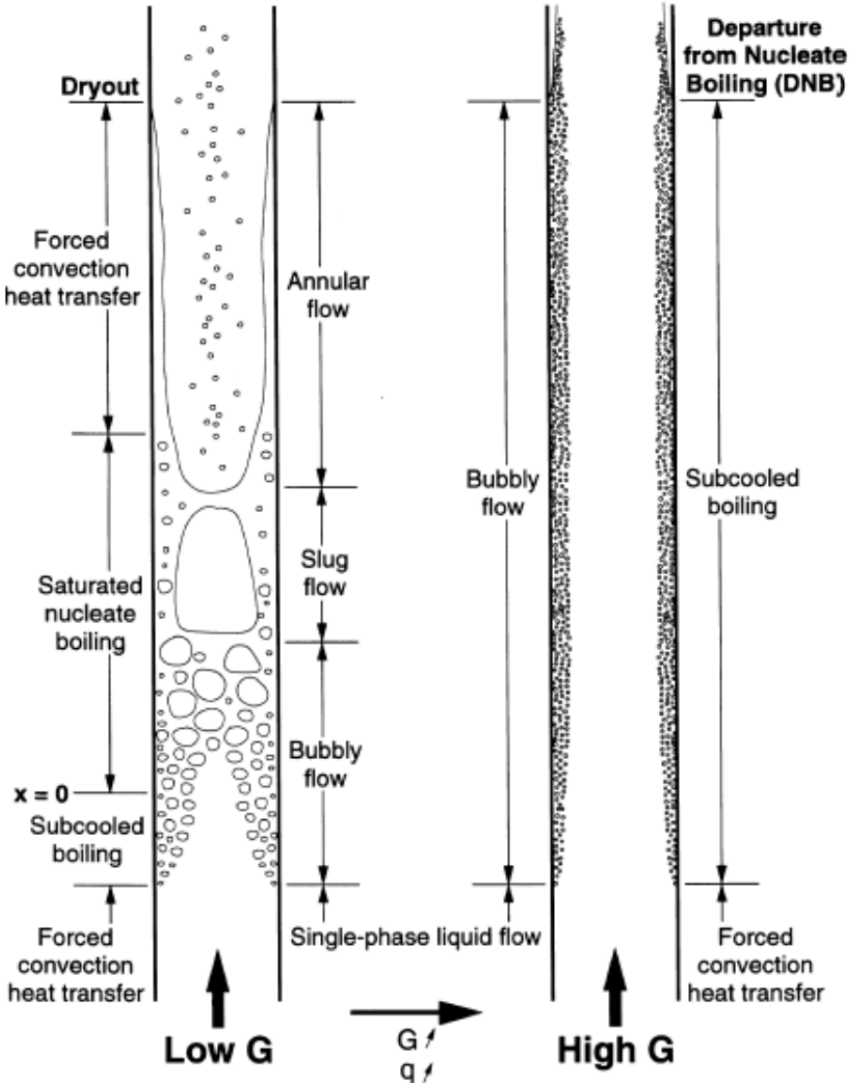


Figure 2.1 Heat transfer regions and CHF occurrence in a uniformly heated tube for conditions of low and high mass velocity flows (Issam Mudawar, 1998).

Researchers have investigated, both experimentally and theoretically, the basic physical mechanisms of CHF. Many studies have reported on the CHF mechanism and prediction model

for certain operating conditions with both pool and flow boiling heat transfer cases. However, no universal onset of the CHF mechanism or well-accepted CHF exists. In addition, due to the many variables of interest in the flow boiling case, the CHF prediction model for flow boiling is a significant challenge.

Up to now, four major physical mechanisms have been postulated as the trigger for CHF in sub-cooled flow boiling. All these models approach the problem by the restriction of bulk liquid flow from reaching the heating surface or fully developed vapor blanket over heating surface.

2.1.1 Boundary layer separation model (Hydrodynamic instability theory)

Zuber proposed the first model for the prediction of CHF on large horizontal surface in pool boiling condition (Zuber, 1959). This model is based on the hydrodynamics of vapor jet flow issuing from the infinite large heating surface. In this model Zuber believed that the CHF takes place when the velocity of the vapor jet flow reaches a critical velocity, which in turns initiates the Kelvin-Helmholtz instability. For inviscid fluids, Zuber obtained an expression for the CHF on an infinite flat plate in pool boiling as;

$$q_{CHF} = C\,\rho_v h_{fg} \sqrt[4]{\frac{\sigma g(\rho_l-\rho_v)}{{\rho_v}^2}} \left(\frac{\rho_l+\rho_v}{\rho_l}\right)^{1/2} \left[\frac{\rho_l(16-\pi)}{\rho_l(16-\pi)+\rho_v\pi}\right] \quad (2\text{-}1)$$

The value obtained from his experimental data for the constant C was $\pi/24$, other researcher (Kutateladze et al., 1964) also concluded that Zuber's correlation is valid and well represents CHF prediction model in low-pressure conditions, proposed the constant C as 0.168.

Later, Liehard and Dhir (1973) concluded the constant C value as 0.15 for various fluid cases with large horizontal plates. Kutateladze and Leont'ev (1964) also suggested that the flow boiling crisis can be analyzed using the concept of boundary layer separation induced by vapor injection. Their physical model led to the following equation;

$$q_{CHF} = \frac{C_1 h_{fg} \rho_l V_o}{Re^{0.6}} \tag{2-2}$$

where, $h_{fg}, \rho_l, V_o, and\ C_1$ are heat of vaporization, liquid density, free stream velocity, a function of equilibrium quality. An expression for C_1 was proposed by Tong (Tong, 1968) using existing flow boiling crisis data obtained in water at 6.9-13.8Mpa. However, none of model took surface wettability into consideration of CHF performance, and presumably assumed that the working fluid is well wetted on the heating surface (Zuber, 1959).

2.1.2 Bubble crowding model

This mechanism is governed by turbulent fluctuation in the liquid flow at the out edge of the near-wall bubbly layer. As shown in Figure 2.2, these turbulent fluctuations become too weak at high heat fluxes to transport bulk liquid through the dense bubbly layer in order to sustain enough heat transfer. Weisman and Pei (1983) first consider the existence of a bubbly layer adjacent to the wall at sub-cooled or low quality conditions. Although their model assumes the existence of a bubbly layer, the enthalpy transport from this bubbly layer to the bulk flow is considered as the limiting factor leading to the CHF condition. They consider the CHF to be a local phenomenon. The liquid region in the immediate vicinity of the heater fills with bubbles

building a bubbly layer. In this region, the turbulent eddy size is insufficient to transport the bubbles away from the heater surface. At the CHF location, this layer is assumed to be at its maximum thickness.

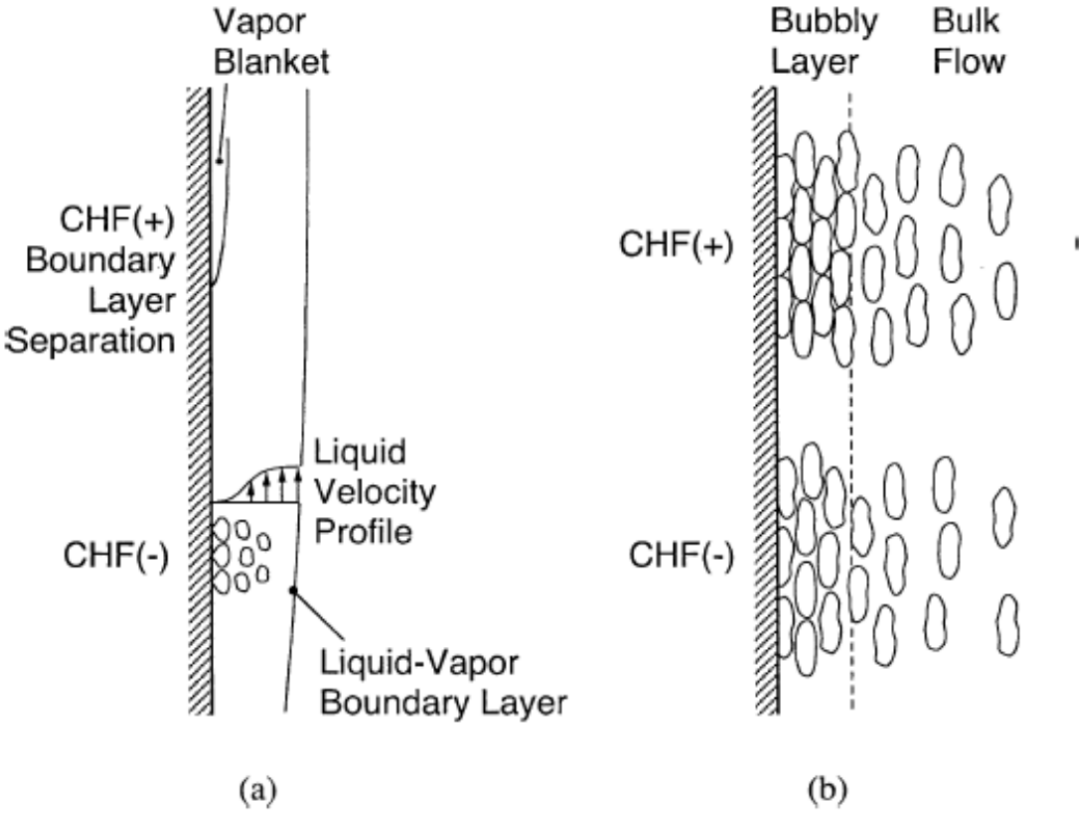


Figure 2.2 Flow boiling CHF mechanism according to (a) boundary layer separation model, (b) bubble crowding model (Issam Mudawar, 1998).

It is postulated that the CHF condition occurs when the void fraction of vapor in the bubbly layer just exceeds the critical value at which an array of ellipsoidal bubbles can be

maintained without significant contact between the bubbles. Weisman and Pei used the homogeneous flow model in the bubbly layer. The resulting model has three adjustable empirical constants that are evaluated from the experimental data. However, the use of this critical void fraction assumption raises serious questions about the validity of this model, since local void fraction is very hard to measure and has limited utilization in practical application.

2.1.3 Sub-layer (Macro layer) dryout model

Katto has questioned the validity of the assumption of the instability of large vapor jets used in the hydrodynamic theory as originally proposed in Zuber's model. He visualized the pool boiling phenomena with the help of high-speed cameras and found that the presence of large vapor mushroom type bubbles on the heater surface rather than tall vapor jet shapes. (Katto et al., 1984) In Katto's model, a macro layer dry-out model, the CHF occurs when the liquid film is trapped between the base of the mushroom bubble and the wall. However, this model was also not associated with the effect of surface wetting feature on CHF as well. His semi-empirical model was limited in pool boiling condition. Several investigators have extended the Katto model to flow boiling heat transfer and to the jet impingement cooling. (Celata et al., 1994a) Later, Celata developed this model by using different methods to calculate vapor departure diameter and liquid sub-layer thickness.

$$q_{CHF} = \frac{\rho_l \delta h_{fg}}{L_B} U_B \tag{2-3}$$

$$\delta = y^* - U_B \tag{2-4}$$

$$D_B = \frac{32}{f}\frac{\sigma g(\beta)\rho_l}{G^2} \tag{2-5}$$

$$\frac{1}{\sqrt{f}} = 114 - 2.0\log\left(\frac{\varepsilon}{D_e} + \frac{9.35}{Re\sqrt{f}}\right) \tag{2-6}$$

The prediction accuracy of sub-layer dry-out model may be improved by applying new empirical correlation for life-off vapor diameter based on more precise observation, however, the difficulty of obtaining good prediction of temperature profile in two phase flow highly limits the application of this model.

2.1.4 Dry-spot model (Wall overheat theory)

Ha and No (1998) first proposed dry-spot model for predicting critical heat flux in pool and forced convection boiling based on early studies on boiling heat transfer mechanics, nucleation site density distribution and its relation with heat flux. The Dry-spot hypothesis was later on confirmed by Theofanous (2002a) in X-ray radiographic visualization experiments. It was observed that dry spot is constrained and guided by neighboring active nucleation sites. Repeated observation showed that the initiation of dry spot is random, and some of dry spots might happen under moderate heat flux levels, but they were not sustainable and disappeared rapidly. Figure 2.3 demonstrated sequential dry spot development images on a burnout surface. In addition, the Ha and No believed that the boiling heat transfer has weak dependence on the two-phase flow hydrodynamics above the bubble layer when it approaches critical heat flux.

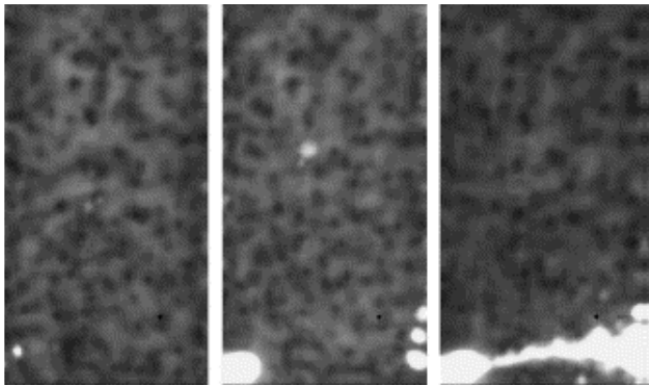


Figure 2.3 Dry spot developments on a burnout surface (Ha et al., 2008).

As discussed before, according to Mikic's model, boiling heat transfer can be discretized in to individual nucleation site, and each such site contributes amount of heat transfer (single phase natural circulation or convection counted for non-boiling area, but it is not important when boiling is fully developed). When heat flux is elevated, the extra amount of heat flux will be removed by the increased nucleation sites and higher bubble departure frequency, which in turn will increase the heat transfer from individual site. However, the total amount heat flux can still be counted as summation of heat flux contributed by single nucleation site.

The dry-spot behavior can be modified by the presence of the nanoparticles on the surface, which was recently found to be the direct consequence of the nanofluids boiling (kim et al., 2006, Bang et al., 2005). It was also confirmed that the presence of the nanoparticle layer increased the surface wettability significantly. Plausibly the improved wettability can help delay the CHF by promoting the rewetting of hot/dry spots upon bubble departure. In the literature, however, no relevant study about the wettability on subcooled flow boiling CHF is found.

Therefore, as an alternative, a pool boiling CHF model that accounts for the wettability effect are introduced (Kandlikar, 2001). Kandlikar observed significant effect of contact angle on the CHF and modeled its contribution by considering the forces exerted on the bubble due to momentum change from evaporation, surface tension acting on base and top of the bubble, and pressure gradient due to buoyancy. The final form of the model/correlation is expressed as:

$$q_{CHF,sat} = h_{fg}\rho_g^{0.5}\left(\frac{1+cos\theta}{16}\right)\left[\frac{2}{\pi}+\frac{\pi}{4}(1+\cos\theta)cos\varphi\right]^{0.5}\left[\sigma g(\rho_f-\rho_g)\right]^{1/4} \qquad (2\text{-}7)$$

where, $\theta, \varphi,$ and σ are static contact angle of liquid, orientation of heater surface (horizontal up-facing: $\varphi = 0°$), and surface tension, respectively. This model provides a basis for the physical consideration of the contact angle, θ Kandlikar points out that use of the dynamic contact angle would be the best choice for the model. However, he also recommends use of static contact angle as an alternative if receding contact angle data are unavailable. Since static contact angle is directly measured in this study, the model will be used in our analysis.

2.2 Parametric Effects on CHF in Sub-cooled Flow Boiling

Several system variables affect the critical heat flux: heater geometry, liquid sub-cooling, flow velocity, system pressure, and surface wettability (Bergles et al., 1963). Generally CHF increases as sub-cooling level (enthalpy) increases. At low sub-cooling levels, particularly, CHF increases linearly when the sub-cooling level increases; this is identical with Zuber hydrodynamic model. However, at medium and high sub-cooling levels, the CHF become nonlinear and independent of sub-cooling level. The flow velocity delays the onset of CHF

occurrence because of the more effective coolant flow onto the heating surface, which leads to increased boiling heat transfer capabilities. For the system pressure effect, the CHF is increased as the pressure is increased in low-pressure condition(less than 0.2 reduced pressures, which in turn 8 bar for R-134a and 45 bar for water). The suppressed system pressure hinders nucleate bubble boiling leading to the film boiling stage and leads to a slightly higher upper limit of CHF (Theofanous et al., 2002b). However, it is noted that more research is necessary to establish the quantitative correlation of CHF prediction with several system parameters including surface characteristics.

Recently researchers have documented the effect of the surface wetting characteristics on CHF performance (Liaw et al., 1988, Kandlikar et al., 2001, Kim et al., 2007). Liaw and Dhir studied pool boiling of saturated water at atmospheric pressure (1 bar) on a vertical surface. They applied a surface treatment to the heating surface using oxidation, and the static contact angle was measured indicating the degree of wettability. Their findings indicated that the CHF increases with decreasing static contact angle.

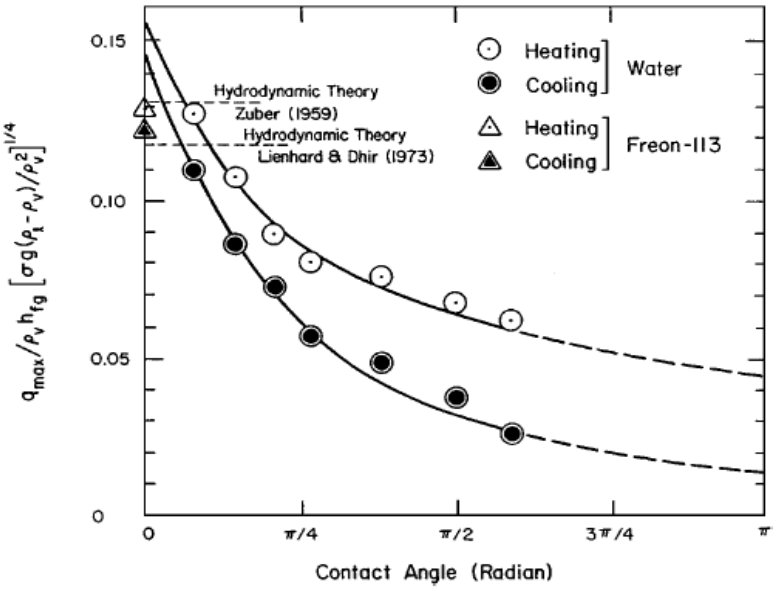


Figure 2.4 The dependence of critical heat flux on the contact angle (Liehard and Dhir, 1973).

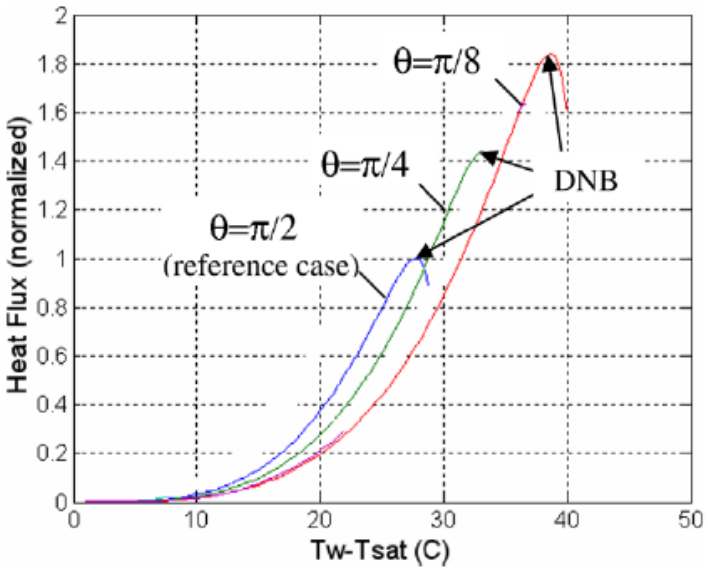


Figure 2.5 The effect of contact angle on boiling curve (Kolev, et al., 2001).

Figure 2.4 shows the normalized critical heat flux as a function of static contact angle with water and R-113 as working fluids for pool boiling condition. As it is seen in figure 2.4, the data obtained with water and with R-113 at a low static contact angle (~18°) indicate good agreement with Zuber's hydrodynamic theory. However when the contact angles range from 27° to 107°, the deviation error for the critical heat flux prediction by Zuber's model becomes large and unpredictable. Therefore, the surface wettability, i.e. static contact angle, becomes an important parameter for CHF prediction even though it is not easily implemented into existing classical models in figure 2.5 (Kolev, et al., 2001).

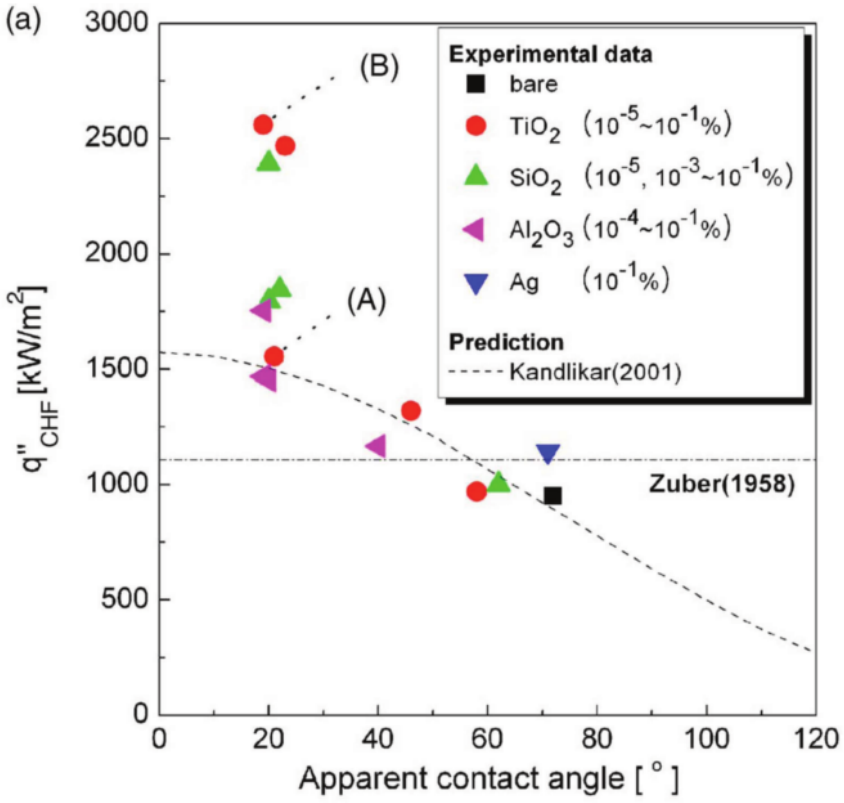


Figure 2.6 The experimental results of measured CHF values for both flat plates and thin wires (Kim, H.D., 2011).

Recently, Kim H.D. (2011) showed that the estimated heat-flux gain due to capillary liquid supply along the porous layer was of the same order of magnitude as that due to wettability enhancement (see fig. 2.5). Kim concluded that significant CHF enhancement of nano-fluid during pool boiling is a consequence of not only increased surface wettability, but also improved capillary resulting from the surface deposition of nanoparticles. A consensus explanation of the cause of CHF enhancement in nano-fluids seems to be obtainable via an intense study focused on the effect of the nanoparticle deposition layer. In order words, the CHF

of a nano-fluid is enhanced by its improved ability to actively wet the heating surface, thanks to the porous structure of the thin nanoparticle sorption layers.

2.3 CHF Visualization Experiments and CHF Flow Regime Map

A review of available two-phase flow visualizations and measurement near CHF under sub-cooled flow boiling conditions was performed as a contribution to a better understanding of the phenomena. The observed two-phase flow regimes were classified into three distinct types and related to relevant parameters (based on a dimensional analysis) in an attempt to develop a tool, which can be used to generally predict the two-phase flow regimes at CHF (Corre J., 2007).

Experimental programs of CHF visualization have been conducted in the past by different investigators in order to understand the physical mechanisms leading to the CHF in sub-cooled flow boiling conditions. However, experimental difficulties such as requirement for very high heat fluxes, large temperature gradients near wall surfaces are often encountered. The boiling wall may be hidden by bubbles in the bulk flow. As an example of the different CHF flow regimes that have been observed we can note the work by Celata et al. (1998) where CHF was observed in bubbly flow with wall-rooted nucleating bubbles (see Fig. 2.6), the work by Bang et al. (2004) where CHF occurred while near-wall vapor clots were observed to slide along the heated wall (see Fig. 2.7) and the work by Fiori and Bergles (1970) where CHF was observed in slug and churn flow regime (see Fig. 2.8). These three flow regimes are representative of the three general types of CHF flow regimes that were observed among most experimental investigations (under sub-cooled flow boiling conditions) found in the literature. The main

characteristics of these flow regimes are listed below:

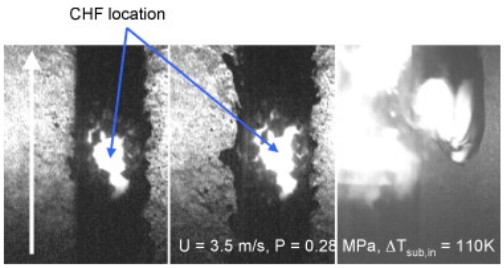


Figure 2.7 The CHF visualization in bubbly flow (Celata et al., 1998), Type 1.

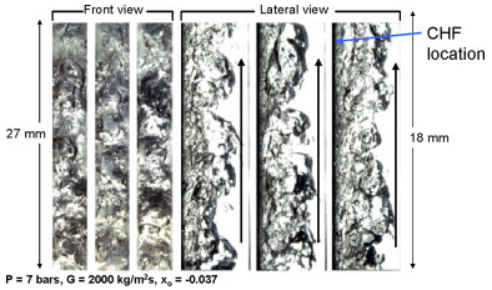


Figure 2.8 The CHF visualization with near-wall vapor clots (Bang et al., 2004), Type 2

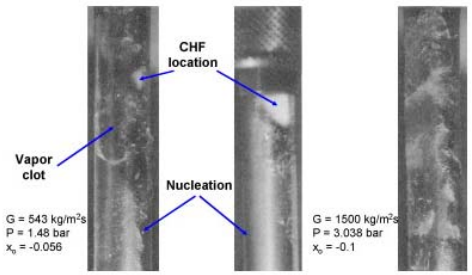


Figure 2.9 The CHF visualization in slug/churn flow (Fiori and Bergles, 1970), Type 3

Type 1: Bubbly flow

Usually it is observed under high mass flux and high sub-cooling. Isolated bubbles nucleate, may slide and detach but do not coalesce. Wall-rooted bubbles are observed to coalesce with neighboring bubbles along the flow stream in some cases (Celata et al., 1998). A reduced boiling activity is often observed at CHF. In general, bubbles size increases with decreased sub-cooling and lower pressure.

Type 2: Vapor clots

Usually vapor clots are observed under moderate sub-cooling condition. Bubbles nucleate and detach from nucleation sites. Near CHF, most bubbles remain within the bubbly layer and coalesce to form periodic vapor clots. Vapor clot lengths are governed by Kelvin–Helmholtz instability while wetting fronts between vapor clots are observed to undergo intense boiling. In general, overall bubbly layer thickness and bubble size decreases with increased sub-cooling and mass flux.

Type 3: Slug flow

Usually slug flow is observed under low mass flux and near saturation. Vapor slugs are observed with thin liquid film along the wall. Fluctuating wall temperatures can be measured with high temperatures corresponding to vapor slugs. In many cases the liquid film is not observed at CHF (Fiori and Bergles, 1970).

2.4 Prediction of CHF

This section summarized previous investigations on general CHF prediction models. Critical heat flux prediction methodology can be categorized as analytical mechanistic models or empirical correlations. Analytical mechanistic models are developed from the consideration of physical mechanisms of force balance: bubble evaporation, inertial, gravity, and shear. This leads to onset of critical heat as discussed in the previous section. Since there remains a lacks of understanding on CHF mechanisms, a continuing effort on the development of analytical mechanism model for CHF is required.

Empirical correlations are mainly generated from regression curve fitting with various experimental databases. From existing empirical correlations, CHF trends with system parameters such as pressure, mass flux, and sub-cooled inlet temperature have been performed and reported by previous researcher. In addition one of empirical methods to predict the CHF with high accuracy is using look-up tables. This allows CHF prediction with various operational conditions from tabulated databases provided by many of research group from world-wide collaboration.

2.4.1 Analytical prediction models

There are no universal governing CHF models for pool and flow boiling conditions, and several analytical models have developed for the same experimental conditions (system pressure, mass flux, inlet sub-cooled enthalpy, etc.). Up to 1970s, Zuber's hydrodynamic instability model

had been widely accepted and extended by other researchers. Lack of visual evidence and poor prediction for low surface wettability cases provided a need to develop advanced models. A liquid macro layer dry-out model introduced by Katto (1983) became an accepted model for flow boiling conditions. Many researchers (Ha and No, 1998; Kolev, 2001; Kandlikar et al., 2001; Theofanous, 2002b) have subsequently proposed new phenomenological models. Models proposed for pool boiling CHF predictions, however, need further improvement in parallel with more experimental validation work.

Analytical modeling for the flow boiling case has also been investigated by several researchers. CHF prediction model in flow boiling have developed relatively slowly compared to pool boiling study due to more complex physical phenomena and flowing fluid effects on the boiling process. Among several CHF prediction correlations, which have been proposed, the bubble coalescence model (Weisman and Pei, 1983) and the liquid sub-layer dry-out model (Katto et al., 1990) have resulted in reasonable predictions compared with flow boiling experimental conditions. In general, the Weiman and Pei's bubble coalescence model is applicable for the high pressure operating conditions, which are practical range for commercial PWRs. The liquid sub-layer model proposed by Katto predicts well in the low pressure with high speed flow conditions that are related to the fusion applications.

The correlations included here are either the most widely used or on the basis of their possible extrapolation to conditions different from the originating experimental condition, though this must be done with great care.

Gunther (1951)

$$q_{CHF} = 7198v^{0.5}\Delta T_{sub} \tag{2-8}$$

recommended ranges; P=0.1–1.1MPa, v=1.5–12.1m/s, CHF=0.4–11.4MW/m^2, ΔTsub=11-39K.

Tong et al., (1968)

$$q_{CHF} = (0.23 \times 10^6 + 0.094\dot{m}) \times (3 + 0.018\Delta T_{sub}) \times$$

$$\left[0.435 + 1.23e^{-0.0093\frac{L}{D}}\right] \times \left\{1.7 - 1.4e^{-0.532\left(\frac{h_f - h_{in}}{h_{fg}}\right)^{\frac{3}{4}}\left(\frac{\rho_g}{\rho_f}\right)^{\frac{1}{3}}}\right\} \tag{2-9}$$

recommended ranges; P=5.5-19.0MPa, v=.3-12.1m/s, CHF=0.4–4MW/m^2, L/D=21-365, ΔTsub=0-126.7K.

Tong (1968, known as Tong-68 correlation)

$$\frac{q_{CHF}}{h_{fg}} = C\frac{G^{0.4}\mu^{0.6}}{D^{0.6}} \tag{2-10}$$

$C=1.765-7.433x_{out}+12.222(x_{out})^2$

The Tong-68 correlation can also be written as:

$$Bo = \frac{C}{Re^{0.6}} \tag{2-11}$$

recommended ranges: P > 7.0MPa.

Tong (1975)

$$q_{CHF} = 0.023 f G h_{fg} \left[1 + 0.0216 \left(\frac{P_{out}}{Pcrit}\right)^{1.8} Re^{0.5} Ja\right] \quad (2\text{-}12)$$

Where;

$$f = 8 \left(\frac{D}{D_o}\right)^{0.32} Re^{-0.6}, with\ D_o = 1.27 \times 10^{-2} m, \quad (2\text{-}13)$$

$$Ja = \frac{C_p (T_w - T_{in})}{h_{fg}} \frac{\rho_l}{\rho_g} \quad (2\text{-}14)$$

$$Re = \frac{GD}{\mu(1-x)}, \text{ with x evaluated by equivalent heat balance,} \quad (2\text{-}15)$$

recommended ranges of P=6.8-13.6Mpa, v = 0.68-5.9m/s, d=3-10mm, l/d=5-100.

Modified Tong-68 (Celata, 1994b)

A modification of the Tong-68 correlations, for pressures lower than 7.0Mpa, has been proposed by Celata et al., (1994b).

$$Bo = \frac{C}{Re^{0.5}} \ , C = (0.216 + 4.74 \times 10^{-2} P)\varphi \ \ (P\ in\ \ Mpa), \quad (2\text{-}16)$$

$$\varphi = \begin{cases} 1 & x_{out} < -0.1 \\ 0.825 + 0.986 x_{out} & 0 > x_{out} \geq -0.1 \\ \frac{1}{2+30 x_{out}} & x_{out} \geq 0 \end{cases}$$

recommended ranges of P=5.5Mpa, v = 2.2-40m/s, ΔTsub = 15-190K, D=0.3-15mm.

Katto's CHF model (1984)

$$q_c = q_{co}\left(1 + \frac{\Delta h_i}{h_{fg}}\right) \tag{2-17}$$

where,

$$\frac{q_{co}}{Gh_{fg}} = \min\left(\frac{CW^{0.043}}{L/D}, \frac{0.1(\rho_g/\rho_f)^{0.133}W^{0.333}}{1+0.0031(L/D)}, \frac{0.098\left(\frac{\rho_g}{\rho_f}\right)^{0.133}W^{0433}(L/D)}{1+0.0031(\frac{L}{D})}\right)$$

$$K = \max\left(\frac{1.043}{4CW^{0.043}}, \frac{\left(\frac{5}{6}\right)(0.0124 + \frac{D}{L})}{(\rho_g/\rho_f)^{0.133}W^{0.333}}\right)$$

$$W = \frac{\sigma\rho_f}{G^2L}\ , \qquad C = 0.25, \qquad q_{co} : \textit{CHF value at saturation flow condition.}$$

It can be seen that there have been numerous explanations, analytic prediction correlations, and empirical correlations of CHF. Among them, none has achieved prevailing success. There has always been controversy on the pros and cons of the basis among different models and prediction correlation in certain application range. In other words, although critical heat flux can be physically interpreted as the limit of heat flux with the increase of wall superheat, there is no such a model that successfully interprets the relationship between surface feature and CHF. It is evident that a model that can provide combined prediction of boiling and CHF is yet to be developed in which each and every component of the wall heat flux is identified and correctly and independently computed. The modeling should be such that the correct and

complete modeling that captures the basic form of sub-cooled flow boiling phenomena with macroscopic parameter (operating condition) and microscopic parameter (surface wettability, contact angle). A proposed CHF flow boiling prediction correlation using bubble force balance with surface wettability concept will be demonstrated in chapter 4.

2.4.2 Empirical prediction models

Empirical prediction models have been proposed from extensive CHF experiment data. Empirical prediction methods can be identified as (1) empirical CHF prediction correlations, and (2) CHF Look-up tables.

The CHF measurements in uniformly heated round tube tests have been intensively investigated worldwide and have resulted in more than a 30,000 database for experimental CHF under a variety of experimental condition. A reliable empirical prediction model for CHF in tube channels is important because such results will provide insight into the basic parametric trends for CHF prediction in many thermal application fields including the nuclear industry. Generally an empirical correlation is investigated using the regression process with a help of CHF test result and a proper set of key variables for a prediction correlation. Due to the limited reliable CHF databases, its prediction accuracy becomes poor when an empirical correlation is applied to a wide range of operating conditions. Therefore, most of empirical correlations should provide an applicable operating parameter range to achieve best accuracy for CHF prediction.

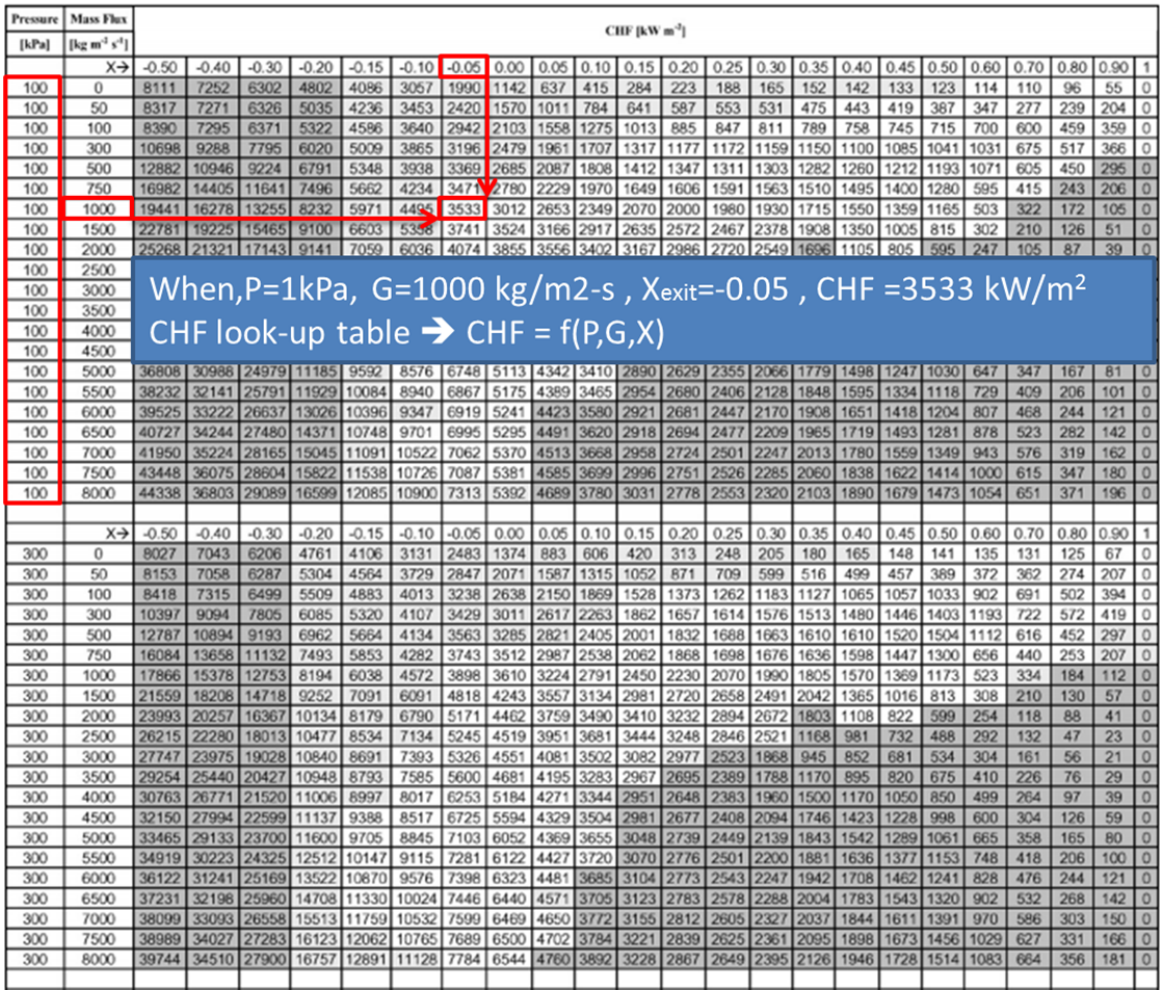
The look-up table method was first developed by Russian investigator, (Doroschchuk et al., 1975] and extended the look-up table method for critical heat flux prediction (Groeneveld et

al., 1996, Groeneveld et al., 2006) This method became intensively utilized in many thermal hydraulic codes for safety analysis of nuclear reactors such as, REALP5/MOD3, CATHARE, CATHENA, etc., (Tong et al., 1988). This look-up table provides a high fidelity of CHF prediction, and simplicity in implementation over a wide range of applicability for the operating condition in nuclear power plants. The look-up table introduced by Groeneveld (1996, 2006) provides predicted CHF values for an 8 mm tube at discrete values of pressure, mass flow rate, and quality, providing a simple relationship for the diameter effect on CHF (see fig. 2.9). Then, the loop-up table can be utilized to predict the CHF point for various geometry conditions by applying a correlation (eq. 2-7), which is coupled with diameter effect, i.e.

$$\frac{CHF_D}{CHF_{D=8mm}} = \left(\frac{D}{8}\right)^n \tag{2-18}$$

n = -0.5, Diameter: 4mm ~16mm (Doroshchuk, 1975)

n= -0.333, Diameter: 4mm ~ 32mm (Groeneveld et al., 1996, 2006)



Pressure [kPa]	Mass Flux [kg m^{-2} s^{-1}]	CHF [kW m^{-2}]																					
	X→	-0.50	-0.40	-0.30	-0.20	-0.15	-0.10	-0.05	0.00	0.05	0.10	0.15	0.20	0.25	0.30	0.35	0.40	0.45	0.50	0.60	0.70	0.80	0.90	1
100	0	8111	7252	6302	4802	4086	3057	1990	1142	637	415	284	223	188	165	152	142	133	123	114	110	96	55	0
100	50	8317	7271	6326	5035	4236	3453	2420	1570	1011	784	641	587	553	531	475	443	419	387	347	277	239	204	0
100	100	8390	7295	6371	5322	4586	3640	2942	2103	1558	1275	1013	885	847	811	789	758	745	715	700	600	459	359	0
100	300	10698	9288	7795	6020	5009	3865	3196	2479	1961	1707	1317	1177	1172	1159	1150	1100	1085	1041	1031	675	517	366	0
100	500	12882	10946	9224	6791	5348	3938	3369	2685	2087	1808	1412	1347	1311	1303	1282	1260	1212	1193	1071	605	450	295	0
100	750	16982	14405	11641	7496	5662	4234	3471	2780	2229	1970	1649	1606	1591	1563	1510	1495	1400	1280	595	415	243	206	0
100	1000	19441	16278	13255	8232	5971	4495	3533	3012	2653	2349	2070	2000	1980	1930	1715	1550	1359	1165	503	322	172	105	0
100	1500	22781	19225	15465	9100	6603	5358	3741	3524	3166	2917	2635	2572	2467	2378	1908	1350	1005	815	302	210	126	51	0
100	2000	25268	21321	17143	9141	7059	6036	4074	3855	3556	3402	3167	2986	2720	2549	1696	1105	805	595	247	105	87	39	0
100	2500																							
100	3000																							
100	3500																							
100	4000																							
100	4500																							
100	5000	36808	30988	24979	11185	9592	8576	6748	5113	4342	3410	2890	2629	2355	2066	1779	1498	1247	1030	647	347	167	81	0
100	5500	38232	32141	25791	11929	10084	8940	6867	5175	4389	3465	2954	2680	2406	2128	1848	1595	1334	1118	729	409	206	101	0
100	6000	39525	33222	26637	13026	10396	9347	6919	5241	4423	3580	2921	2681	2447	2170	1908	1651	1418	1204	807	468	244	121	0
100	6500	40727	34244	27480	14371	10748	9701	6995	5295	4491	3620	2918	2694	2477	2209	1965	1719	1493	1281	878	523	282	142	0
100	7000	41950	35224	28165	15045	11091	10522	7062	5370	4513	3668	2958	2724	2501	2247	2013	1780	1559	1349	943	576	319	162	0
100	7500	43448	36075	28604	15822	11538	10726	7087	5381	4585	3699	2996	2751	2526	2285	2060	1838	1622	1414	1000	615	347	180	0
100	8000	44338	36803	29089	16599	12085	10900	7313	5392	4689	3780	3031	2778	2553	2320	2103	1890	1679	1473	1054	651	371	196	0
	X→	-0.50	-0.40	-0.30	-0.20	-0.15	-0.10	-0.05	0.00	0.05	0.10	0.15	0.20	0.25	0.30	0.35	0.40	0.45	0.50	0.60	0.70	0.80	0.90	1
300	0	8027	7043	6206	4761	4106	3131	2483	1374	883	606	420	313	248	205	180	165	148	141	135	131	125	67	0
300	50	8153	7058	6287	5304	4564	3729	2847	2071	1587	1315	1052	871	709	599	516	499	457	389	372	362	274	207	0
300	100	8418	7315	6499	5509	4883	4013	3238	2638	2150	1869	1528	1373	1262	1183	1127	1065	1057	1033	902	691	502	394	0
300	300	10397	9094	7805	6085	5320	4107	3429	3011	2617	2263	1862	1657	1614	1576	1513	1480	1446	1403	1193	722	572	419	0
300	500	12787	10894	9193	6962	5664	4134	3563	3285	2821	2405	2001	1832	1688	1663	1610	1610	1520	1504	1112	616	452	297	0
300	750	16084	13658	11132	7493	5853	4282	3743	3512	2987	2538	2062	1868	1698	1676	1636	1598	1447	1300	656	440	253	207	0
300	1000	17866	15378	12753	8194	6038	4572	3898	3610	3224	2791	2450	2230	2070	1990	1805	1570	1369	1173	523	334	184	112	0
300	1500	21559	18208	14718	9252	7091	6091	4818	4243	3557	3134	2981	2720	2658	2491	2042	1365	1016	813	308	210	130	57	0
300	2000	23993	20257	16367	10134	8179	6790	5171	4462	3759	3490	3410	3232	2894	2672	1803	1108	822	599	254	118	88	41	0
300	2500	26215	22280	18013	10477	8534	7134	5245	4519	3951	3681	3444	3248	2846	2521	1168	981	732	488	292	132	47	23	0
300	3000	27747	23975	19028	10840	8691	7393	5326	4551	4081	3502	3082	2977	2523	1868	945	852	681	534	304	161	56	21	0
300	3500	29254	25440	20427	10948	8793	7585	5600	4681	4195	3283	2967	2695	2389	1788	1170	895	820	675	410	226	76	29	0
300	4000	30763	26771	21520	11006	8997	8017	6253	5184	4271	3344	2951	2648	2383	1960	1500	1170	1050	850	499	264	97	39	0
300	4500	32150	27994	22599	11137	9388	8517	6725	5594	4329	3504	2981	2677	2408	2094	1746	1423	1228	998	600	304	126	59	0
300	5000	33465	29133	23700	11600	9705	8845	7103	6052	4369	3655	3048	2739	2449	2139	1843	1542	1289	1061	665	358	165	80	0
300	5500	34919	30223	24325	12512	10147	9115	7281	6122	4427	3720	3070	2776	2501	2200	1881	1636	1377	1153	748	418	206	100	0
300	6000	36122	31241	25169	13522	10870	9576	7398	6323	4481	3685	3104	2773	2543	2247	1942	1708	1462	1241	828	476	244	121	0
300	6500	37231	32198	25960	14708	11330	10024	7446	6440	4571	3705	3123	2783	2578	2288	2004	1783	1543	1320	902	532	268	142	0
300	7000	38099	33093	26558	15513	11759	10532	7599	6469	4650	3772	3155	2812	2605	2327	2037	1844	1611	1391	970	586	303	150	0
300	7500	38989	34027	27283	16123	12062	10765	7689	6500	4702	3784	3221	2839	2625	2361	2095	1898	1673	1456	1029	627	331	166	0
300	8000	39744	34510	27900	16757	12891	11128	7784	6544	4760	3892	3228	2867	2649	2395	2126	1946	1728	1514	1083	664	356	181	0

Figure 2.10 A part of 2006 CHF look-up table (Groeneveld, D.C., et al., 2006).

2.4.3 Fluid-to-fluid scaling CHF prediction method

Fluid modeling is widely used in thermal-hydraulic design of nuclear reactors (Ahmad et al., 1973, Katto 1978). One of the main tasks concerning the fluid modeling is the transfer of the test data obtained in the model fluid to the prototypical fluid (water). An analysis shows that by neglecting geometric scaling and the effect of heat transfer surface properties on CHF. There

exist more than 10 independent dimensionless numbers that describe the CHF under forced flow condition (Cheng X., 2003). It is obviously impossible to achieve a complete similarity using different fluids, because of the limiting degree of freedom available for experimentation. During the CHF experiments four thermal-hydraulic parameters can normally be adjusted, i.e. pressure, mass flux, equilibrium exit quality and heat flux. They should obey the following equations:

Geometric similarity

$$\left[\frac{L_h}{D}\right]_P = \left[\frac{L_h}{D}\right]_M \tag{2-19}$$

Hydrodynamic similarity

$$\left[\frac{\rho_f}{\rho_g}\right]_P = \left[\frac{\rho_f}{\rho_g}\right]_M \tag{2-20}$$

Thermodynamic similarity

$$\left[\frac{\Delta h}{h_{fg}}\right]_P = \left[\frac{\Delta h}{h_{fg}}\right]_M \tag{2-21}$$

where, $\rho_f \; and \; \rho_g$ are the density of the liquid phase and the vapor phase. The subscripts 'M' and 'P' stand for model and prototype, respectively. The difference between the fluid-to-fluid scaling laws is the derivation of the scaling factor of mass flux, which is defined as the ratio of the mass flux of the original fluid (water) to that of the model fluid (R-12, R-134a, etc.). Based on CHF test data obtained in seven different fluids. Groeneveld et al., (1996) pointed out that the Weber is a reliable parameter for determining the scaling factor of mass flux. The present study

uses the Katto's model widely used for a scaling law and is expressed as follows:

$$\left[\frac{G\sqrt{D}}{\sqrt{\sigma\rho_f}}\right]_P = \left[\frac{G\sqrt{D}}{\sqrt{\sigma\rho_f}}\right]_M \tag{2-22}$$

The following procedures can be used to convert the R-134a CHF data from the scaling fluid to the water CHF data.

1. Calculate the density ratio of the liquid to the vapor. Find the pressure where the density ratio is same.
2. Calculate the mass ratio at the equivalent pressure as follows:

$$F_G = \frac{G_P}{G_M} = \frac{\left(\sqrt{\frac{\sigma\rho}{D}}\right)_P}{\left(\sqrt{\frac{\sigma\rho}{D}}\right)_M} \tag{2-23}$$

3. Calculate the latent scaling ratios defined as latent ratio of prototype fluid to vapor of model fluid as follows:

$$F_{\Delta h} = \frac{(h_{fg})_P}{(h_{fg})_M} \tag{2-24}$$

4. Calculate the heat flux scaling ratio by multiplying the latent scaling ratio and the heat flux scaling ratio as follows:

$$F_Q = F_G \times F_{\Delta h} \tag{2-25}$$

5. Calculate the critical heat flux from the heat flux scaling ratio as follows:

$$(q_{CHF})_P = F_Q \times (q_{CHF})_M \tag{2-26}$$

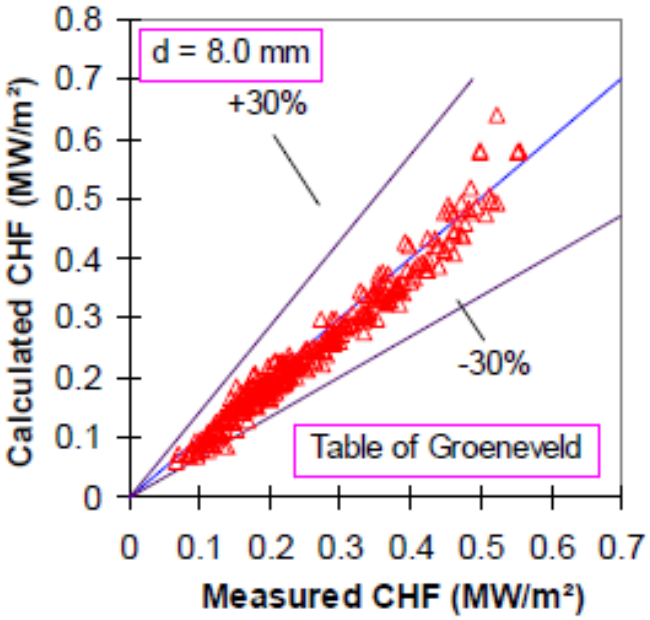


Figure 2.11 A comparison of the water equivalent CHF converted from Freon-12 data with the 1996 CHF look-up table (Cheng, X., 2003).

The water table data are transferred to Freon-12 equivalent conditions by using the Katto's fluid-to-fluid scaling law. The good agreement shows that the test results obtained in Freon-12 can be well transferred to water condition by using Kattos's scaling law shown in fig. 2.11.

2.5 Enhancement of CHF

Enhancements on CHF allow system to have improved operating conditions and safety margins. These can be obtained by applying various surface treatments, enhanced mixing oriented geometries, etc. Until the late 1980's, however, research on enhancement of CHF by surface modification was not active since the surface observation technology were not well

established, and some experimental findings indicated at that time that surface condition does not significantly effect on CHF. Those findings are consistent with the hydrodynamic instability model (Zuber, 1959) or macro layer dry-out model (Katto, 1984). However, several new experimental findings on CHF after 2000 indicated significant variations of CHF with modified surface conditions. Theofanous et al. (2002) observed 50% of CHF enhancement with surface treatments in water flow boiling test. Another CHF experiment with porous coated surface showed 200% enhancement for pool boiling compared with a plain surface (Chang et al., 2006).

General approaches proposed to enhance the critical heat flux include:

-Increased fluid mixing by modifying channel contour

-Increased heat transfer area, e.g. hypervapotron

-Increased bubble departure frequency by introducing acoustic perturbation

-Nano-particle suspended in fluid, i.e. nanofluid

-Increased surface wettability, e.g. Oxidation on the heating surface

However, the understanding on CHF enhancement mechanisms and supporting experimental databases are still significantly limited. Thus, additional research on CHF enhancement with pool and flow boiling conditions are needed.

2.5.1 Nano-fluid application for CHF enhancement

Nano-fluids, with their reduced thermal resistance and improved heat transfer properties, are a potential choice for these working fluids since late 90s. There are a large number of

engineering systems like thermal application, cooling package in electronics as well as nuclear engineering that can take advantage of such fluid. “Nanofluid” refers to a fluid in which nanometer sized particles are suspended in a fluid, usually a liquid (Choi et al., 1995). Practical experimental tests with uniformly distributed nanoparticles for CHF measurements have been conducted by several researchers to validate the existence of pool boiling CHF prediction model. However, a few flow boiling CHF enhancement experimental studies with surface modifications have been conducted so far. A summary of those efforts are listed in table 2.1.

Table 2.1 The pool and flow boiling CHF enhancement studies with surface modifications.

Reference	Boiling condition	Surface modification	CHF enhancement (%)
Dhir and Liaw, 1989	Pool Boiling	Oxidation film	~ 100%
You et al., 2001	Pool Boiling	Nanofluid (Al_2O_3)	~ 200%
Bang et al., 2004	Pool Boiling	Nanofluid (Al_2O_3)	~ 50%
Vassallo et al., 2004	Pool Boiling	Nanofluid (silica)	~ 60%
Kaviany et al., 2001	Pool Boiling	Nano porous coating	~ 70%
Kim et al., 2008	Flow Boiling	Nanofluid (Al_2O_3)	~ 35%

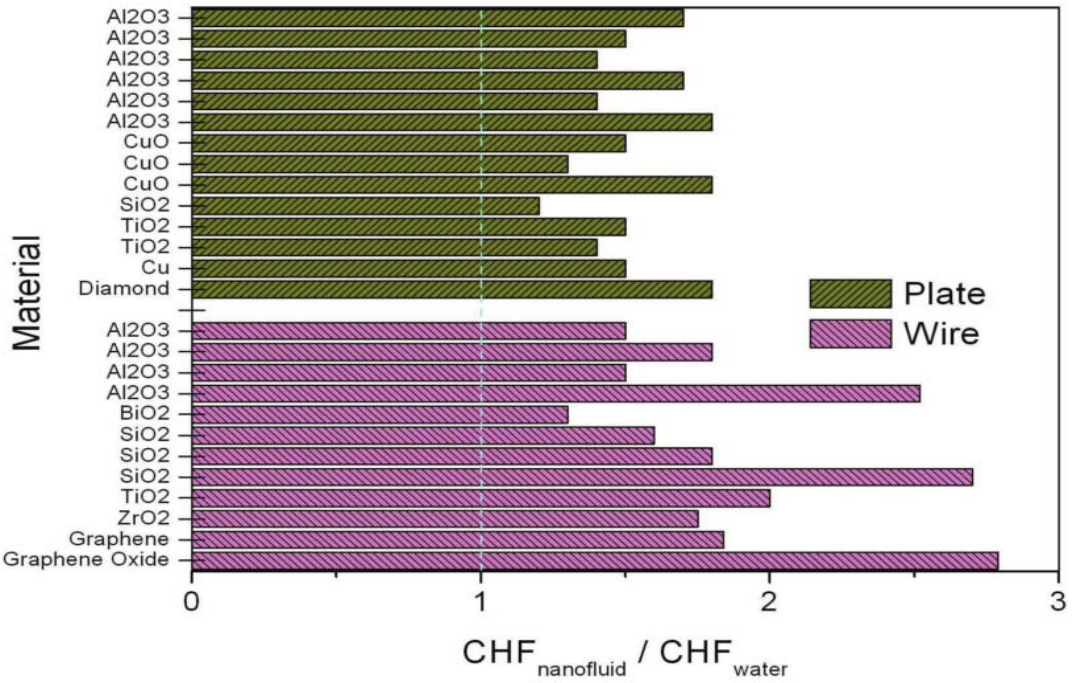


Figure 2.12 The experimental results of CHF values for both plates and thin wires (Kim H.D., 2011).

Nanotechnology based designer fluids developed by stably suspending nanoparticles (typically of length 1-100 nm) in conventional heat transfer liquids are termed as nano-fluids. Review papers (Choi et al., 1995; Das et al., 2006) include various aspects of this new research field including the history of technology development. It is clear that these technologically enhanced fluids have thermal properties that may be quite different from their base fluid. It has been shown that in one of the cases a small amount (less than 1% by volume) of addition of nanoparticles to the fluid in one case increased the thermal conductivity by a factor of two (Choi et al. 1995). From the literature available, however, it is apparent that the reported enhanced heat transfer rates are beyond just the effect of enhanced thermal conductivity (Das et al. 2006).

Though different mechanisms have been proposed, the scientific community still does not agree on an explanation as to how the nanoparticles enhance the heat transfer properties of the fluid.

Inspired by the notable outcomes of these pool boiling studies, the application of nano-fluid coolants into nuclear reactor or other thermal applications have been investigated by some researchers (see figure 2.11; Kim, H.D. et al., 2011; Jacopo et al., 2007). However, the thermal and hydraulic conditions of interest for those applications are under flow boiling conditions. The literature of surface modification by nanoparticle deposition in flow boiling condition is in the early stage of investigation. The conclusion from nano-fluid deposition studies in flow boiling condition (Kim et al., 2008) is that addition of nanoparticles in the working fluid provides the particle deposition by boiling and generates a surface with enhanced wettability and reduced the contact angles.

2.5.2 Surface modification application for CHF enhancement

Metallic or ceramic porous coatings on heating surfaces for pool and flow boiling have been evaluated by several research groups. It is observed that porous coated surfaces induce an increased number of small scale cavities on the surface, i.e. nucleation sites. Bubble release hinders the development of film boiling conditions.

Sarwar and Jeong (2007) conducted sub-cooled water flow boiling CHF enhancement with porous surface coatings experiments. The effect of micro-porous and nano-porous coated surfaces in vertical tubes was investigated under flow boiling tests at ambient pressure. Greater CHF enhancement was found with micro-porous coatings than with nano-porous coatings. Al_2O_3

micro porous coatings with particle sizes <10 micrometer and coating thickness of 50 micrometer showed the best CHF enhancement. Maximum increase in CHF was about 25% for micro-porous Al_2O_3. They concluded that a high nucleation site density and an optimized cavity structure are required for CHF enhancement.

Chang and You (2005) used alumina, diamond and silver particles (1–70 μm) as the coating material to test in pool boiling experiment with FC-72 (refrigerant) at atmospheric pressure. The particles adhered to the surface due to Van der waals molecular attraction forces. Significant reduction in wall superheats (50%) and an increase in CHF (32%) were reported. This simple and economical coating technique produced highly enhanced nucleation with lower incipient superheat and enhanced CHF compared with an uncoated surface.

Vemuri and Kim (2001) performed a pool boiling heat transfer experiment from a nanoporous coated surface immersed in a saturated FC-72 at atmospheric pressure (101 kPa). The diameter of the Alumina nanoporous surface ranged from 50 to 250 nm. They compared the results of a nanoporous surface with a plain surface and obtained a decrease of 30% in the incipient superheat and 50% of CHF enhancement with nanoporous surfaces.

Many researchers have studied on porous coating effect on pool boiling CHF enhancement. However, the effect of micro-porous and nano-porous coating on CHF under flow boiling conditions has not been sufficiently investigated. Thus, the effect of surface coatings on CHF enhancement during flow boiling is needed further study.

Nomenclature

English Symbols

Bo	Boiling number $\left(\mathrm{Bo} = \frac{q_{CHF}}{h_{gf}G}\right)$
cp	heat capacity of liquid at constant pressure
C	Kutateladze constant
C_1	a function of equilibrium quality proposed by Tong
CHF_D	Critical heat flux at certain diameter (D)
D	channel diameter
D_B	Bubble departure diameter
D_e	Equivalent diameter
f	friction factor
F_G	Scaling factor of mass flux
$F_{\Delta h}$	Scaling factor of sub-cooled enthalpy
F_Q	Scaling factor of critical heat flux
$F_{\Delta h}$	Scaling factor of sub-cooled enthalpy
g	Gravitation force (=9.81 m/s^2)
G	Mass flux [Kg/m^2]
h_{fg}	Heat of vaporization (latent heat)
h_f	Enthalpy of saturation fluid
h_{in}	Inlet enthalpy [KJ/Kg]
Ja	Jacob number $Ja = \frac{C_p(T_w - T_{in})}{h_{fg}} \frac{\rho_l}{\rho_g}$
K	Non-dimensionless parameter in Katto correlation
L_B	Heated length
L, L_h	Heated channel length
$\dot{m}$	Mass flow rate [Kg/s]
P	Pressure [Pa]
P_{out}	Pressure at outlet
P_{cr}	Critical pressure
$q_{CHF,sat,}$	Critical Heat flux at saturation flow condition (q_{co})
$q_{CHF,}$ q_C	Critical Heat flux
Re	Prandtl number $\left(\mathrm{Pr} = \frac{\mu_f c_{pf}}{k_f}\right)$
T	Temperature (C°)
U_B	Bulk fluid velocity
W	Weber number $\left(\mathrm{We} = \frac{G^2 D}{\rho_f \sigma}\right)$

x_{out}	Thermodynamic quality at outlet $\left(x = \frac{h-h_f}{k_{fg}}\right)$
y^*	Dimensionless wall distance

Greek Symbols

ρ_v	Density of vapor
ρ_g	Density of gas
σ	Surface tension
ρ_l	Density of liquid
ρ_f	Density of fluid
δ	Micro layer thickness
ε	Roughness
β, θ	Static Contact angle at atmospheric pressure condition [°]
ϑ	Bulk fluid mean velocity [m/s]
μ	Viscosity [kg/m-s]
Δh_{in}	Sub-cooled Inlet enthalpy [KJ/Kg]
ΔTsub	Sub-cooled temperature [C°]

Acronyms

BWR	Boiling Water Reactor
CHF	Critical Heat Flux
DO	Dry-Out
DNB	Departure from Nucleate Boiling
M	Modeling fluid
P	Prototype fluid
PWR	Pressurized boiling Water Reactor

References

Ahmad, S.Y., 1973, “Fluid to fluid modeling of critical heat flux: a compensated distortion model.” International Journal of Heat and Mass Transfer, 16(3), pp. 641-662

Bang, I. C., Chang, S. H., 2004, "Visualization of the sub-cooled flow boiling of R-134a in a vertical rectangular channel with an electrically heated wall", Int. J. of Heat and Mass Transfer, Vol. 47, pp. 4349-4363

Bang, I. C., Chang, S. H., 2005, "Boiling Heat Transfer Performance and Phenomena of A120 3-Water Nano-fluids from a Plain Surface in a Pool", Int. J. of Heat and Mass Transfer, Vol. 48, pp. 2407-2419

Bergles, A.E.1963, “Subcooled burnout in tubes of small diameter” AMSE paper

Corre, Jean-Marie 2007, “Flow regimes and mechanistic modeling of critical heat flux under sub-cooled flow boiling conditions” Doctoral Dissertation, Mechanical Engineering Department, Carnegie Mellon University

Chang, J.Y., You, S.M., 2005, “Enhanced boiling heat transfer from micro-porous surfaces: effects of a coating composition and method”, Int. J. Heat and Mass Transfer 40 (18) 4449–4466.

Choi, S.U.S. et al., 1995, “Enhancing thermal conductivity of fluids with nanoparticles” Argonne National Lab. Annular report

Collier, John, Thome, John, 1996, “Convective boiling and condensation” chapter 2

Cheng , X. Muller U. 2003, “Review on critical heat flux in water cooled reactors” Master thesis, Forschungszentrum Karlsruhe

Chang, S.H., Y.H. Jeong, B.S. Shin, 2006, “Critical Heat Flux Enhancement”, Nuclear Engineering and Technology, Vol. 38 No. 8 December

Celata, G. P., Cumo, M., Mariani, A., 1994a, "Assessment of correlations and models for the prediction of CHF in subcooled flow boiling", Int. J. Heat and Mass Transfer, Vol. 37, pp. 237-255

Celata, G. P., Cumo, M., Mariani, A., Simoncini, M., Zummo, G., 1994b, "Rationalization of existing mechanistic models for the prediction of water subcooled flow boiling critical heat flux", Int. J. Heat Mass Transfer, Vol. 37, pp. 347-360

Celata G.P., Mariani A., Zummo G., M. and Gallo D, 1988, “Physical insight in the burnout region of water-sucooled flow boiling”, Rev. Gem. Therm., 37, pp. 450-458

Das, Wen, Wang, B.X., 2006, “Effect of surface wettability on nucleate pool boiling heat transfer for surfactant solutions”, Int. Journal of Heat and Mass Transfer 45 1739-1747

Dhir, V.K., S.P. Liaw, Framework for a unified model for nucleate and transition pool boiling, Journal of Heat Transfer, August 1989, Vol. 111 739-746

Doroshchuk, V.E. et al., 1975, “Investigations into burnout in uniformly heated tubes” AMSE paper

Fiori, P., Bergles, A.E., 1970, “Model of critical heat flux in subcooled flow boiling” Int. Heat transfer conference

Groeneveld, D.C., et al., 1996 “The 1995 look-up table for critical heat flux in tubes” Nuclear Engineer and Design, Vol. 163, pp 1-23

Groeneveld, D.C., et al., 2006 “The 2005 look-up table for critical heat flux in tubes” Nuclear Engineer and Design, Vol. 237, pp 1909-1922

Gunther F.C., 1951,“Photographic study of surface-boiling heat transfer to water with forced convection” Trans. AMSE, 73, pp. 115-123

Ha, S.J., No, H.C., 1998, “A dry-spot model for transition boiling heat transfer in pool boiling” Int. J. Heat and Mass Transfer, Vol. 41, No 23, pp. 3771-3779

Issam Mudawar, et al., 2009, “Flow boiling in a micro-channel coated with carbon nanotubes”, IEEE Trans. Components and packing technologies, Vol. 32, No. 3

Issam Mudawar, 1998 “Critical Heat Flux in small diameter channels” sixteenth symposium on energy, pp58-70

Jacopo, Buongiorno, S.J. Kim, I.C. Bang, L.W. Hu, “Surface wettability change during pool boiling of nanofluids and its effects on critical heat flux”, Int. J. Heat and Mass Transfer 50 (2007) pp 4105-4116

Kutateladge, S. S., Leont’ev, A. I., “Turbulent boundary layers in compressible gases”, D.B. Spalding, trans., Academic press, New York, 1964

Katto, Y., 1978, “A Generalized correlation of critical heat flux for the forced convection boiling in vertical uniformly heated round tubes.” International Journal of Heat and Mass transfer,

21(12), pp. 1527-1542

Katto, Y., et al., "A new hydrodynamic model of critical heat flux, applicable widely to both pool and forced convection boiling on submerged bodies in saturated liquids", Int. Journal of Heat and Mass Transfer Vol. 26, No. 6. 389-399, 1983

Katto, Y., Ohno, H., "An improved version of the generalized correlation of critical heat flux for the forced convective boiling in uniformly heat vertical tube" Int. J. Heat Mass Transfer, Vol. 27 No 9. 1641-1648, 1984

Katto, Y., 1990, "A physical approach to critical heat flux of subcooled flow boiling in round tubes", Int. J. Heat Mass Transfer, Vol. 33, pp. 611-620

Kolev Nikolay I., 2001 "Mutiphase Flow Dynamics 4" Springer

Kandlikar, Satish G. 2001, "A theoretical Model to predict pool boiling CHF incorporating effects of contact angle and orientation", Journal of Heat Transfer, Vol. 123

Kaviany, M., Scott G. Litter, "Pool-boiling CHF enhancement by modulated porous layer coating: theory and experiment", Int. J. Heat Mass Transfer 44 (2007) 4287–4311.

Kim, H., Kim, J., Kim, M., 2006, "Experimental study on CHF characteristics of water-TiO 2 nanofluids", Nuclear Engineering and Technology, Vol. 38, No. 1

Kim, H.D. 2011, "enhancement of critical heat flux in nucleate boiling of nanofluids: a state-of-art review", Nanoscale Research Letters, 6:415

Kim, S. J., Bang, I. C., Buongiorno, J., Hu, L. W., 2007, "Surface wettability change during pool boiling of nanofuids and its effect on critical heat flux", Int. J. of Heat and Mass Transfer, Vol. 50, pp. 4105-4116

Liehard, J.H., Dvir V.K., 1973, "Hydrodynamics prediction of peak pool-boiling heat fluxes from finite bodies", Journal of Heat transfer, Volume 95, Issue 2, pp 152-159

Liaw, Shin-Pin 1988, "Experimental and Analytical study of nucleate and transition boiling on vertical surfaces", Doctoral Dissertation, Mechanical Engineering Department, UCLA

Srinivas Vemuri and K.J. Kim, Pool boiling of saturated FC-72 on nanoporous surfaces, Int. J. Heat and Mass Transfer 32 (2005) (1–2), 27–31.

Sarwar, S.M., Jeong, Y.H., Chang, S.H., 2007, "Sub-cooled flow boiling CHF enhancement with porous surface coating", Int. J. Heat and Mass Transfer 50 3649-3657

Tong, L.S., 1968, “A phenomenological study of Critical Heat Flux” ASME paper 75-HT-68

Tong, L. S., 1975, "Boundary layer analysis of the flow boiling crisis", Int. J. Heat and Mass Transfer, Vol. 11, pp. 1208-1211

Tong, L. S., Tang, Y. S., 1988, "Boiling heat transfer and two-phase flow", Taylor & Francis, 2 nd Ed.

Theofanous, T.G. et al., 2002a, “The boiling crisis phenomenon Part I: nucleation and nucleate boiling heat transfer”, Experimental Thermal and Fluid Science 26, pp. 775-792

Theofanous, T.G. et al., 2002b, “The boiling crisis phenomenon Part II: dry out dynamics and burnout”, Experimental thermal and Fluid Science 26, pp. 793-810

You, S.M., J.H.Kim, “Effect of nanoparticles on critical heat flux of water in pool boiling heat transfer”, Applied physics letters, Vol, 83, No. 16 October 2003

You, S.M., Chang, J.Y., “Enhanced boiling heat transfer from micro-porous surfaces: effects of a coating composition and method”, Int. J. Heat and Mass Transfer 40 (1998) (18) 4449–4466.

You, S.M., You, C.N. “Ammerman, Enhancing small-channel convective boiling performance using a microporous surface coating”, Trans. ASME 123 (2001), 976–1083

Vassallo, peter, et al., “Pool boiling heat transfer experiments in silica water nano-fluids”, Int. Journal of Heat and Mass Transfer 47 (2004) 407-411

Vemuri, Srinivas, Kim, K.J., 2001, “Pool boiling of saturated FC-72 on nanoporous surfaces”, Int. J. Heat and Mass Transfer 32 (1–2), 27–31

Weisman, J., Pei, B.S., 1983, “Prediction of critical heat flux in flow boiling at low qualities” Int. J. Heat Mass Transfer, Vol. 10 No 10, pp10

Zuber, N., 1959, “Hydrodynamic aspects of boiling heat transfer” PhD thesis, June 1

3.Experimental Descriptions

In this chapter, the experimental apparatus setting and data acquisition system used in the current sub-cooled flow boiling experimental loop are introduced. The surface treatment techniques utilizing atmospheric pressure plasma coating is also reported. The major components of the experimental apparatus include a refrigerant loop and an electrically heated test section with and without surface treatment. Instruments include thermocouples, pressure transducers, flow meters, etc. Most of the signals are collected by a data acquisition system (HP75000 serial B), which is connected to a personal computer (PC). A high-speed digital camera with high resolution is used to record bubble and nucleation site images from side view.

3.1 Sub-cooled Flow Boiling Experimental Test Facility

A test loop in the Air Conditioning and Refrigeration Center (ACRC) at the University of Illinois at Urbana-Champaign is utilized for the experiment. The loop was originally designed and built in 1989 to determine two-phase heat transfer coefficients for alternative refrigerants. Modification was made by Wu (2007), Chen (2007), Zou (2010), and author (2011) to observe and measure the sub-cooled boiling heat transfer phenomena with different perspectives.

Mainly critical heat flux measurement experiments and visualization have been carried out with R-134a as a working fluid with forced convection boiling condition in current research. The experimental apparatus used in this study consists of: (1) a liquid reservoir of R-134a, (2) a

cooler and a gear pump, (3) a test section including copper based heating block and visualization channel, and (4) a data acquisition system. The voltage signals from the thermocouples embedded in the copper-heating block were recorded using a computer-controlled data acquisition system. Figure 3.1 shows the schematic diagram of the experiment setup. Refrigerant R-134a is used as the working fluid in this experiment. The objective of this experimental apparatus is to observe the sub-cooled flow boiling heat transfer phenomena and collect the critical heat flux data points with wide ranges of inlet temperature, mass flow rate of R-134a, system pressures, and different wetting condition of heating surface.

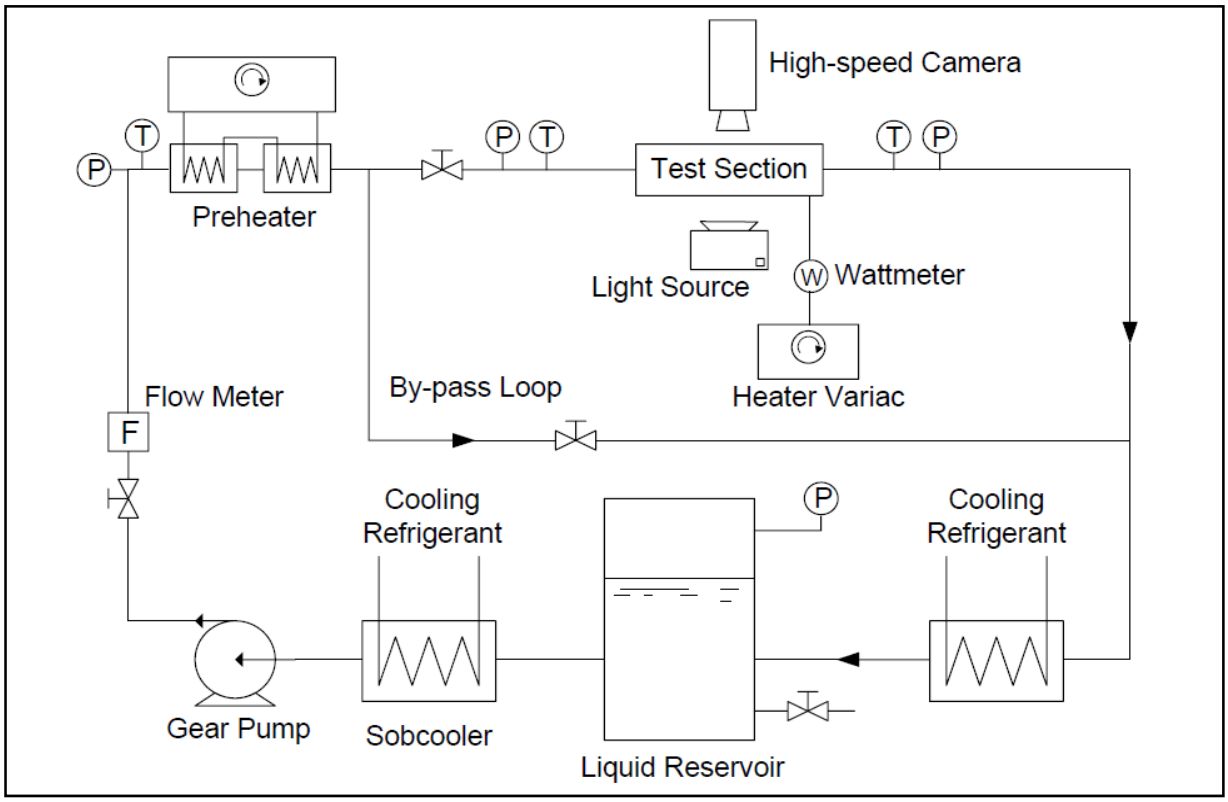


Figure 3.1 The schematic diagram of the R-134a forced convection boiling test loop.

3.1.1 Overall test loop configuration

The R-134a fluid pathway and equipment component setting are explained below. A liquid reservoir of R-134a is used to store refrigerant and stabilize the system pressure. A typical and widely used refrigerant, R134a, is chosen as the working fluid for its relatively low critical pressure, saturation temperature, and latent heat. A list of the physical and thermal properties is given in Table 3.1. A gear Pump, manufactured by Micro-Pump ®, provides a variable range of mass flow rates, up to 4 LPM (liter per minute) which are measured by a Coriolis-type mass flow meter, manufactured by Micro-Motion ®. An electric pre-heater controls inlet sub-cooling temperature of R-134a at the entrance to the test section, and is installed at upstream of test section. The pre-heater consists of three copper tubes 1.8 meters in length and 9.525 mm in outer diameter and assembled in a serpentine shape. The outside of the tubes is wrapped with twelve electrical heating stripes with variable powers. Ten of these twelve stripes are controlled by 4 switches and provide constant power, while providing a different power level controlled by a 115 Volt Variac. The preheater is used to adjust the degree of the sub-cooling of the fluid entering the test section. A throttling valve located at the upstream of the test sectionis used to avoid flow fluctuations, which usually occur at low flow conditions. The rectangular test section is heated from the bottom by electric copper heater, and three quartz windows are installed on the other three sides of the test section. This enables direct observation of the flow boiling process through a high-speed visualization camera. A cooling component is installed downstream of the test section. It cools the refrigerant exiting from the test section, which is especially important for a flow boiling experiment to maintain a constant system pressure. Another cooling sub-loop is

installed immediately upstream of the gear pump and downstream of the liquid reservoir, which ensures there is no refrigerant vapor entering the pump. The working fluid for these two cooling sub-loops is R-12, which is then cooled in two commercial water chillers. A fine adjustment in the degree of sub-cooling temperature is made through a combination of adjustments in the preheater's power along with a valve opening of the heated and cooling water lines of the coolers. Numbers of type K thermocouples and BEC strain-gage type pressure transducers are installed in the loop to measure temperature, applied heat flux at the copper surface, and fluid pressure information at several locations (see Fig. 3.1).

Table 3.1 The physical and thermal properties of R134a at different pressures.

P (bar)	T_{sat} (K)	ρ_l (kg/m3)	ρ_v (kg/m3)	$C_{p,l}$ (J/kg·K)	h_{fg} (J/kg)	σ (N/m)
2.0	263.07	1327.40	10.012	1315.4	206.02	1.303E-02
2.5	268.87	1308.80	12.394	1329.7	201.81	1.218E-02
3.0	273.82	1292.60	14.770	1342.9	198.10	1.146E-02
3.5	278.18	1278.00	17.147	1355.2	194.72	1.084E-02
4.0	282.08	1264.70	19.529	1367	191.61	1.029E-02
4.5	285.63	1252.30	21.918	1378.4	188.70	9.791E-03
5.0	288.88	1240.80	24.317	1389.4	185.97	9.340E-03
5.5	291.90	1229.90	26.729	1400.2	183.37	8.925E-03
6.0	294.72	1219.50	29.155	1410.9	180.89	8.542E-03
6.5	297.37	1209.70	31.596	1421.4	178.51	8.186E-03
7.0	299.86	1200.20	34.054	1431.8	176.21	7.852E-03
7.5	302.23	1191.10	36.530	1442.3	173.98	7.539E-03
8.0	304.48	1182.20	39.025	1452.7	171.81	7.243E-03

3.1.2 Test section

A detailed drawing of the test section is shown in figure 3.2. The test section consists of a 1 m long rectangular channel made with stainless steel, a copper block heating element with

cartridge heaters, and three quartz windows for visual observations. The rectangular copper heating block, 12.7 mm by 107.95 mm with and length, respectively, is installed in the middle of a straight horizontal rectangular stainless steel flow channel. The dimensions of the flow channel are 1 m by 12.7 mm by 12.7 mm (length, with, and height, respectively). The entrance length, which is measured from the entrance of the straight flow channel to the leading edge of the test section, is 490 mm (Fig. 3.2). The ratio of entrance length to the flow channel hydraulic diameter is calculated as 38.58. This is much larger than the recommended entrance length ratio values of ~19 to ~24, calculated from experimental conditions investigated, such as system pressures ranging from 400 kPa to 800 kPa and mass flux ranging from 125 kg/m^{2}s to 255 kg/m^{2}s . The value of the required entrance length to hydraulic diameter ratio is evaluated by,

$$\frac{L}{D_h} \approx 4.4(Re)^{1/6} \tag{3-1}$$

The test section is heated by seven cartridge heaters, which provide a maximum total power of 5050W (750W × 7). These seven heaters are divided into three groups with a 2/3/2 pattern, each of which can be turned on and off independently. The electric power level is controlled by an autotransformer and measured by voltmeter and ammeter instruments in the power circuit. Each of these seven cartridge heaters contains one continuous 76.2 mm long heated section. All heaters have an INCOLOY sheath to enhance the heat conduction from heaters to copper base block.

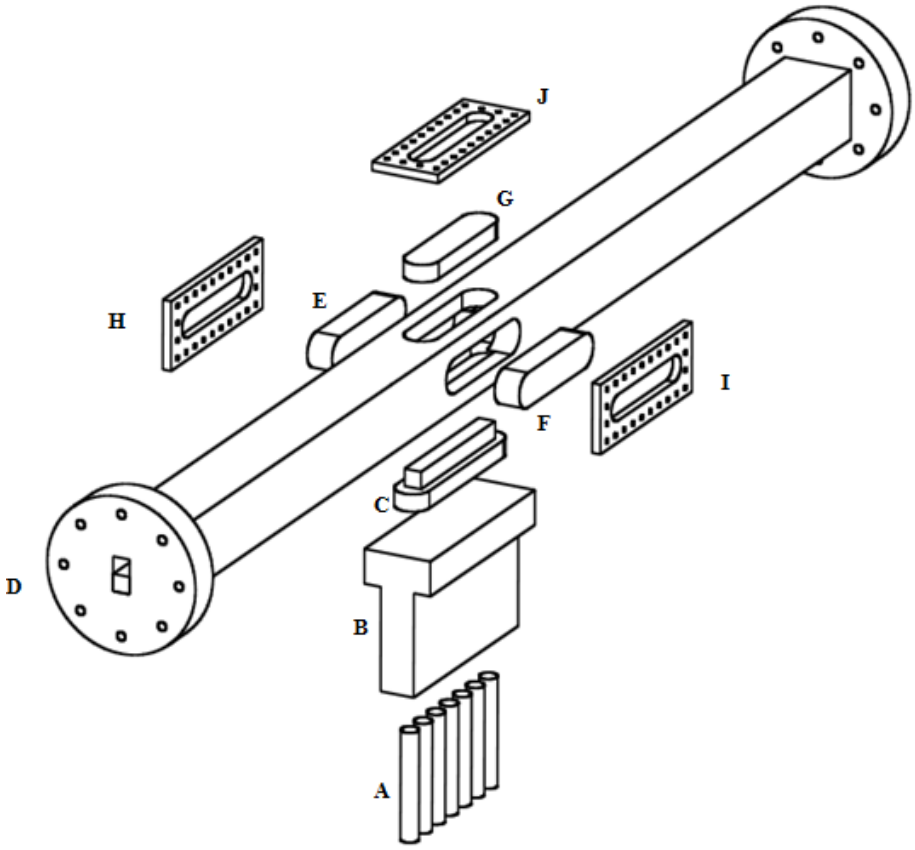


Figure 3.2 An exploded view of the test section assembly.

A - Cartridge heaters
B – Copper base block
C – Heating block
D – Stainless steel flow channel
E – Rear quartz window
F – Front quartz window
G – Top quartz window
H – Rear stainless steel window mounting
I – Front stainless steel window mounting
J – Top stainless steel window mounting

To obtain a uniform heat flux and temperature profile close to the heating surface, it is recommended to turn on either all of these 7 cartridge heaters or the center 3 ones. Eight type K thermocouples are inserted into the copper block to monitor temperature and this temperature information allows one to determine the heat flux. A numerical study by using FLUENT® demonstrate that, for the case, when the center 3 cartridge heaters are turned on, a nearly uniform temperature profile and thermal uniformity over the entire heating surface both can be obtained compared to the case where 7 cartridge heaters are turned on.

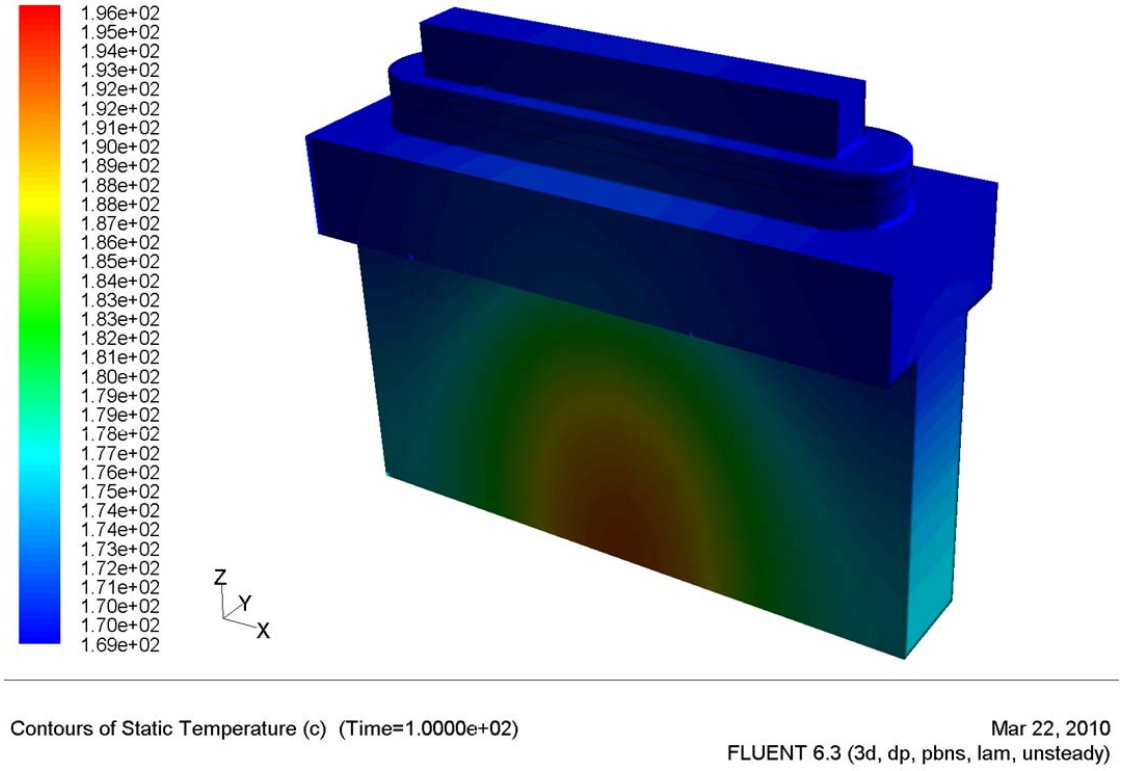


Figure 3.3 The temperature profile on heating block walls at 100 seconds after critical heat flux occurring with power on (Zou, Ling, 2010).

During the experiments, the critical heat flux can be observed by monitoring sudden surface temperature jump due to the vapor film covering heating surface. The film boiling phenomenon normally takes place at the post-CHF stage, which gives a much smaller heat transfer coefficient compared to nucleate boiling heat transfer. To avoid an accident scenario with burnout or components damage, the electric power applied on the heating block has to be shut off promptly when it reaches the CHF point. The maximum temperature the INCOLOY sheath can withstand is approximately 800ºC, while the silicone rubber O-ring, which seals the gap between the flow channel and the heating block, can only sustain temperatures lower than 250 ºC. To assure there is no accidental scenario, a transient heat transfer simulation was carried out with FLUENT® to calculate the temperature profile inside the copper base block and heating block at the post-CHF stage. Conservative boundary conditions were assigned, i.e., the heat transfer coefficient from the heating block to fluid side drops to zero, and heat can only be removed by natural convection and radiation heat transfer at surfaces exposed to the air. 100 seconds of post CHF transient heat transfer simulation has been done with FLUENT® to predict the temperature profiles in the heating blocks. The simulation obtained a maximum critical heat flux in 800kPa pressure, of around 6.0×10^5 W/m^2. The temperature profile is shown in Figure 3.3. The simulation results show that, at 100 seconds after CHF occurs, the temperature at the O-ring is around 169 ºC, and the maximum temperature on the INCOLOY sheath is around 196 ºC. This simulation result ensures that when CHF occurs, there will be enough time to turn off the heaters.

Baseline heating blocks with copper and surface treated copper heating block with atmospheric pressure plasma coating technique were employed separately to study sub-cooled

flow boiling performance and critical heat flux (CHF) with different surface condition. Copper was selected as the base material for both heating block due to its very high thermal conductivity, ~400W/m-K, and good reaction feasibility with atmospheric pressure plasma coating. The heating block with a copper-heating surface was machined from a pure copper block. To make a heating block with a different surface condition (such as a reduced static contact angle, more hydrophilic surface), atmospheric pressure plasma coating was utilized (see fig. 3.4). The detail measurements of static contact angle/ oxidation layer thickness are presented in chapter 5, the changes in surface interface morphology observations are conducted by using SEM and XPS is reported.



Figure 3.4 Pictures of static contact angle of liquid drop test with/ without AP-plasma treatment on copper surface

One main reason to utilize atmospheric pressure plasma surface coating is that this technique does not require highly restricted vacuum condition to treat and modify the copper surface. Atmospheric pressure plasma spray device (Dielectric Barrier Discharge (DBD) AP-

Plasma), was utilized to modify the copper surface which became more of a hydrophilic surface with reduction of static contact angle. After surface treatment, the contact angle measurement and coating layer thickness measurements was conducted to observe and quantitatively understand the change on the heating surfaces.

To measure the heating surface wall temperature and heat flux, eight type-K thermocouples were installed in the copper-heating block. The heat flux can be calculated from the temperature gradient in the copper-heating block, and the wall temperature can be calculated from the temperatures measured at the thermocouples located very close to the heater wall, with a distance correction applied. The detailed test section dimensions and locations of thermocouples are shown in Figure 3.5 and 3.6.

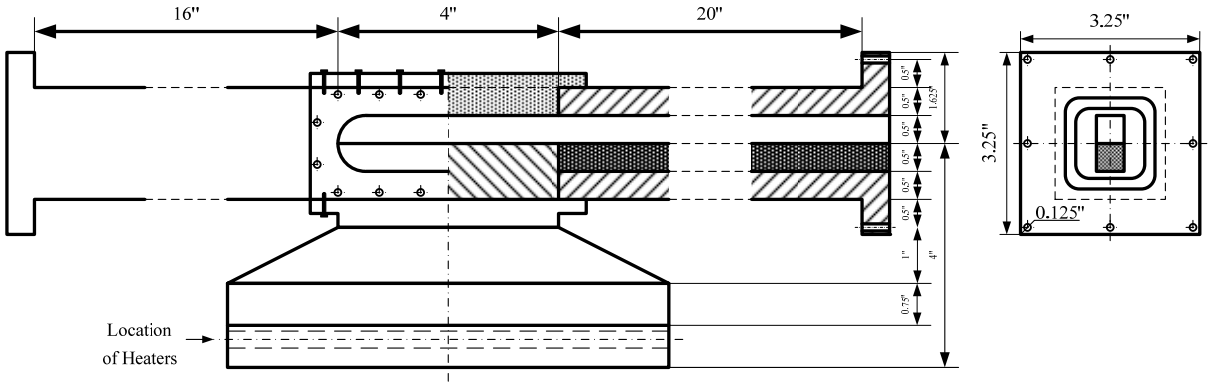


Figure 3.5 The schematic diagram of the detail design information of the test section.

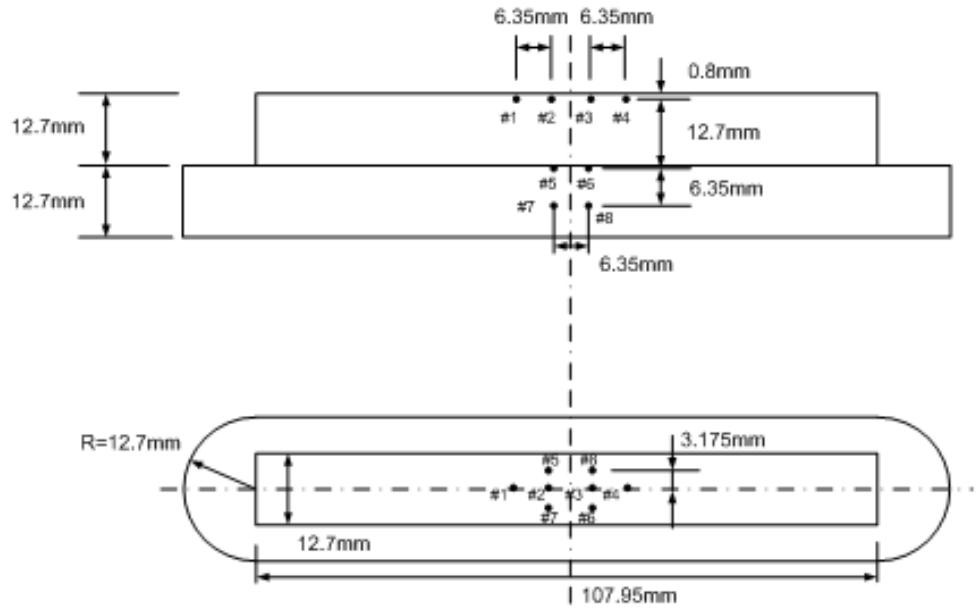


Figure 3.6 The schematic drawings of test sections and locations of thermocouples in side/ top view.

3.1.3 Data acquisition and flow visualization systems

The signals recorded during the flow boiling heat transfer experiment include directly measured quantities, such as temperature, pressure, mass flow rate, electric voltage, current, etc. Quantities calculated from the directly measured quantities, such as power and heat flux are also recorded. An array of instruments, such as thermocouples and pressure transducers, is employed to measure these quantities. A data acquisition system for temperature, pressure and mass flow rate signals includes HP 75000 serial B data acquisition equipment and a PC. In addition, a high-speed digital camera was used to observe the small-scale bubble dynamics, which were recorded in a second PC. Types K and T thermocouples are used for temperature measurements. All

thermocouples are calibrated using an ice bath reference and are considered valid from 5 ºC to 100 ºC with an uncertainly of ±0.1 ºC. The working fluid inlet and outlet temperatures are directly measured with thermocouples inserted in the flow channel. Eight thermocouples are installed in the heater block, so that the heat flux then can be calculated from the temperature gradient inside the heating block. The uncertainty for heat flux measurements is estimated to be ±3%, given the maximum temperature measurement error of 0.75%. The heating surface wall temperature can be calculated from temperatures measured at locations immediately beneath the surface by compensating for the temperature difference due to the distance from the wall surface to the thermocouples. The saturation temperature is calculated from the measured system pressure. The bulk temperature, Tb, is an average value of inlet and outlet temperatures. Two BEC strain-gage type pressure transducers are installed before the pre-heater inlet and the test section inlet. Both transducers are calibrated using a dead weight tester with an uncertainly of ±900Pa with a range of 0~2100kPa). The liquid mass flow rate is measured by a model D12 mass flow meter (inertial flow meter or Coriolis flow meter) manufactured by Micro-Motion. A pair of U-shaped tubes in the flow meter vibrates as fluid flows by, and a current which depends on the frequency of vibration is delivered to the data acquisition system.

A Photron FASTCAM ultima 1024 High Speed Video Camera System is used to photograph the boiling phenomena on the test section through the side and top windows. Fig. 3.7 shows the camera and channel arrangement. In order to achieve the highest possible resolution and eliminate errors in calibration, the camera is mounted on a tripod, and the lens is fixed at a constant focal length, resulting in a fixed viewing area of approximately 26×13 mm^2. This

system can acquire images at up to 12000frames/s employing a high intensive light supply. In these experiments, frame speeds between 1000 and 4000 frames/s are used. The high-speed images are recorded in a computer by an IEEE 1394 fire wire connection. Various magnifications are provided by choosing different micro lenses, ranging from 0.58× ~ 7×, which allow detailed observation of the liquid-vapor activity on the heated surface. Table 3.2 shows the camera lens magnification calibration results and conversion table with respect to pixel. The accuracy of conversion for different magnification is estimated to be within ±1.0%.

In order to achieve the highest possible resolution and best fidelity, the camera is mounted on a 65mm XYZ linear stage and the focal length of the lens is fixed at a constant value, which is about 5 cm. The XYZ linear stage provides a smooth and stable camera positioning function with travel distance of 30/30/45(X/Y/Z) mm, and sensitivity of 0.1 mm. The camera is calibrated by comparing the size of an object in the image and its real size which is measured with a micrometer. The uncertainly of the image is estimated to be 1 pixel and therefore the error depends on the image size and the lens magnification selected.

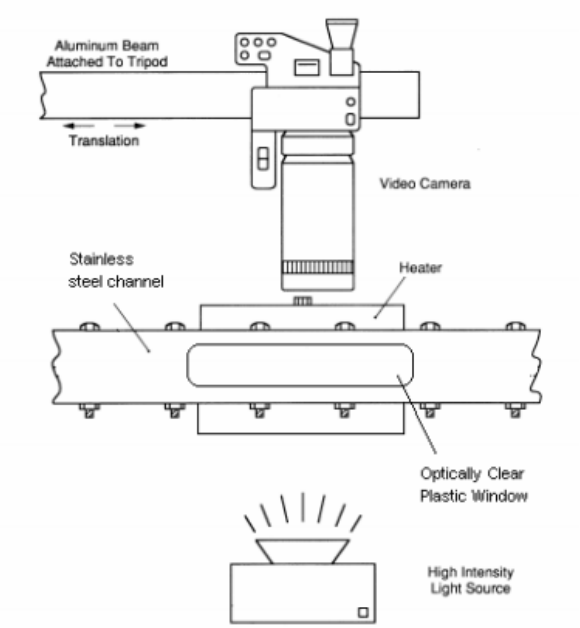


Figure 3.7 A Camera and light arrangement for flow visualization tests (Top View).

Table 3.2 The lens Calibration and index ratio with respect to pixel.

Magnification factor	Pixel/mm	μm/pixel
1	50.04	19.99
2	103.07	9.70
3	157.61	6.34
4	209.14	4.78
5	255.51	3.91
6	314.96	3.18
7	365.47	2.74

3.2 Experimental Operating Conditions and Uncertainty Analysis

3.2.1 Experimental operating conditions

In this present study, the experiments on CHF with R-134a were performed with mass

fluxes varying from 125 to 225kg/m^{2}s, pressures from 400 kPa to 800 kPa, and the sub-cooling temperatures from -5 ˚C to 17 ˚C. Table 3.3 summarizes the experimental test condition. A series of experiments have been performed for R-134 forced convection boiling with difference system pressure and mass flux and sub-cooling temperature at the inlet. To achieve accurate critical heat flux data in this study, the following procedures were utilized to prepare for data acquisition as follows:

Table 3.3 The summary of experimental opering conditions for CHF measurement test.

Experimental parameter	Experimental condition
Pressure (kPa)	400~ 800 kPa
Mass flux of R-134a (kg/m^{2}s)	125~225 kg/m^{2}s
Sub-cooling temperature of inlet (˚C)	-5 ~ 17 ˚C

Critical Heat Flux measurement procedure

1) Turn on the cooling system to have a high quality of liquid phase of R-134a in whole test loop, and a cooling water loop was used to control the loop temperature.

2) A stable flow rate was obtained using the gear pump, which was controlled by a flow meter (Variac) located upstream of test section.

3) After the system pressure was stabilized, the inlet sub-cooling temperature was controlled to a desired level using the pre-heater, and mass flux was set as a selected

value using a flow meter (Variac).

4) The power to the test section was increased gradually in small steps, at each power level, the test parameters are allowed to stabilize for several minutes to achieve a quasi-steady state condition before raising the power lever again.

5) Just prior to CHF occurrence, all test conditions are stabilized and the power to the test section is raised in incremental steps of 10~15W.

6) The onset of CHF is defined as the condition where the surface temperature of the test section rises dramatically.

7) Right after the CHF occurrence, the power supply for the heater was shut down to avoid damage to the heating block and test section (when the wall temperature reaches a pre-determined set point (typically ~ 80˚C, the power supplied to the heater rod is manually tripped). With continued coolant flow and lower heat flux, the wall temperature starts to decrease till nucleate boiling resumes again.

8) After investigating on raw data from data collection system, the heat flux and superheated surface temperature are selected at each steady state equilibrium condition. Then, a single boiling curve of R-134a with fixed pressure, mass flux, and inlet sub-cooled enthalpy condition is generated.

3.2.2 The uncertainty analysis and experimental condition

The heat flux functions as the experimentally determined parameters; it can be calculated in two manners such as thermal heat flux, electrical heat flux. Thermal heat flux $[w/m^2]$ is calculated from the gradient of the temperature profiles in the copper block

$$q'' = -k\frac{\Delta T}{\Delta x} \tag{3-2}$$

where, k is the thermal conductivity of the copper block $[w/k]$, ΔT is the temperature difference between two thermocouples lying in the same vertical plane [˚C], and Δx is the distance [m] between the thermocouples. The uncertainty of thermal heat flux is calculated using the Holman uncertainty calculation method as follows (Holman, 2001):

$$\frac{\omega_{q''}}{q''} = \sqrt{\left(\frac{\omega_k}{k}\right)^2 + \left(\frac{\omega_{\Delta T}}{\Delta T}\right)^2 + \left(\frac{\omega_{\Delta x}}{\Delta x}\right)^2} \tag{3-3}$$

where, ω is the statistical uncertainty value for each variable.

$$\frac{\omega_{q''}}{q''} = \sqrt{(0.03)^2 + (0.015)^2 + (0.045)^2} = 0.0561 \tag{3-4}$$

The uncertainty in the vertical distance between two thermocouples embedded in the copper block was estimated to be $\pm 3\%$, which was determined from the positioning accuracy. The uncertainty of the thermal conductivity of the copper block was assumed to be $\pm 1.5\%$ based on thermo physical property table provided from the National Institute of Standards and Technology (NIST). The uncertainty of the temperature differential was estimated to be $\pm 4.5\%$

at the critical heat flux. Therefore, the total experimental uncertainty for the thermal heat flux was estimated to be $\pm$5.61% at the critical heat flux points.

Uncertainties for the electrical heat flux were estimated using same Holman method. The electrical heat flux was calculated by the following equation.

$$q_{CHF} = \frac{V \cdot I}{DL} \tag{3-5}$$

$$\frac{\omega_{q''}}{q''} = \sqrt{\left(\frac{\omega_V}{V}\right)^2 + \left(\frac{\omega_I}{I}\right)^2 + \left(\frac{\omega_D}{D}\right)^2 + \left(\frac{\omega_L}{L}\right)^2} \tag{3-6}$$

$\omega_{q''}$, is the uncertainty of critical heat flux. ω_V, ω_I, ω_D and ω_L are the uncertainties of the voltage, current, the width of heating block facing fluid, and the length of heating block facing fluid, which are estimated to be less than 4%, 4%,1.5% and 1.5%, respectively. The propagation of error method (Holman 2001) suggests the following estimates of electrical heat flux uncertainty:

$$\frac{\omega_{q''}}{q''} = \sqrt{(0.04)^2 + (0.04)^2 + (0.015)^2 + (0.015)^2} = 0.0604 \tag{3-7}$$

Therefore, the measurement uncertainty on the calculated value of the electrical heat flux is <$\pm$ 6.04%.

3.3 Surface Treatment (Atmospheric Pressure (AP) Plasma Coating)

3.2.1 Atmospheric pressure plasma coating

The atmospheric pressure plasma is well known for its great advantages in various kinds of industrial coating applications and has been widely used in manufacturing process including flat panel displays, thin films and semiconductor packaging. There has been enormous progress on atmospheric pressure plasma coating technique and diagnostics to suit these for different purposes. Especially metallic surface treatment with atmospheric pressure plasma technique is a very promising way to get hydrophilic surface (heat pipe, advanced condensation or boiling), or hydrophobic surface (self-cleaning, semiconductor industry) for various applications. Surface modifications of copper surface using atmospheric pressure plasma coating are carried out to enhance the surface wettability and reduce static contact angle. In this study, N2 atmospheric pressure plasmas are generated and their influence on surface modification has been investigated. (see Fig 3.8).

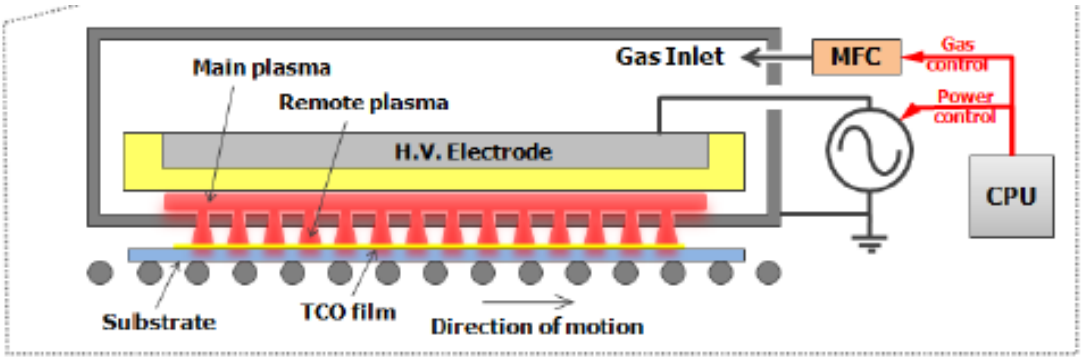


Figure 3.8 The schematic diagram of atmospheric pressure plasma coating device.

300 liter per minute of N2 gas and 0.2 liter per minute of air (N2 gas: Air = 99.4%: 0.06%) was utilized to produce plasma spraying on targeting sample with atmospheric pressure condition (see Table 3.4, fig. 3.9). The majority of N2 gas plays a very important role in the surface treatment of metallic surface because of their high-energy contents. The copper surface is placed facing toward to AP-plasma spray with 3mm gap, the operating time of AP-plasma treatment for test-section copper surface is set to 400 seconds (see fig. 3.10). Optimal AP-plasma treatment time is determined by the contact angle measurement with identical properties of coupon test over the range of AP-plasma treatment condition. And they are correlated with the change of surface characteristic (wettability, static contact angle). In addition, modified copper surface by atmospheric pressure plasma coating can be explained by chemical and mechanical changes of surface imposed by plasma particles. These surface analyses are usually performed by XPS and AFM. In this study XPS analysis was conducted to observe the surface modification after atmospheric pressure plasma treatment (fig. 5.9).

Table 3.4 The operation condition of atmospheric pressure plasma coating

Atmospheric Pressure Plasma operating condition	
Applied Voltage	12kV, 2.0kW(30kHz)
Gas combination	N2/Air = 300 lpm/ 0,2lpm (liter per min.)
Gas distance	2.5mm
Plasma area	30 mm X 550 mm
Treatment time	82 sec ~ 820 sec

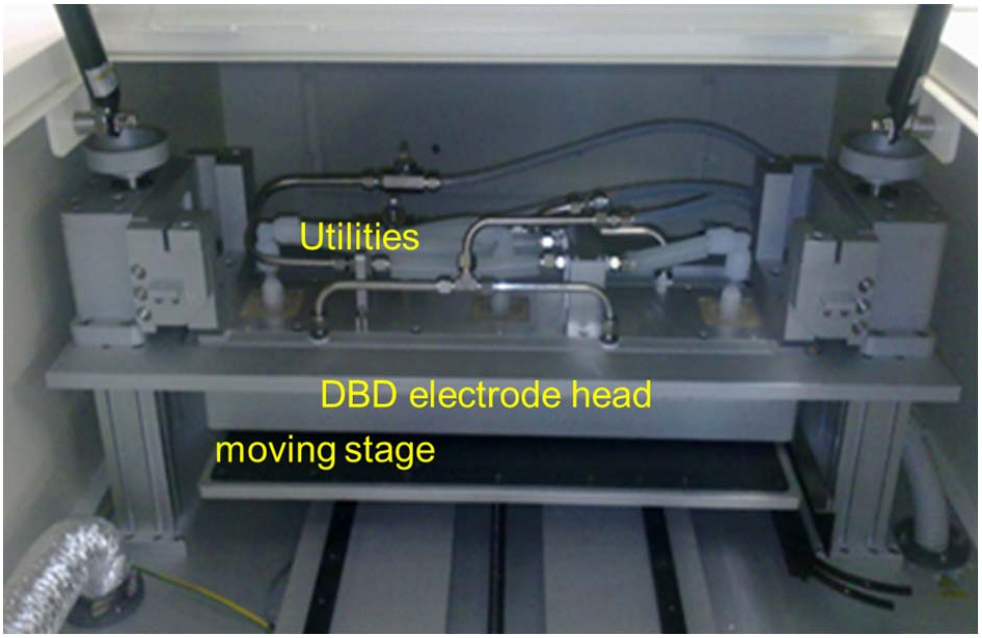


Figure 3.9 A picture of atmospheric pressure plasma coating device

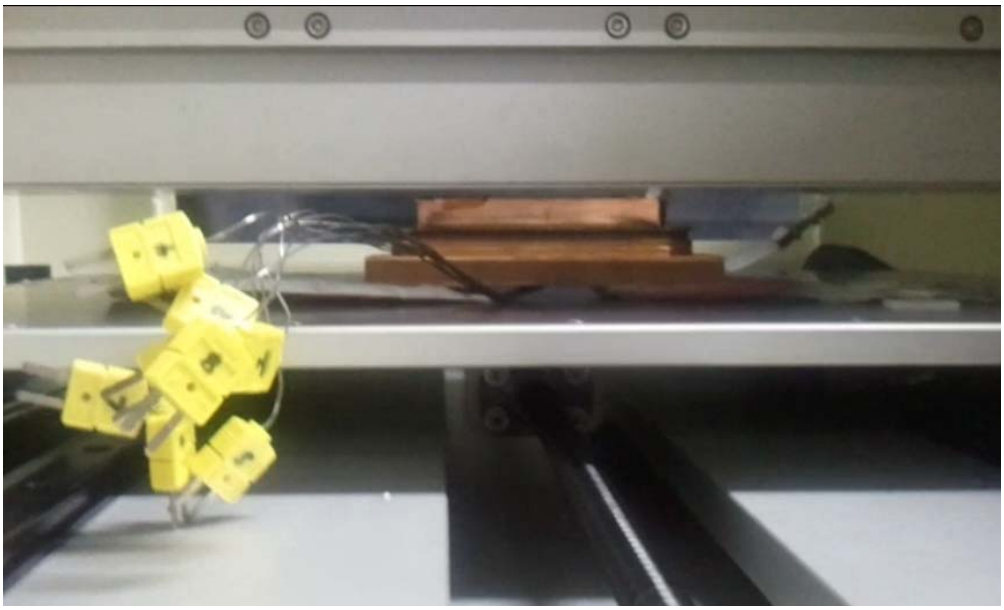


Figure 3.10 A picture of AP-plasma coating on copper test section from side view.

3.2.2 Contact angle measurement (surface wettability measurement)

A surface feature that may strongly affect Critical Heat Flux is the contact angle (Kim S.J., et al., 2007), which is related to the wettability of the surface. The contact angle also can be changed by the surface treatment through atmospheric pressure plasma coating on top of copper block. The results of the contact angle measurements and their significance are discussed in chapter 5.

The sessile drop technique was adopted to measure the static (not advancing or receding) contact angle. Pictures of the contact angle of a still droplet on the surface of interest are taken and the contact angle is estimated from such pictures. A state-of-the-art contact angle goniometer, Rame-hart model 500 was used for this purpose. The apparatus is shown in Fig. 3.11. Because the heater surfaces in our study are flat, static contact angle of liquid droplet was directly measured from the picture taken by Rame-Hart, model-500 with the help of the software PSM Image. The contact angle photo was imported in PSM Image and its left and right hand sides were read five times and averaged (see fig. 3.12). It is noted that determination of the contact angle value is somewhat subjective with this approach. The estimated uncertainty for these measurements is ±10 ˚. To obtain a reliable contact angle data, it is recommended to use a consistent volume of sessile drop during each test. The volume was kept below 5 μL for all tests. Also, the time duration of the measurement was held short, less than 30 seconds, to minimize the effect of droplet evaporation. The measurements were carried out at 22 C ˚ in air by depositing each droplet on the modified heater surface coupon from the respective atmospheric pressure

plasma coating condition.

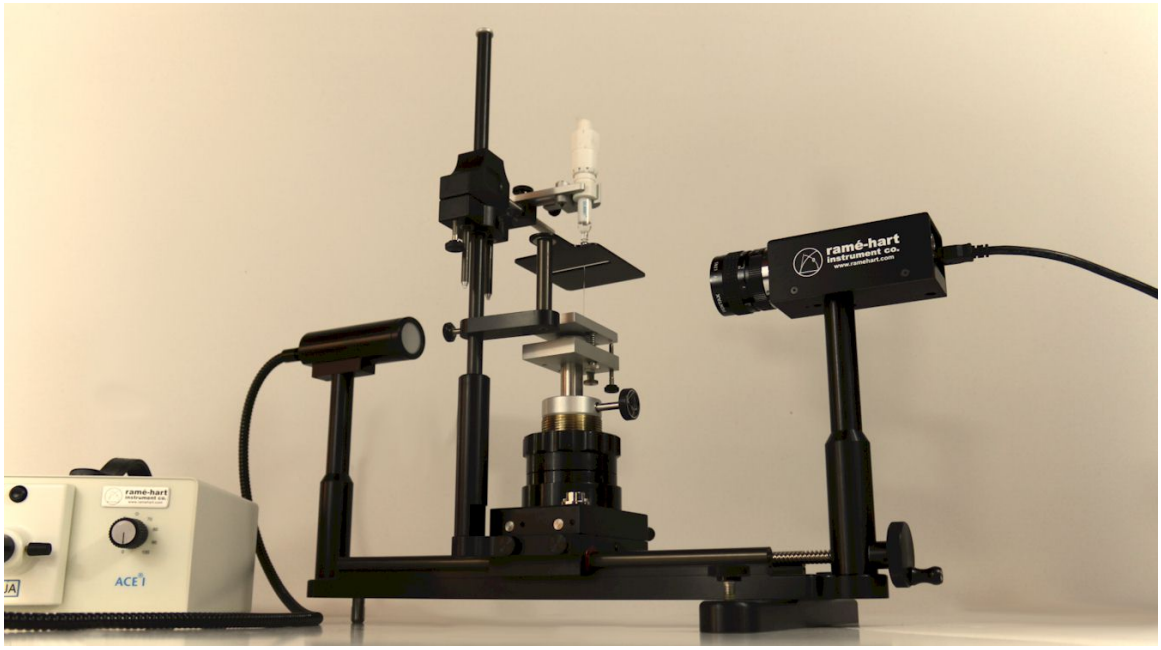


Figure 3.11 A picture of Rame-Hart model 500, Advanced goniometer/ tensiometer

The as-received copper coupon has contact angles around 80 ˚, while the copper coupons with surface treatment using atmospheric pressure plasma coating all have a significantly lower contact angle, ~15˚ ~ 30 ˚. Representative photos of the contact angles will be reported in the chapter 5. Recall that the maximum CHF enhancement was observed with the surface with AP-plasma treatment for around 800 sec., so there might be a correlation between contact angle reduction and CHF enhancement. This aspect is also represented in chapter 5.

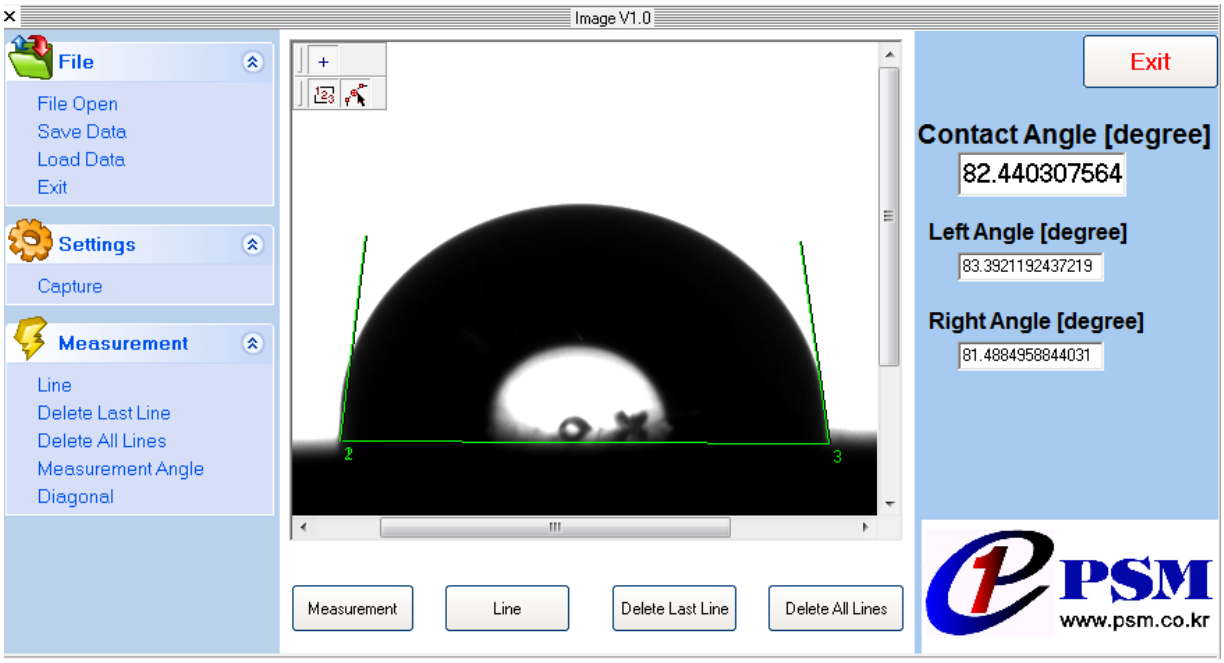


Figure 3.12 A picture of static contact angle measurement software. (www.psm.co.kr).

3.2.3 Coating layer thickness measurement (Dektak stylus profilometer)

Surface profilometry is a technique in which a diamond stylus, in contact with a sample, can measure minute physical surface variations as a function of position. The center operates a Sloan Dektak3 ST stylus surface profilometer for the measurement of surface topography. This instrument has the capability of measuring step height down to a few nm. The Dektak is controlled by a PC running Windows, making the system very easy to use (see fig. 3.13). The software offers several data processing functions as well as image capture and storage. The data can be easily converted to ASCII format and stored on a diskette for those requiring additional processing capabilities. Surface profilometry is commonly used to measure film thickness in thin

film deposition and processing. A diamond stylus is moved vertically in contact with a sample and then moved laterally across the sample for a specified distance and specified contact force. A profilometer can measure small surface variations in vertical stylus displacement as a function of position. The stylus profilometer at MRL can measure small vertical features ranging in height from 10 nm to 1 mm. Therefore for each sample, the stylus is moved from the edge of the sample to the other edge of the sample to find the profile and then average thickness.

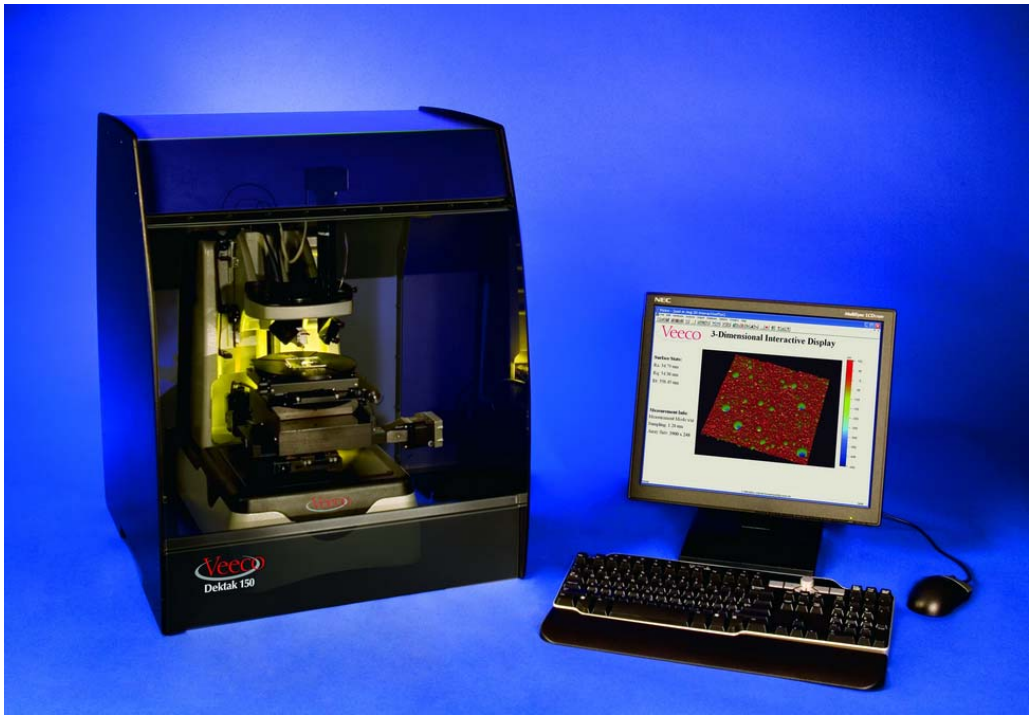


Figure 3.13 A picture of the model DEKTAK III- Stylus profilometer.

Nomenclature

English Symbols

$Cp_{,l}$	heat capacity of liquid at constant pressure
D_h	Hydraulic diameter
D	Width of heating block facing fluid
h_{fg}	Heat of vaporization (latent heat)
I	Current (A)
k	thermal conductivity (w/k)
L	Length of heating block facing fluid
L, L_h	Heated channel length
P	Pressure [Pa]
q''	Heat flux
Re	Prandtl number $\left(\mathrm{Pr} = \frac{\mu_f c_{pf}}{k_f}\right)$
T_{sat}	Satration Temperature (K)
V	Voltage (V)

Greek Symbols

β, θ	Static Contact angle at atmospheric pressure condition [°]
ρ_v	Density of vapor
ρ_l	Density of liquid
σ	Surface tension
ΔT	Temperature difference in different location
Δx	distance between the thermocouples
ω	the statistical uncertainty

Acronyms

ACRC	Air Conditioning and Refrigeration Center
AP-	Atmospheric Pressure-(Plasma)
CHF	Critical heat flux
DBD	Dielectric Barrier Discharge
MRL	Material Research Laboratory at UIUC

References

Chen, Peipei, 2007, “An experimental investigation of critical heat flux performance of hypervaporton in subcooled boiling” PhD Dissertation thesis, UIUC

Zou, Ling, 2011, “Experimental study of sub-cooled flow boiling on heating surfaces with different thermal conductivities” PhD Dissertation thesis, UIUC

Wu, Wen, 2007, “Combined modeling and experimental validation of boiling curve and critical heat flux” PhD Dissertation thesis, UIUC

Kim, Seung-Jun, 2011 “An Experimental study of Flow Boiling Critical Heat Flux Performance with Surface wettability concept” Proc. American Nuclear Society National Conference, Hollywood FL, June 26-30

Holman, J. P., 2001, "Experimental Methods for Engineers", 7th ed., McGraw-Hill, New York

ANSYS FLUENT, http://www.ansys.com/

NIST National Institute of Standards and Technology, http://www.nist.gov/index.html

PSM, Plasam System & Material, www.psm.co.k

4.Experimental Result

Chapter 4 reports the experimental results for the critical heat flux (CHF) measurement and its parametric trend study under the flow boiling condition with various macroscopic operating parameters (sub-cooled inlet temperature, mass flux, and system pressure) effects. In addition, the fluid-to-fluid (in this study, R134a-to-water) scaling method is presented in this chapter. Equivalent water CHF data converted from R-134a CHF value by using fluid-to-fluid scaling method are compared to the CHF look-up table.

4.1 Critical heat flux (CHF) Measurement and Parametric Trend Study

In order to investigate the flow boiling heat transfer with critical heat flux measurement, sub-cooled flow boiling CHF experiments were performed with an R-134a as a working fluid. Individual boiling curves and CHF point under various operating condition were obtained in this study. In addition, bubble dynamics under flow boiling conditions are well captured with reasonable resolution using a high-speed video camera. Fig. 4 indicates the shape of bubbles formed on the heated surface as heat flux increases. An exact understanding of parametric trends of CHF is very important to develop a reliable CHF prediction model. Although there has been significant research on parametric trends of CHF (Coller and Thome, 1994, Hewitt et al., 1982, Moon et al., 1996), some aspects are still not answered completely and surface characteristic effects on CHF need further investigation. Previous researchers have not adequately addressed, especially, parametric trends of CHF under the Low Pressure Low Flow (LPLF) condition. In

this study, operating system pressure applying to CHF test is manly low pressure condition where reduced pressure (P/P_{cr}) is below than 0.2, the range of mass flux for CHF test is also arranged below than 300 kg/m^2-s. These pressure and mass flux conditions meet the requirements of low pressure and low flow CHF test. Therefore, effect of system pressure, mass flux, and sub-cooled inlet enthalpy on CHF under low-pressure, low-flow condition was investigated in following sections.

In flow boiling experiment, sudden temperature rising at the heating surface or significant heat flux drop is a good indicator for the onset of CHF. Figure 4.2 shows present experiment also follows sudden temperature rising and wall heat flux drop at the near CHF point. It takes about 2~3 hours to produce a boiling curve of each individual CHF test with data reduction process. Figure 4.3 shows the boiling curves in the present CHF measurement and visualization experiment. The temperatures measured from the heated wall represent the typical relation of heat flux vs. wall temperature between a single-phase region and two-phase region. As the mass flux increases, the wall temperature decreases at same heat flux in the single-phase region, but there is no change in the two-phase region. Visualization from side view was performed mainly in the two-phase region, from a low heat flux (10~15% of CHF) of the ONB (Onset of Nucleating Boiling) with discrete bubbles, to a near CHF with large vapor clots, by a violent coalescing behavior of those bubbles.

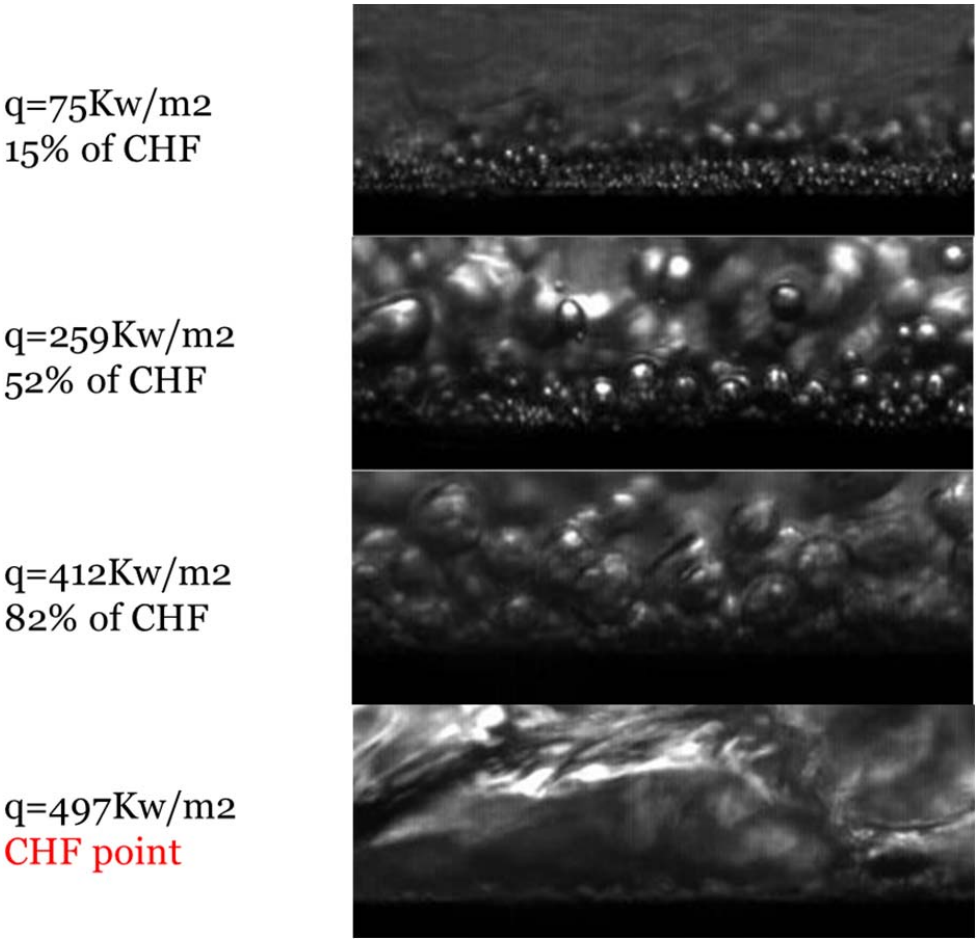


Figure 4.1 The visualization of bubble behavior from isolate bubble regime (nuclear boiling) to coalesced bubble regime (near CHF).

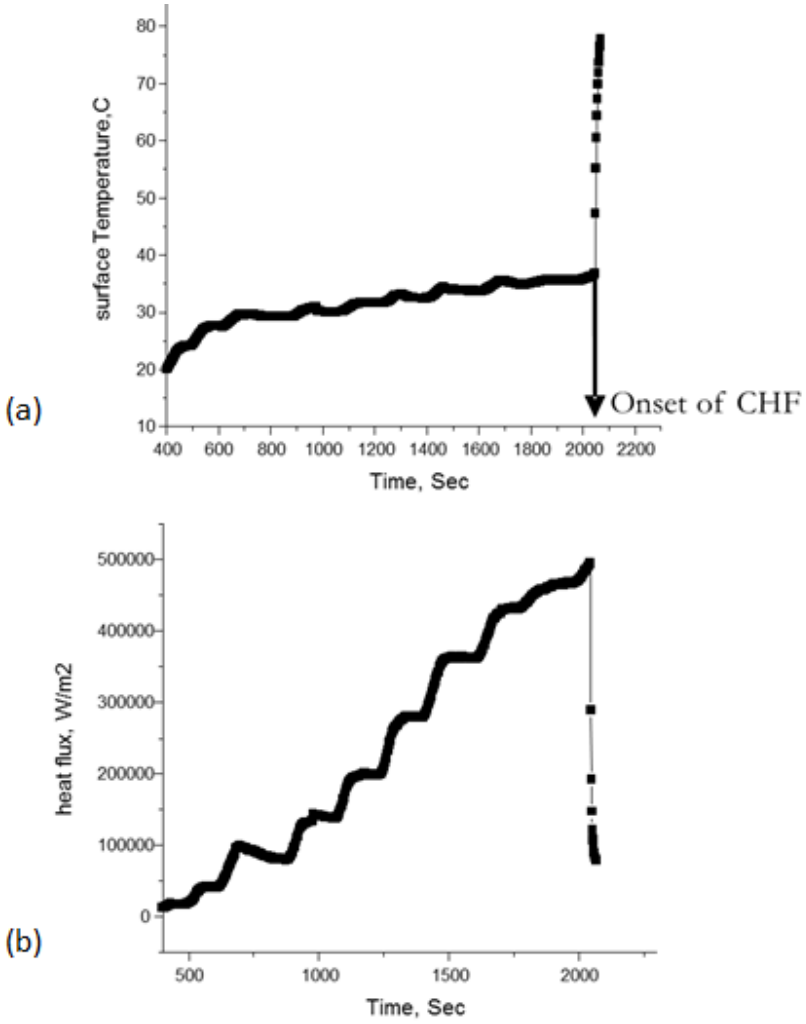


Figure 4.2 A sudden temperature rise (a) and sudden heat flux drop (b) at the critical heat flux point.

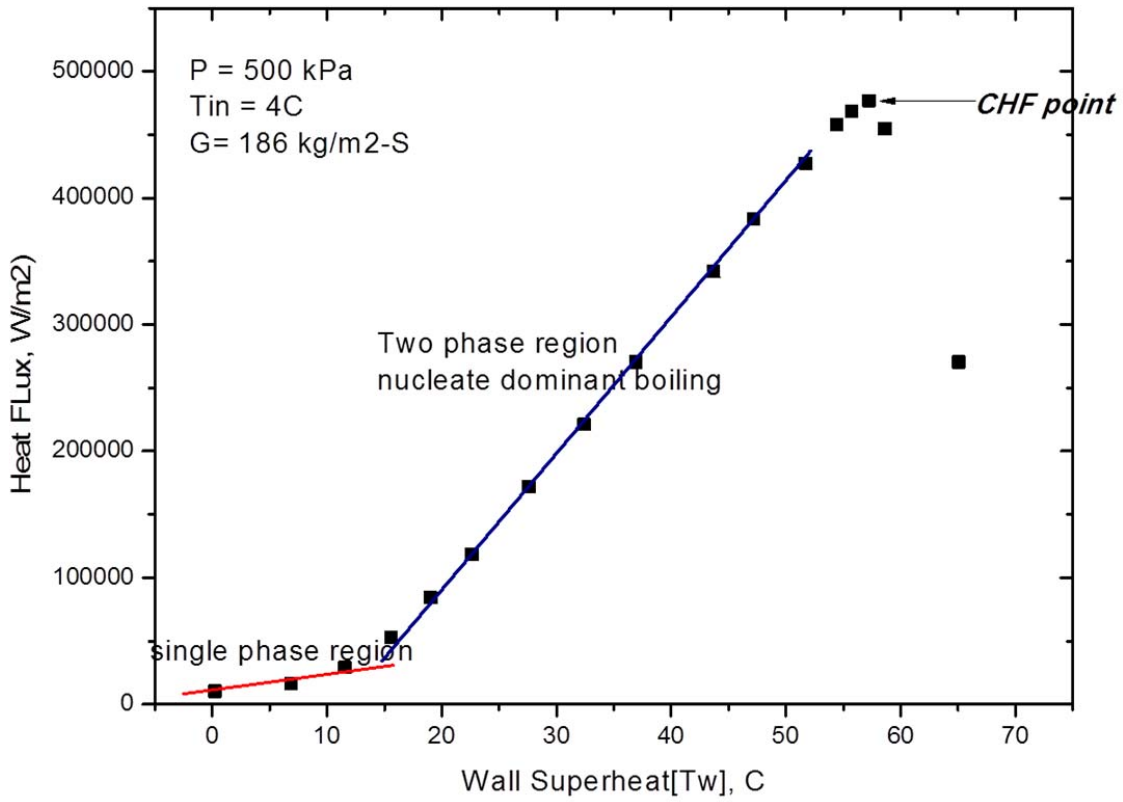


Figure 4.3 A general boiling curve with highlighted single-phase region, two-phase region, CHF point under system pressure of 5 bar, inlet sub-cooled temperature of 4C˚, and mass flux of 186 kg/m2-s.

4.1.1 Effect of sub-cooling inlet temperature on CHF

For CHF of forced convection boiling in vertical and horizontal uniformly heated tubes, it is well known (Collier, J.G., 1994, Lee, D.H., 1977) that plots of CHF against sub-cooled inlet temperature for fixed mass flux and pressure often indicate the linear relationship such as is shown in figure 4.4, and it can be written as follows:

$$q_{CHF,sub-cooled} = q_{CHF,saturation}\left(1 + K\frac{\Delta h_i}{h_{fg}}\right) \quad (4\text{-}1)$$

Where, K is a dimensionless parameter independent ofΔh_i,

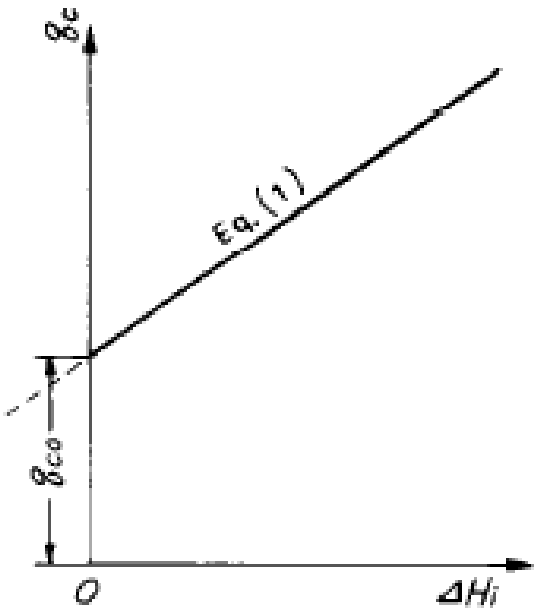
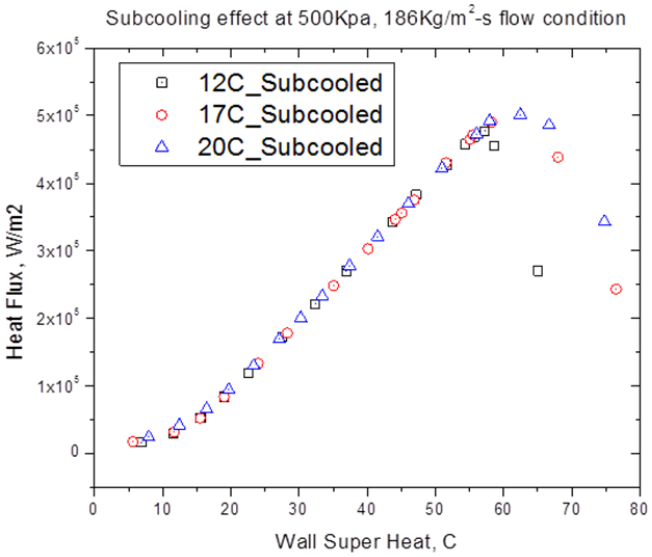


Figure 4.4 The linear relationships between CHF (q_c) and Δh_i for fixed mass flux, pressure (katto, Y., 1979).

The effect of inlet sub-cooled temperature on CHF is shown in figure 4.5. With system pressure and mass flux fixed, different sub-cooling temperature are implemented to observe the effect of inlet cub-cooled temperature on CHF. Three sub-cooled inlet temperature selected; 12 C°, 17 C°, and 20 C°, respectively, with a fixed pressure of 500 kPa and a fixed mass flux of 186 kg/m^2-s.

Thought the effect is not large, it is clear that the CHF increase with the increase in inlet sub-cooled temperature. Most of the previous investigators have reported that the inlet sub-cooling effect on CHF is negligible for low pressure (Mishima et al., 1985; Chang et al., 1991; Bergles, 1977), present experiments result show that the inlet sub-cooling effect certainly exists in low pressure low flow condition. The quantitative CHF increase with inlet sub-cooling level is shown in figure 4.6. With higher sub-cooled fluid entering the heating zone, more effective boiling heat transfer takes place at the heating surface. This effect is already well reported by previous researchers as well as supported by the present experimental data. Therefore, it can be concluded that the sub-cooling inlet temperature is a key parameter for the determination of CHF in sub-cooled flow boiling cases.



(a)

Figure 4.5 Boiling curves with different sub-cooled inlet temperatures at P=500Kpa, G=186 kg/m^2-s.

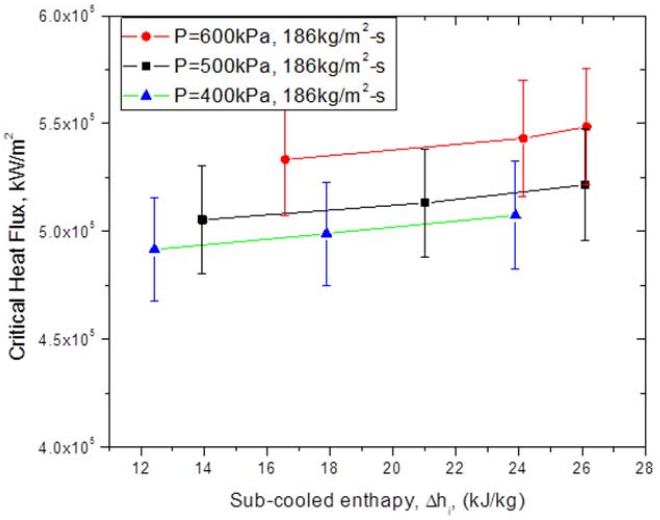


Figure 4.6 The effect of sub-cooling level on critical heat flux at fixed G=186 kg/m^2-s.

4.1.2 Effect of mass flux on CHF

In General, it is reported that the CHF increases with the increase of mass flux for fixed system pressure, and sub-cooled temperature, however, the rate of increase decreases with increasing mass flux (see fig. 4.7). As shown in figure 4.7, the mass flux effect on CHF under the low flow condition follows a positive trend with sharp gradient. Beyond 1500 kg/m^2-s of mass flux condition, the mass flux effect on CHF is negligible, whereas the CHF are more likely predominantly dependent of the equilibrium quality which is related to inlet sub-cooled temperature in fixed inlet condition.

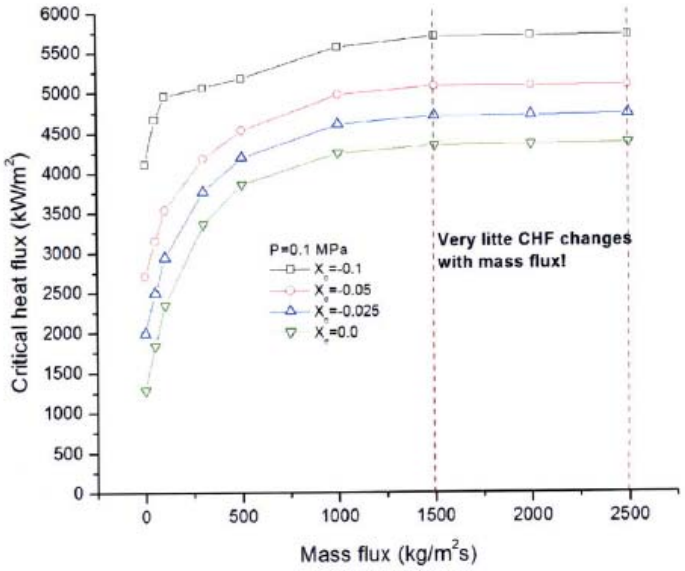


Figure 4.7 CHF variation according to the mass flux; extracted from 1995 CHF look-up table (Kim et al., 2009).

In this study, CHF was measured for different mass flux conditions with fixed system pressure

and inlet sub-cooling level. The mass flux effect on CHF is indicated in figure 4.8. Three mass fluxes were selected: 126.6 kg/m^2-s, 190.4 kg/m^2-s, and 253.3 kg/m^2-s, respectively with a fixed pressure of 500 kPa, and sub-cooling level of 17 C˚. The effect of mass flux shows that increases in mass flux increase the CHF value. The quantitative CHF increase with mass flux found in current experimental data is shown in figure 4.9. At the boiling surface, i.e. interface between liquid phase and vapor phase, a high mass flux is important to detach bubbles from the heating surface, and to avoid the coalescence of bubbles, which can trigger film boiling, or onset of critical heat flux. Therefore, it is also reasonably accepted that the mass flux is one of key parameter that determines CHF.

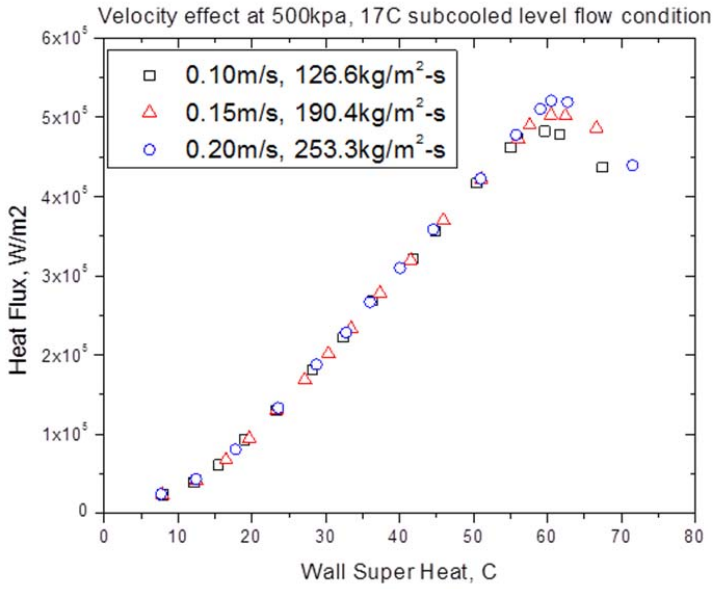


Figure 4.8 Boiling curves with different mass fluxes at P=500Kpa, sub-cooled inlet temperature = 17C˚

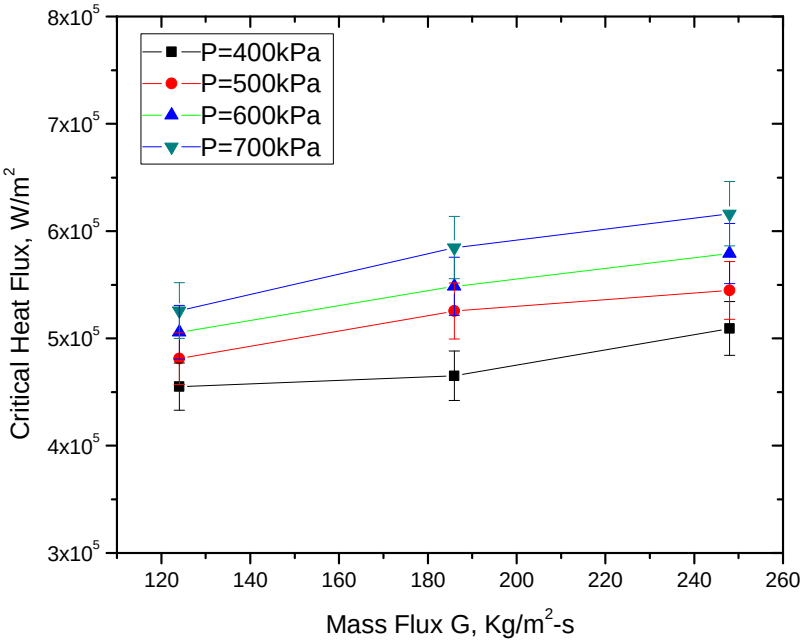


Figure 4.9 The effect of mass flux on critical heat flux with fixed pressure sub-cooling enthalpy.

4.1.3 Effect of system pressure on CHF

It is generally known that CHF increases with the increase of pressure, goes through a maximum where the reduced pressure is around 0.2, then decreases with pressure (Collier and Thome, 1994; Bergles, 1977). As pressure increases, surface tension, latent heat of vaporization and steam-to-water specific volume ratio decrease. In particular, the specific volume ratio decreases sharply from about 1600 at 1 bar to about 55 at 50 bar, then it decreases slowly with increasing pressure. Figure 4.10 indicated the CHF variation according to reduced pressure, P/P_{cr} : a non-dimensionless parameter defined as its actual pressure (P) divided by its critical

pressure(P_{cr}), extracted from the CHF look-up table for different mass flux (300 Kg/m^2-s, 500 kg/m^2-s, 750 kg/m^2-s) and fixed exit quality (X_{exit} =-0.05) conditions. As seen from figure 4.10, CHF increase with increase of reduced pressure till 0.2, and then CHF decrease with increase of reduced pressure.

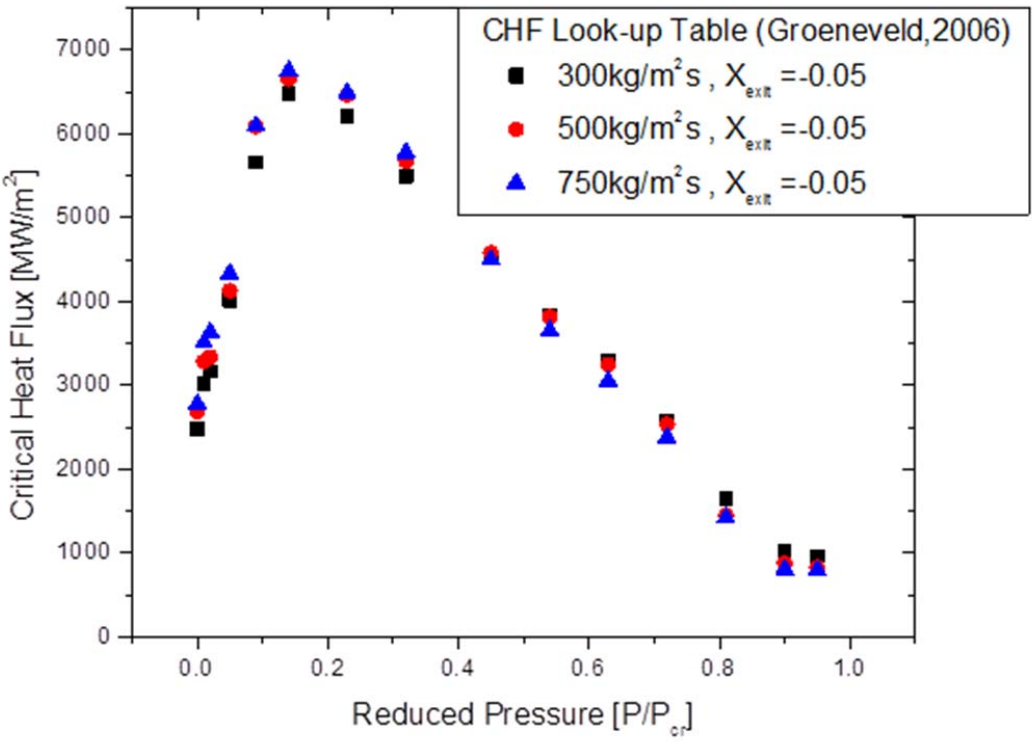


Figure 4.10 The CHF variation according to system pressure; extracted from 2006 CHF look-up table.

The effect of pressure observed in the present tests is illustrated in Fig. 4.11. In the figure, the CHF increases with the increase in the pressure range of 4 ~ 8 bar (below than 0.2

reduced pressure for R-134a). Kim, H.C., (2000) also reported that at low-pressure conditions CHF is proportional to the system pressure in linear fashion. A trend of CHF with system pressure in this present study also show good agreement with Kim's findings for system pressures of 400 kPa, 500 kPa, 600kPa, 700kPa, and 800 kPa, respectively, with different mass flux.

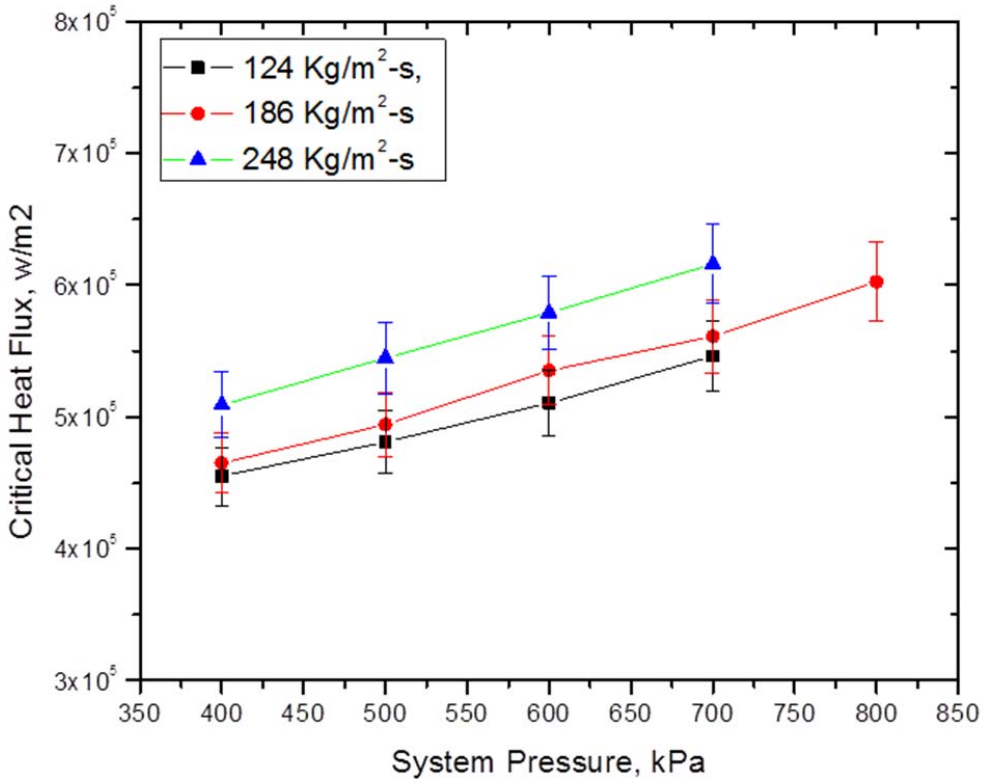


Figure 4.11 Effect of system pressure on critical heat flux.

4.1.4 An empirical CHF prediction correlation based on R-134a flow boiling CHF experimental data

In this section, an empirical CHF prediction model is proposed with key experimental parameters (system pressure, mass flux, and sub-cooled inlet enthalpy) for the flow boiling condition with R-134a as a working fluid. In general, there have been three approaches for CHF prediction; empirical correlation, analytical correlation based on physical model, and look-up table method. We first developed an empirical correlation of CHF prediction for limited experimental conditions in this chapter. The theoretical CHF prediction correlation development is presented in chapter 5. The importance of the critical heat flux phenomena has led to the development of a very large number of CHF correlations with various ranges of experimental condition. It is beyond the scope of this study to present a comprehensive description of these many correlations (refer to chapter 2.4). However, There are more than hundreds empirical critical heat flux prediction correlation for certain experimental conditions with a combination of key experimentally measured parameters; pressure, mass flux, sub-cooling, and flow channel and heating zone geometry. Our experimental apparatus was originally designed to visualize the bubble inception, growth, and departure from the heating surface as well as CHF measurement. We examined 36 critical heat flux data point from various experimental conditions. Experimental parameter values are tabulated in table 4.1.

Table 4.1 The measured CHF data point in various experimental conditions.

# of sample	CHF (Kw/m2)	Pressure (kPa)	Mass Flux (kg/m2-s)	sub-cooling enthalpy (Hi-Hf, KJ/Kg)
1	462.951	400	124	14.787
2	509.282	400	248	14.535
3	498.970	400	248	13.951
4	501.252	400	248	12.756
5	491.620	400	248	9.425
6	495.425	500	124	22.935
7	525.567	500	186	23.205
8	544.685	500	248	22.017
9	513.183	500	186	21.019
10	505.413	500	186	13.936
11	510.625	600	124	30.670
12	548.506	600	186	30.508
13	579.069	600	248	28.349
14	535.199	600	186	28.132
15	533.354	600	186	22.022
16	546.207	700	124	35.866
17	584.638	700	186	36.488
18	616.157	700	248	35.880
19	583.294	700	186	35.893
20	561.116	700	186	29.139
21	617.047	800	186	43.696
22	602.688	800	186	38.682
23	454.938	400	124	17.004
24	465.120	400	186	15.531
25	481.098	500	124	26.307
26	501.414	500	186	25.012
27	491.944	500	186	21.586
28	478.443	500	186	16.499
29	494.291	500	186	24.378
30	519.917	500	248	24.567
31	505.704	600	124	32.381
32	530.666	600	186	30.901
33	544.329	600	248	28.539
34	525.858	700	124	38.838
35	560.809	700	186	36.312
36	587.179	700	248	37.244

To develop the empirical CHF prediction correlation with controllable experimental key parameters (pressure, mass flux, and sub-cooled enthalpy), 36 CHF data point were utilized to evaluate the sensitivity of individual parameter effect on CHF prediction model. With a help of Matlab, data regression was conducted with numerical optimization tool, and critical hear flux correlation was induced from data regression process; moreover, Origin 8.1 software was utilized to confirm the data regression process and correlation generation. Both of numerical tool provide almost similar empirical correlation with negligible error band. The proposed empirical correlation is only a function of system pressure, mass flux, and sub-cooling enthalpy, which are the main controllable experimental parameters in current study.

In general, the CHF is a function of six independent variables, i.e., system pressure (P), heated length (L_h), tube diameter (D_i), flow channel width (w), mass flux (G), and inlet sub-cooling enthalpy (Δh_i). This relationship represents the fixed inlet conditions concept, and inlet temperature (T_{in}) or inlet quality (x_i) can be used instead of inlet sub-cooling enthalpy. In the fixed exit condition concept, exit quality (x_e) is used instead of inlet sub-cooling enthalpy. Exit quality and inlet sub-cooling enthalpy are related to each other via the heat balance equation. The quality is the thermodynamic equilibrium quality at the test section outlet, which was calculated by assuming the following steady-state heat balance equation:

$$x_e = \frac{h-h_f}{h_{fg}} = \frac{4\pi D_i L_h q}{(4w^2-\pi D_i^2)Gh_{fg}} - \frac{\Delta h_i}{h_{fg}} \quad (4\text{-}2)$$

Under the present fixed conditions of heated length (L_h), tube diameter (D_i), flow

channel width (w) and uniform heating condition of the heater, finally, CHF is the following type of function:

$$q_{CHF} = f(P, G, x_e) \ , \ q_{CHF} = f(P, G, \Delta h_i) \tag{4-3}$$

The empirical correlation of CHF prediction under current experimental condition is listed

$$q_{CHF} = 274.31 + 0.284P + 0.416G + 0.541\Delta h_i \tag{4-4}$$

$$q_{CHF} = 256.95 + 0.338P + 0.436G + 220x_e \tag{4-5}$$

This correlation is only applicable for current experimental conditions. Due to limitation of experiment settings, diameter effect of critical heat flux was not considered in the above empirical correlations. The detail measurement information and correlation prediction are summarized in appendix D. Figure 4.12 shows that the comparison between experimentally measured critical heat flux points and prediction of the empirical CHF correlation (eq. 4-4 and 4-5) based on inlet sub-cooled enthalpy and exit quality, respectively. The average error and RMS errors of the predictions are 0.31%, 0.27% and 5.1%, 7.2%, respectively.

The advantages of the proposed empirical correlation are listed as follows:

- Unique empirical CHF correlation which is intended to be utilized for flow boiling heat transfer in rectangular channel

- Unlike general empirical models, the current empirical correlation is designed to predict

the CHF with low-flow and low-pressure conditions (LFLP), which show poor prediction accuracy with general empirical models (Chang et al., 2005).

- Compared to other CHF prediction correlations, the proposed empirical correlation is simple to utilize with three variables (for both fixed inlet condition and fixed outlet condition). With key parameters measurements, the CHF for the current experimental range is predicted with simple calculation; no additional iterative calculation is required.

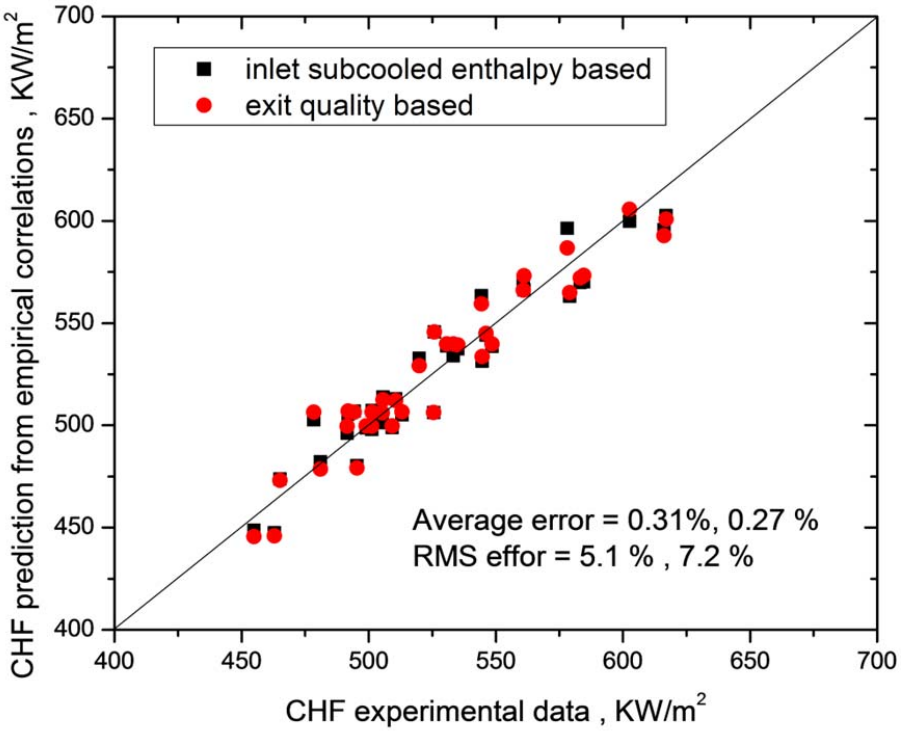


Figure 4.12 Comparison of predicted CHF values and measured CHF data points

4.2 R134a-water Scaling Method and Comparison Work

The critical heat flux (CHF) has been considered to be one of the most important parameters in designing and operating the heat transfer enhancement equipment. However, CHF experiments using water as working fluid suffer from high temperatures and high pressures and encounter certain difficulties, for example, high expenditure for materials and more complex experimental platform construction. To avoid these difficulties, Barnett was the first investigator to propose fluid-to-fluid CHF modeling using low latent heat of working fluid such as Freon R-12, R-35 and developed scaling laws for application (Barnett et al., 1963, 1964, 1965). Recently, alternative refrigerant of R-134a was also considered to be applicable as modeling fluids. The modeling scaling factors is be determined by the classical dimensional analysis or similarity theories. Then, the investigation of CHF characteristics in R134a is carried out with various experimental conditions in this research. Finally, the results derived from modeling experiments of CHF in R134a can be extended to apply to prototype fluid (i.e. water) according to fluid-to-fluid scaling factors. The purpose of this conversion to water and R134a is to reduce the expenditure and difficulties of prototype experiments under high temperature and pressure. Actually, the CHF phenomena is too complicated to be described in a mathematical equation accurately, so the most effective way to study the essence of CHF is to use dimensional analysis method to find out the relationships among all the main variables. A typical example is the compensated distortion model derived by Ahmad and Katto (Ahmad, et al., 1973; Katto et al., 1978).

4.2.1 Fluid-to-fluid scaling method of CHF

Ahmad's compensated distortion model and the Katto model are widely used and are accurate enough in engineering applications (Ahmad, et al., 1973; Katto et al., 1978). So here Katto model (Fluid-to-Fluid Scaling Method) is chosen as calculation models. Katto introduced five dimensionless groups to fluid-to-fluid CHF modeling method based on dimensional analysis and the similarity criteria formula as follows:

$$\frac{q_c}{G\lambda} = f\left(\psi_{CHF}, \frac{\Delta H}{\lambda}, \frac{\rho_l}{\rho_g}, L/D\right) \tag{4-6}$$

$$\psi_{CHF,Katto} = \frac{G\sqrt{D}}{\sqrt{\sigma\rho_l}} \tag{4-7}$$

$$\psi_{CHF,Ahmad} = \left[\frac{\mathrm{GD}}{\mu_l} \cdot \left(\frac{\gamma^{0.5}\mu_l}{D{\rho_l}^{0.5}}\right)^{\frac{2}{3}} \cdot \left(\frac{\mu_l}{\mu_g}\right)^{\frac{1}{8}}\right] \tag{4-8}$$

To develop fluid-to-fluid CHF model in prototype fluid (water) using modeling fluid (R-134a) with Katto method, the following equations should be satisfied at the same time.

$$\left(\frac{L}{D}\right)_P = \left(\frac{L}{D}\right)_M \quad \text{: Geometric similarity} \tag{4-9}$$

$$\left(\frac{\Delta H}{\lambda}\right)_P = \left(\frac{\Delta H}{\lambda}\right)_M \quad \text{: Thermodynamic similarity} \tag{4-10}$$

$$\left(\frac{\rho_l}{\rho_g}\right)_P = \left(\frac{\rho_l}{\rho_g}\right)_M \quad \text{: Hydrodynamic similarity} \tag{4-11}$$

$$\left(\frac{G\sqrt{D}}{\sqrt{\sigma\rho_l}}\right)_P = \left(\frac{G\sqrt{D}}{\sqrt{\sigma\rho_l}}\right)_M \quad (4\text{-}12)$$

Three equations (4-9, 4-10, and 4-10) of the four criteria equations are identical except the fourth one (4-11). That is to say, there is only one condition different for the two modeling models. The following items can be used to calculate the four modeling scaling factors: F_L, F_P, F_H, and F_G.

(a) Because of the uncertain influence of flow channel on fluid modeling of CHF, geometry size of model is usually the same as prototype. Thus the equation $\left(\frac{L}{D}\right)_P = \left(\frac{L}{D}\right)_M$ will be satisfied itself, and size modeling scaling factor F_L=1.

(b) Calculate the density ratio of the liquid to the vapor. Find out the pressure of prototype fluid and the pressure of modeling fluid at the same density ratio point. Then pressure modeling scaling factor F_P can be obtained by:

$$F_P = \frac{P_P}{P_M} \quad (4\text{-}13)$$

(c) Since $\left(\frac{\Delta H_P}{\lambda}\right)_P = \left(\frac{\Delta H_P}{\lambda}\right)_M$, latent modeling scaling factor F_H can be determined by

$$F_H = \frac{\Delta H_p}{\Delta H_p} = \frac{\lambda_P}{\lambda_M} \quad (4\text{-}14)$$

(d) Mass flux modeling scaling factor F_G can be calculated as follows:

$$\text{Katto}: \ F_G = \frac{\left(\sqrt{\frac{\sigma\rho_l}{D}}\right)_P}{\left(\sqrt{\frac{\sigma\rho_l}{D}}\right)_P} \tag{4-15}$$

If latent modeling scaling factor F_H and mass flux modeling scaling factor F_G were known, then CHF modeling scaling factor

$$F_{CHF} = \frac{(q_{CHF})_P}{(q_{CHF})_M} = \frac{G_P}{G_M} \cdot \frac{\lambda_P}{\lambda_M} = F_G \cdot F_H \tag{4-16}$$

All the four modeling scaling factors of R134a-water F_L, F_P, F_H and F_G were calculated based on the thermo physical properties data published in ASHRAE for R134a and reference for water(ASHRAE, 2001; Yan et al., 1995). According to references (ASHRAE, 2001), the data which were near the triple point and the critical point was excluded. The pressure range selected in R134a was 0.15-3.59Mpa, water-equivalent pressure range 1-20Mpa, and the density ratio was 172.45-2.88. The corresponding relationship between the R-134a-water pressures and density ratios is shown in Fig.4.13. Table 4.2 shows the selected 5 pairs of R134a/water pressures and density ratios' data which covers all current test pressure range. From this data, it has been determined that difficulty for performing CHF experiments would be drastically reduced by 70%~80% using R-134a as modeling fluid in term of pressure conditions.

Table 4.2 The R-134a and water density ratios data along with pressure

R-134a				Water			
Pressure[Bar]	ρ_l , kg/m^3	ρ_g, kg/m^3	ρ_l/ρ_g	**Pressure[Bar]**	ρ_l , kg/m^3	ρ_g , kg/m^3	ρ_l/ρ_g
4	1264.7	19.53	64.76	**26**	832.37	13.04	64.03
5	1240.8	24.33	51.03	**32**	816.92	16.04	51.05
6	1219.5	29.16	41.83	**38**	802.82	19.12	42.13
7	1200.2	34.05	35.25	**45**	787.61	22.61	34.70
8	1182.2	39.02	30.29	**50**	777.36	25.35	30.66

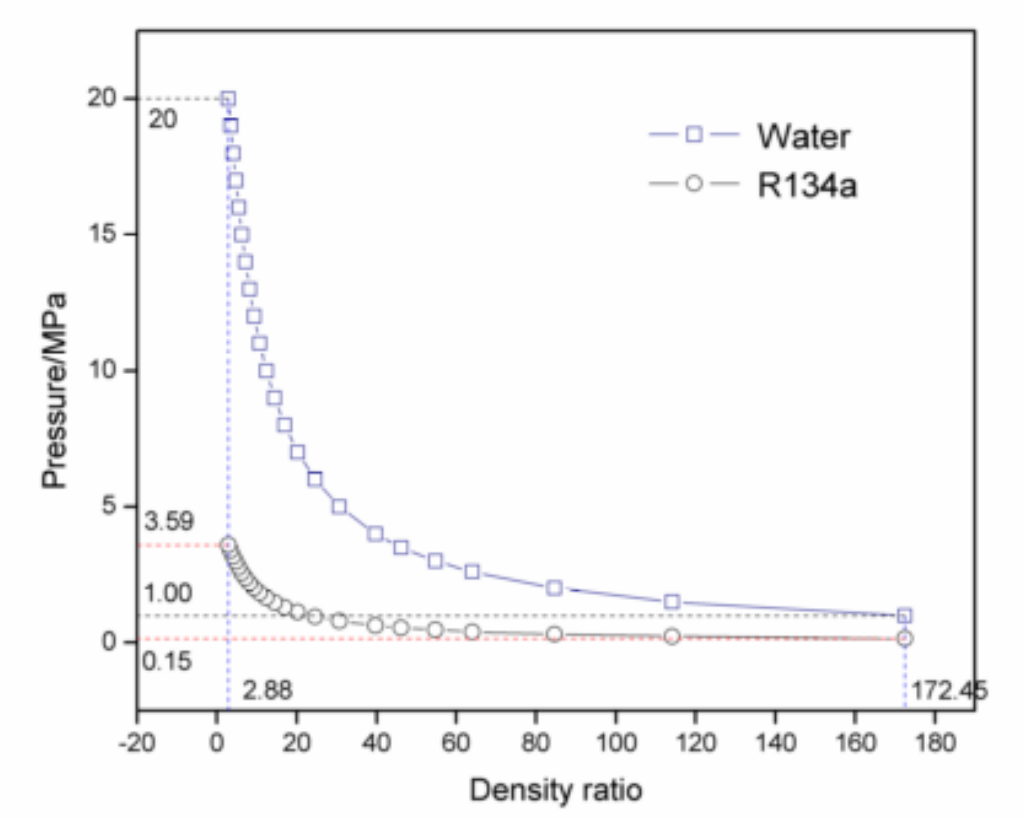


Figure 4.13 Corresponding relationships between density ratios of R-134a and that of water along with pressure (Chen, et al., 2010).

4.2.2 Comparison work between equivalent water CHF data and look-up table

The validity of the fluid-to-fluid modeling method was confirmed by comparing the CHF data converted from R134a flow boiling experimental data with existing CHF data in water provided from CHF look-up table (Groeneveld, et al., 2006). The selected condition ranges in R134a for comparison with CHF data in water are shown in Table 4.3. A sample of fluid-to-fluid converting process and comparison work is listed as follows (See Fig. 4.11).

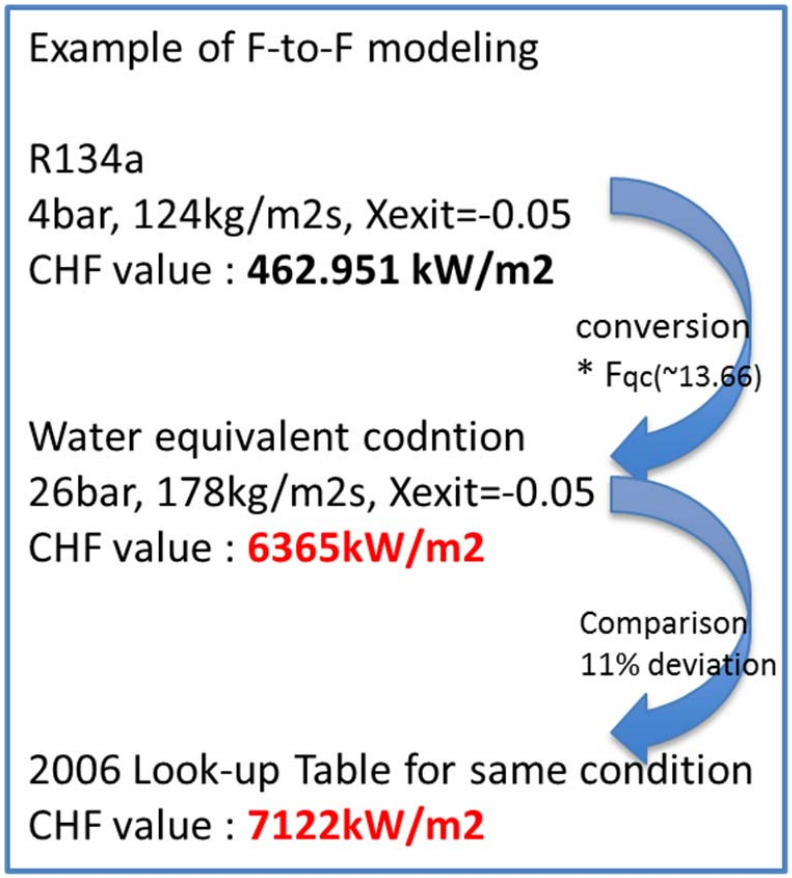


Figure 4.14 A schematic diagram of equivalent water CHF converting process and comparison with CHF look-up table.

Converting procedure form the R-134a CHF to Water-equivalent CHF

1. Select the one CHF with pressure, mass flux, exit quality (e.g. CHF=462.95 kW/m2 at 4bar, 124/m^2-s, x_{exit}=-0.05)

2. Determine the water equivalent condition using F_P, F_G, and assume geometry similarity is obtained (F_L=1) (see Table 4.4).

   Water equivalent pressure and mass flux condition become 26 bar (4 × F_p), 178 kg/m^2-s (124 kg/m^2-s * F_G), respectively.

3. Determine the water equivalent CHF value using F_{CHF} (e.g. $CHF_{water\ equivalent}$ = F_{CHF} × CHF_{R134a}= 13.75 × 462.951 = 6365 kW/m^2)

4. Find the existing water CHF data from the CHF-look-up table under the water equivalent condition (Pressure: 26 bar, Mass flux: 178 kg/m^2-s, x_{exit}: -0.05). CHF value is selected as 7122 kW/m^2 from look-up table.

5. Compare between the water equivalents CHF converted from R134a experimental test data using fluid-to-fluid method and the CHF look-up table result under identical water equivalent operating condition. ($CHF_{water\ equivalent}$ / $CHF_{Look\text{-}up\ table}$ = 1.118)

Table 4.3 A selected conditions in R134a and the corresponding conditions in water.

Test Matrix condition in R-134a and their water-equivalent conditions						
Pressure (bar)		Saturation Temp. C°		Mass Flux (R-134a), Kg/m^2-s		
				124	186	248
R-134a	Water	R-134a	Water	Mass Flux (Water), Kg/m^2-s		
4	**26**	8.93	226	**178.56**	**267.84**	**357.12**
5	**32**	15.73	237	**177.94**	**266.91**	**355.88**
6	**38**	21.57	247	**177.32**	**265.98**	**354.64**
7	**45**	26.71	257	**176.70**	**265.05**	**353.41**
8	**50**	31.33	264	**176.08**	**264.12**	**352.16**

Table 4.4 A summary of R134a-water fluid-to-fluid modeling scaling factor.

Summary of scaling factor (F_L, F_P, F_H, F_G, F_{CHF}) along with pressure						
No	R-134a, Pressure[Bar]	F_L	F_P	F_H	F_G	F_{CHF}
1	1.5	1	6.67	9.55	1.46	13.94
2	2.3	1	6.53	9.57	1.46	13.97
3	3.1	1	6.46	9.57	1.45	13.88
4	**4.0**	**1**	**6.50**	**9.55**	**1.44**	**13.75**
5	**5.0**	**1**	**6.40**	**9.56**	**1.44**	**13.77**
6	**6.0**	**1**	**6.33**	**9.55**	**1.43**	**13.66**
7	**7.0**	**1**	**6.43**	**9.53**	**1.43**	**13.36**
8	**8.0**	**1**	**6.25**	**9.52**	**1.42**	**13.52**
9	9.6	1	6.19	9.50	1.41	13.40
10	11.3	1	6.15	9.48	1.41	13.37

Table 4.5 Comparison between water-equivalent CHF value and 2006 CHF look-up table

water equivalent CHF value converted from R134a					(2006 CHF look-up table)				
P, bar	G, Kg/m2-s	exit quality	CHF, R134a, w/m2	water-eq. CHF, KW/m2	P, bar	G, Kg/m2-s	exit quality	wate CHF, w/m2	ratio
4	124	-0.0012	462.951	6366	26	178.56	0	**7122**	1.12
4	248	-0.0091	509.282	7003	26	357.88	0	**6222**	0.89
5	124	-0.0075	495.425	6812	32	177.94	0	**6951**	1.02
5	186	-0.0102	513.183	7056	32	266.91	0	**6620**	0.94
5	248	-0.0107	544.685	7489	32	355.88	0	**6384**	0.85
6	124	-0.0071	510.625	7021	38	177.32	0	**5952**	0.85
6	186	-0.0009	548.506	7542	38	265.98	0	**6374**	0.85
6	248	-0.0058	579.069	7962	38	354.64	0	**6577**	0.83
7	124	-0.0111	546.207	7510	45	176.7	0	**5703**	0.76
7	186	-0.0107	584.638	8039	45	265.05	0	**6510**	0.81
7	248	-0.0128	616.157	8472	45	353.4	0	**6655**	0.79
8	186	-0.0095	602.688	8287	50	264.12	0	**6107**	0.74

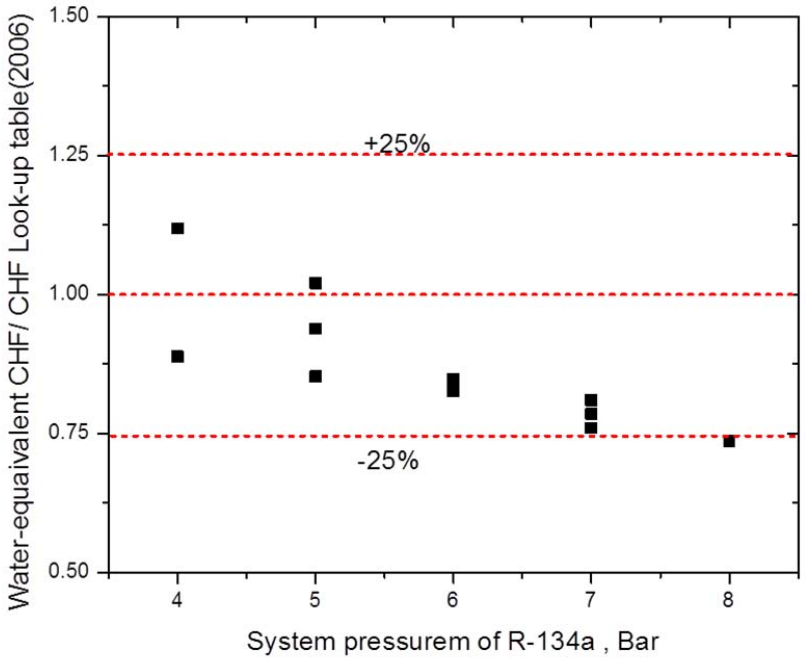


Figure 4.15 Ratios of the water-equivalent CHF data converted from the CHF data in R-134a to the CHF data from Look-up table with identical operating condition along with pressure

The table 4.5 is a summary of operating condition of R-134a flow boiling, converted operating condition of water flow boiling, water-equivalent CHF data, and look up table result. The validity of the fluid-to-fluid modeling method was performed. Comparison between water equivalent CHF and 2006 CHF look-up table was also conducted along pressures range of 4, 5, 6, 7, and 8 bar. A good agreement is achieved between the water equivalent CHF data converted from R-134a CHF data by using fluid-to-fluid modeling and the existing water CHF data from 2006 CHF look-up table under identical operating conditions, with an error of 25% as indicated in Fig. 4.15.

Nomenclature

English Symbols

D, D_i	Tube diameter
F_G	Scaling factor of mass flux
$F_{\Delta h}$	Scaling factor of sub-cooled enthalpy
F_P	Scaling factor of system pressure
F_L	Scaling factor of heating channel geometry
F_Q	Scaling factor of critical heat flux
G	Mass flux [Kg/m^2]
h_{fg}	Heat of vaporization (latent heat)
K	Non-dimensionless parameter in Katto correlation
L, L_h	Heated channel length
P	Pressure [Pa]
P_{cr}	Critical pressure
$q_{CHF,}$ q_C	Critical Heat flux
$q_{CHF,sat,}$	Critical Heat flux at saturation flow condition
$q_{CHF,sub}$	Critical Heat flux at sub-cooled flow condition
w	flow channel width
x_{exit}	Thermodynamic quality at exit $\left(x = \frac{h-h_f}{k_{fg}}\right)$

Greek Symbols

Δh_{in}	Sub-cooled Inlet enthalpy (KJ/Kg)
ρ_l	Density of liquid
ρ_g	Density of gas
λ	Latent heat of evaporation (K/Kg)
μ_l	liquid phase dynamic Viscosity [kg/m-s]
μ_g	gas phase dynamic Viscosity [kg/m-s]
γ	$\left\lvert\frac{\partial(\rho_l/\rho_{g)}}{\partial P}\right\rvert at\ satration$
φ_{CHF}	Modeling parameter

Acronyms

AP-	Atmospheric Pressure-(Plasma)
CHF	Critical Heat Flux
ONB	Onset of nucleating boiling
M	Modeling fluid
P	Prototype fluid

References

Collier, J.G., Thome, J.R., 1994. Convective Boiling and Condensation, Oxford University Press, Oxford, pp. 329–367

Hewitt, G.F., 1982. Burnout. In: Hetsroni, G. (Ed.), Handbook of Miltiphase Systems, vol. 1. Hemisphere Publishing Corporation, USA

Moon, S.K., Baek, W.P., Chang, S.H., 1996. "Parametric trend analysis of the critical heat flux based on artificial neural networks", Nucl. Eng. Des. 163, 29–49

Lee, D.H., 1977. Prediction of burnout in two-phase flow and heat transfer, p. 296, Oxford university press, Oxford 1977

Katto, Y., 1979. An analysis of the effect of inlet subcooling on critical heat flux of forced convection boiling in vertical uniformly heated tubes, Int. J. Heat and Mass Transfer,. Vol. 22, pp 1567-1575

Mishima, K., Nishihara, H., Michiyoshi, I., 1985. Boiling burnout and flow instabilities for water flowing in a round tube under atmospheric pressure. Int. J. Heat Mass Transfer 28, 1115–1129.

Chang, S.H., Baek, W.P., Bae, T.M., 1991. A study of critical heat flux for low flow of water in vertical round tubes under low pressure. Nucl. Eng. Des. 132, 225–237.

Bergles, A.E., 1977. Burnout in boiling heat transfer, Part II: subcooled and low quality forced convection systems. Nucl. Safety 18, 154–167

Kim, S.J., 2009 "Subcooled flow boiling heat transfer and critical heat flux in water-based nanofluids at low pressure" PhD Dissertation Thesis, MIT

Kim, C.H., 2000, "Critical heat flux of water in vertical round tubes at low pressure and low flow conditions", Nuclear Engineering and Design 199(2000) 49-73

Barnett, P.G., 1963, "The Scaling of Forced Convection Boiling Heat Transfer," U.K.A.E.A. Report, AEEW-R134, Winfrith, Dorset, England

Barnett, P.G., 1964, "An Experimental Investigation to Determine the Scaling Laws of Forced Convection Boiling Heat Transfer. Part 1: The Preliminary Examination of Burnout Data for Water and Arcton 12," U.K.A.E.A. Report, AEEW-R363, Winfrith, England

Barnett, P.G., and Wood, R.W., 1965, "An Experimental Investigation to Determine the Scaling

Laws of Forced Convection Boiling Heat Transfer. Part 2: An Examination of Burnout Data for Water, Freon 12 and Freon 21 in Uniformly Heated Round Tubes," U.K.A.E.A. Report, AEEW-R443, Winfrith, England

Ahmad, S.Y., 1973, "Fluid to Fluid Modeling of Critical Heat Flux: A Compensated Distortion Model," International Journal of Heat and Mass Transfer, 16(3), pp. 641-662.

Katto, Y., 1978, "A Generalized Correlation of Critical Heat Flux for the Forced Convection Boiling in Vertical Uniformly Heated Round Tubes." International Journal of Heat and Mass Transfer, 21(12), pp. 1527-1542.

ASHRAE, 2001, 2001 Fundamentals Handbook, American Society of Heating, Refrigerating and Air-Conditioning Engineers, Atlanta, Georgia, USA

Chen, et al., 2010, "Fluid to fluid modeling scaling factors of R134a-water" Proceeding of the 14th international heat transfer conference, IHTC14

Yan, J.L., and Yu, X.F., 1995, The Thermal Properties of Water and Vapor, 2nd edition, Higher Education Press, Beijing, China, pp. 1-15.

Groeneveld, D.C., et al., 2006 "The 2005 look-up table for critical heat flux in tubes" Nuclear Engineer and Design, Vol. 237, pp 1909-1922

5.Model Development and Validation work

Chapter 5 proposes the analytical CHF prediction model development based on bubble force balance and its validation work with current R-134a flow boiling CHF test data and other previous CHF data from literatures. In addition, the result of surface modification from AP-plasma coating in term of contact angle and coating thickness measurements are discussed. The effect of surface contact angle is investigated by both experimental and analytical model validation method.

5.1 CHF Prediction Model Development Using Force Balance

This section presents the development of CHF prediction model based on a force balance method with the concept of surface wettability. The theoretical models available in literature have not incorporated surface characteristic effects. These effects are considered indirectly through the changes in bubble size and number of nucleation sites in some existing models. In this study, an analytical model is presented which directly incorporates the effect of dynamic contact angle of bubbles on CHF. The model is tested with our flow boiling CHF data sets and also will be validated with available CHF data sets in literature for different fluid conditions.

Chang (1961) first considered that the force balance on a bubble might lead to CHF conditions. Later the model of Katto and Haramura (1983) also focused on the bubble behavior

and onset of CHF by considering the presence of a thin macro-layer underneath a bubble. This allows us to understand that the mechanisms leading to CHF are more intimately connected to the bubble events occurring in the vicinity of heater surface. The proposed analytical CHF model for flow boiling condition is developed based on the balance of forces at the interface, where the bubble is being generated and leaves the surface. The force balance with dynamic contact angle concept for pool boiling condition was first proposed by Kandlikar (2002). Similar concept is applicable for flow boiling conditions by including additional forces due to fluid motion in flow boiling condition. The movement of bubble interface can be analyzed in a two-dimensional plane shown in figure 5.1.

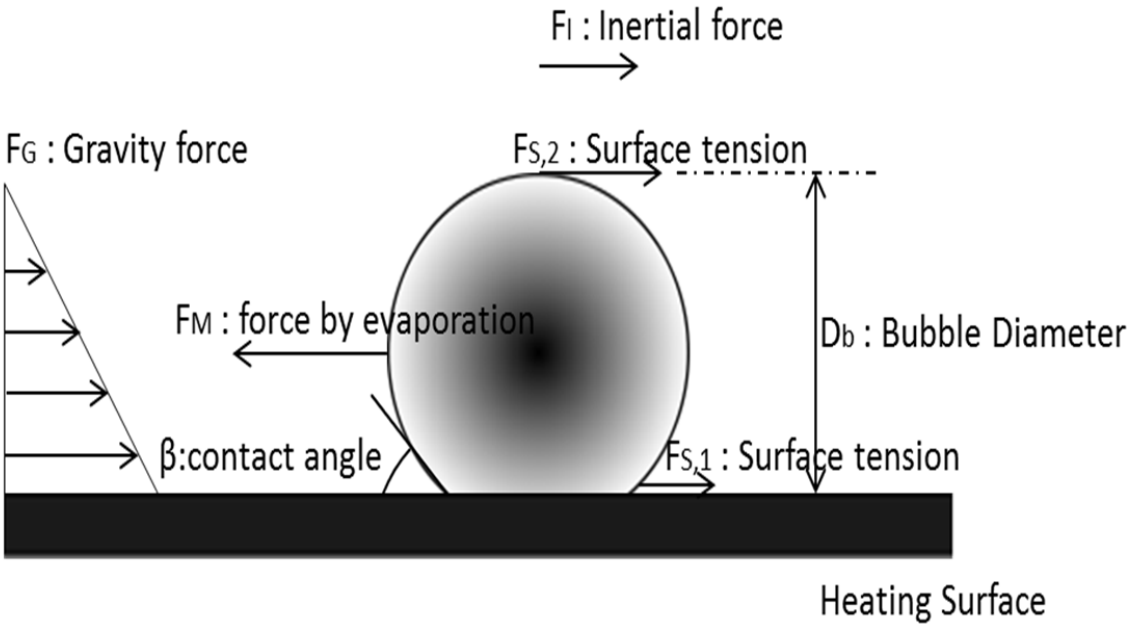


Figure 5.1 A force balance acting on a bubble parallel to the heating surface.

The surface tension forces act on the bubble surface. For a unit length in the direction parallel to the plane, Fs, 1 and Fs, 2 are given by

$$F_{S,1} = \sigma \cos\beta \quad , F_{S,2} = \sigma \tag{5.1}$$

where, σ is surface tension, N/m, and β is the receding contact angle of the liquid-vapor interface with the solid heater surface. The evaporation at the interface results in a force due to the change in momentum as vapor leaves the interface. The resulting force by the momentum change is given by the product of the evaporation mass flow rate and the vapor velocity near at the surface.

$$F_M = \frac{q'' D_b \cdot 1}{h_{fg}} \frac{q'' \cdot 1}{h_{fg}\rho_g} = \left(\frac{q''}{h_{fg}}\right)^2 \frac{D_b}{\rho_g} \cdot 1 \tag{5.2}$$

The force due to gravity on the bubble interface acting in the direction parallel to the heater surface from the triangular pressure distribution. The gravity force due to the hydrostatic head on a surface on a unit width is given by;

$$F_G = \frac{1}{2}(\rho_f - \rho_g) g (D_b)^2 \cdot 1 \tag{5.3}$$

The inertial force resulting from the flowing fluid can be expressed by ρV^2. This force is given by;

$$F_I = \frac{1}{2}\rho_f V^2 D_b = \frac{G^2 D_b}{2\rho_f} \tag{5.4}$$

A proposed flow boiling CHF prediction model is developed based on a force balance as shown in Figure 11. In the current model, it is assumed that the critical heat flux or CHF occurs when the force due to the momentum change F_M pulling the bubble interface into the liquid along the heated surface exceeds the sum of the forces holding the bubble, $F_{S,1}$, $F_{S,2}$, F_G, and F_I . The bubble then expands along the heater surface, blankets it, and form vapor film. At the inception of the CHF condition, the force balance yields;

$$F_M \sim F_{S,1} + F_{s,2} + F_G + F_I \tag{5.5}$$

Substituting Equations (5.1) – (5.4) into Eq. (5.5), we obtain the following correlation based on the heat flux.

$$q'' \sim h_{fg}\sqrt{\frac{\sigma\rho_g(1+cos\beta)}{D} + \frac{\rho_f\rho_g gD(1+cos\beta)}{2} + \frac{\rho_g G^2}{\rho_f}} \tag{5.6}$$

This heat flux is related to the CHF in flow boiling condition. Since this relation is not explicitly known, a constant C is introduced to predict the CHF based on the experimental data. Then, the current proposed analytical CHF prediction correlation is expressed as;

$$q'' = Ch_{fg}\sqrt{\frac{\sigma\rho_g(1+cos\beta)}{D} + \frac{\rho_f\rho_g gD(1+cos\beta)}{2} + \frac{\rho_g G^2}{\rho_f}} \tag{5.7}$$

As mentioned in chapter 4, there are several apparent results on the effect of sub-cooled inlet temperature in which an increase in sub-cooled level leads to increasing of CHF in flow boiling condition. The effect of sub-cooling has been observed a linear relationship between the

degree of sub-cooling and CHF for water at various pressures (Kutateladze, et al., 1964). A linear relationship of CHF with inlet sub-cooled temperature was obtained by Jakob and Fritz (Jakob et al., 1931). Elkassabgi, et al., (1988) conducted experiments with sub-cooled pool boiling with R-113 and isopropanol and identified two regions depending on the level of sub-cooling (low sub-cooling level and high sub-cooling level). At relatively low sub-cooling levels, CHF increased linearly, while at very large sub-cooling condition, CHF was insensitive to changes in sub-cooling levels. It is proposed that an increase in sub-cooled temperature of the bulk liquid increases the transient conduction to the liquid. The CHF under sub-cooled condition, therefore, is then given by;

$$q''_{CHF,subcooled} = q''_{CHF,saturation}\left(1+\frac{\Delta h_i}{h_{fg}}\right) \tag{5.8}$$

For sub-cooled flow boiling condition, the sub-cooling effect on CHF should be applied to the prediction model. The equation (5.7) can be expanded as follows for sub-cooled flow boiling case:

$$q''_{CHF,subcooled} = Ch_{fg}\sqrt{\frac{\sigma\rho_g(1+cos\beta)}{D}+\frac{\rho_f\rho_g gD(1+cos\beta)}{2}+\frac{\rho_g G^2}{\rho_f}}\left(1+\frac{\Delta h_i}{h_{fg}}\right) \tag{5.9}$$

In the present proposed correlation, with given measure value of system pressure, mass flux, inlet sub-cooled enthalpy (macroscopic operating parameters), and contact angle (microscopic surface wetting parameter), the CHF value can be directly predicted. Regarding the bubble departure diameter which is one of input value for current correlation, at the low

pressure conditions, Fritx (1935) suggested the following correlation based the theory of capillarity to obtain an equilibrium bubble shape and a differential equation that represents a balance of gravity and surface tension force with surface wettability concept

$$\mathrm{D} = 0.208\beta\sqrt{\frac{\sigma}{g(\rho_l-\rho_g)}} \tag{5.10}$$

where $\beta, \sigma, \mathrm{g}, \rho_l, and\ \rho_g$ are static contact angle, surface tension, gravity constant, liquid density, and vapor density, respectively. This correlation initially was developed for pool boiling conditions and hence, its applicability to flow boiling is therefore questionable. In current model, constant value of 0.1 was used instead of 0.208 β, which show reasonably good agreement with measurement of bubble departure diameter through high speed camera observation under the current operating condition.

Based on current sub-cooled CHF databases, the value of C is calculated as 0.0391. The results are included in figure 12, which indicates that 7.68 % of maximum deviation and 2.77% of mean absolute deviation (MAD) with current CHF measurements. In this study, maximum deviation and mean absolute deviation (MAD) method are utilized to perform the validation of proposed CHF correlation with current experimental data. Furthermore, other CHF data from open literature is also validated with the proposed CHF correlation and evaluated if the correlation is applicable for the broad range of operating condition. The mean absolute deviation (MAD) method is defined in eq. (5.11).

$$\text{Mean Absolute Deviation (MAD)} = \frac{1}{M}\sum \frac{\left|q''_{CHF,expt} - q''_{CHF,pred}\right|}{q''_{CHF,expt}} \times 100\% \quad (5.11)$$

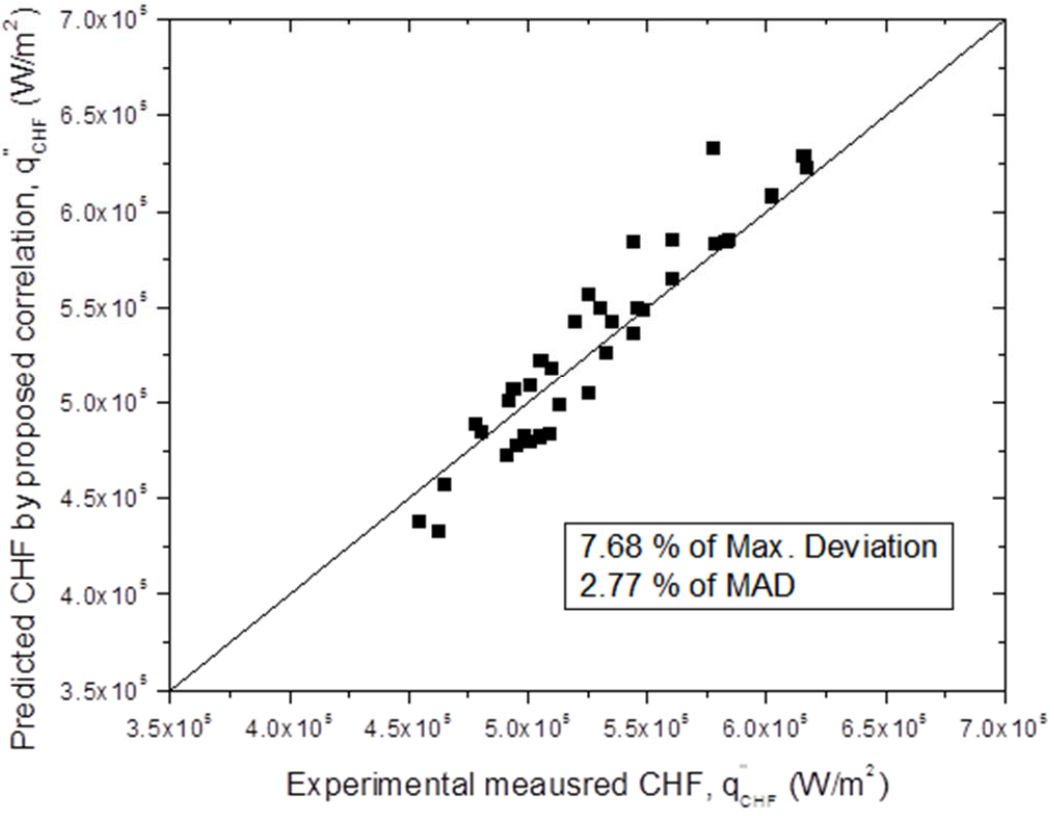


Figure 5.2 The comparison of CHF predicted from proposed model and experimental CHF data

5.1.1 Katto CHF correlation (1984) for current experimental CHF result and comparison

There are several CHF prediction correlations which are claimed to cover low flow, low pressure (LPLF) conditions with quite a good accuracy (Bowring, et al., 1972; Katto et al., 1984;

Shar, et al., 1987; Weber et al., 1990; Chang et al., 1991; Baek et al., 1995; Groeneveld et al., 1996; Baek et al., 1997]. Those previous researchers have investigated the CHF mechanism and proposed CHF correlation, for which they obtained CHF points from various experiments and from the studies in the literature. In this section, Katto correlation (1984) is described and compared with current CHF experimental data. Katto presented the improved version of generalized CHF correlation in uniformly heated surface covering various fluids based on the inlet condition. Basically, Katto correlation incorporates with three key parameters; system pressure, mass flux, and sub-cooling inlet enthalpy, which is similar to what was considered in our CHF model excluding surface wettability feature.

The Katto's CHF correlation is;

$$q_c = q_{co}\left(1 + K\frac{\Delta h_i}{h_{fg}}\right) \tag{5.12}$$

Since the density ratio of vapor to liquid is less than 0.15 for the testing pressure range of R-134a, q_{co} is obtained from the minimum value as follows:

$$\frac{q_{co}}{Gh_{fg}} = \min\left(\frac{CW^{0.043}}{L/D}, \frac{0.1(\rho_g/\rho_f)^{0.133}W^{0.333}}{1+0.0031(L/D)}, \frac{0.098\left(\frac{\rho_g}{\rho_f}\right)^{0.133}W^{0433}(L/D)}{1+0.0031(\frac{L}{D})}\right) \tag{5.13}$$

The non-dimensional parameter, K is obtained from the maximum values as follows:

$$K = \max\left(\frac{1.043}{4CW^{0.043}}, \frac{\left(\frac{5}{6}\right)(0.0124+\frac{D}{L})}{(\rho_g/\rho_f)^{0.133}W^{0.333}}\right) \tag{5.14}$$

where, $W = \frac{\sigma \rho_f}{G^2 L}$, $C = 0.25$.

The Katto correlation shows good agreement with other experiments (Katto et al., 1984). Simply Katto correlation utilizes three physical operating parameters (pressure, mass flux, sub-cooling level) and one geometrical parameter (ratio of diameter of channel and heated length) to predict CHF. Prediction by Katto correlation for the current experimental data sets is shown in figure 5.4. It is noted that Katto correlation under-predicts the CHF value compared to the measured CHF value in present experimental test. Figure 5.4 indicates that 23.1 % of maximum deviation and 12.1% of mean absolute deviation (MAD) with comparison with current CHF measurements. However, this is still a reasonable error band in general empirical CHF prediction correlation. The detail calculation procedure of Katto correlation is tabulated in appendix C.

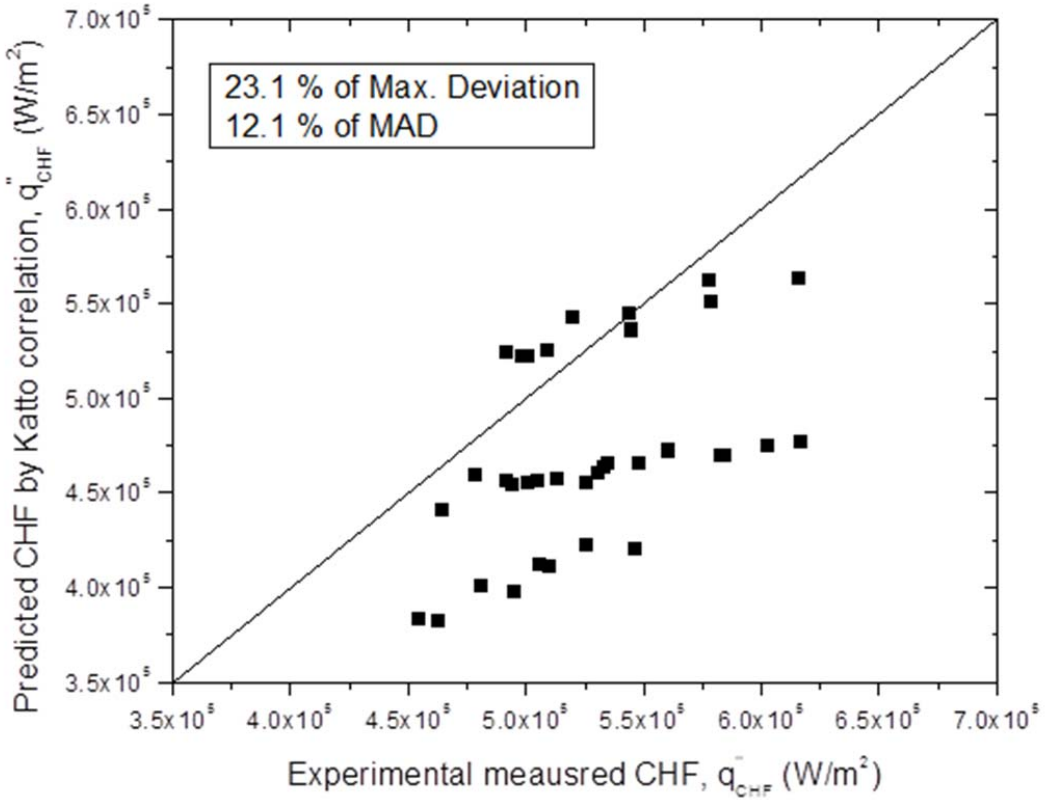


Figure 5.3 The comparison of CHF predicted from Katto correlation and experimental CHF data

5.1.3 Bowring CHF correlation (1972) for current experimental CHF result and comparison

The correlation of Bowring was developed for CHF prediction for water with fixed inlet condition. The correlation is

$$q_c = \frac{A' + 0.25DG\Delta h_i}{C' + L} \tag{5.15}$$

where, $A' = \frac{0.5792 h_{fg} DGF1}{1+0.0143 F2 D^{0.5} G}$, $C' = \frac{0.077 F3 DG}{1+0.347 F4 (\frac{G}{1356})^n}$.

F1, F2, F3, F4 and n are the function of a non-dimensional pressure, P'=P/68.95.

$$n = 2 - 0.5P' \tag{5.16}$$

$$F1 = P'^{-0.368} exp[0.648(1 - P')] \tag{5.17}$$

$$F1/F2 = P'^{-0.448} exp[0.0245(1 - P')] \tag{5.18}$$

$$F3 = P'^{0.213} \tag{5.19}$$

$$F4 = F3 \cdot P'^{1.649} \tag{5.20}$$

The correlation proposed by Bowring (1972) is applicable for the pressure of 2–190 bar, tube diameter of 2–45 mm, tube length 0.15–3.7 m and mass flux of 136–18,600 kg/m2 s. Since this correlation is applicable for water only, the present CHF data of R-134a are first converted into water-equivalent values using the fluid-to-fluid scaling method presented in previous chapter 4. Converted water-equivalent CHF data is summarized in Table 4.5. Figure 5.5 shows the comparison of the water-equivalent CHF data converted from the CHF data in R-134a with the CHF prediction using Bowring correlation with assumption of identical geometry condition. The maximum deviation and mean absolute deviation (MAD) of the prediction by Bowring's correlation are 67.68% and 52.77%, respectively.

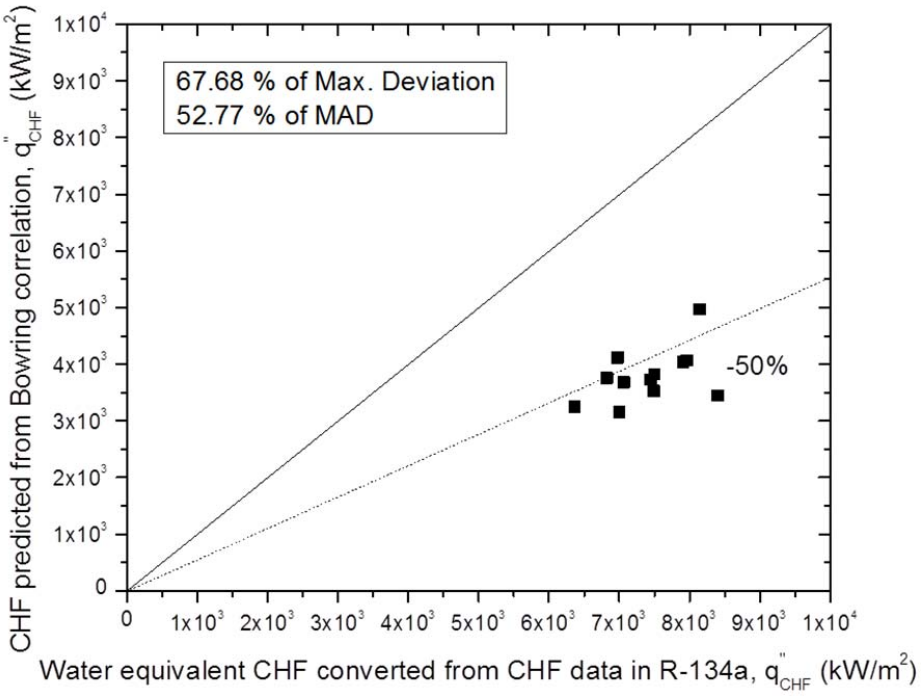


Figure 5.4 The comparison of the water-equivalent CHF data with the predicted CHF by Bowring correlation

The summary of maximum deviation and mean absolute deviation (MAD) of CHF prediction correlations (i.e., proposed correlation, Katto correlation, Bowring correlation) for current experimental CHF value is listed in table 5.1

Table 5.1 The summary of maximum deviation and MAD value for three CHF correlations.

	Maximum Deviation (%)	Mean Absolute Deviation (%)
Proposed correlation	7.68	2.77
Katto correlation	23.1	12.1
Bowring correlation	67.68	52.77

5.2 Validation of Proposed Correlation with Other CHF Results from Open Literature

In this section, the proposed CHF prediction correlation is validated with open literature CHF data obtained in various operating conditions. The empirical CHF prediction correlation proposed in chapter 4 is based on only current experimental conditions. Thus the validation for empirical CHF correlation is excluded due to lack of applicability for different operating conditions. However, the proposed analytical CHF prediction correlation based on the bubble force balance method developed in previous section possesses the universal application feasibility over large range of operating conditions. In order to evaluate applicability of the proposed correlation, it is noted that operating conditions (i.e., system pressure, mass flux, inlet sub-cooling temperature, and type of fluids) is required to predict the CHF value. Including current CHF test in flow boiling, other 5 researcher's CHF data in flow boiling condition in literature are selected for the validation work.

Due to lack of flexibility of the current experimental apparatus, hydraulic diameter effects on CHF were not examined. Even though proposed CHF prediction correlation does not contain hydraulic diameter information, this correlation can be expanded for different geometry by using equation (2-7) which is widely used in the CHF look up table (refer to chapter 2.4). The proposed CHF prediction correlation for the current experimental condition can be improved by adding more CHF data with a wider range of key parametric conditions. In this validation work, 36 current CHF measure value are selected for the comparative study between author's proposed

CHF correlation and most well accepted Katto CHF prediction correlation. Katto proposed a revised generalized correlation applicable for a range of fluids (i.e. water, R-12, R134a). The correlation is a non-local correlation that consists of four equations (refer chapter 5.1.1). The effect of inlet sub-cooling on the CHF is included in the correlation. The correlation requires an inlet sub-cooled enthalpy, a system pressure, mass flux, and geometry of heating section.

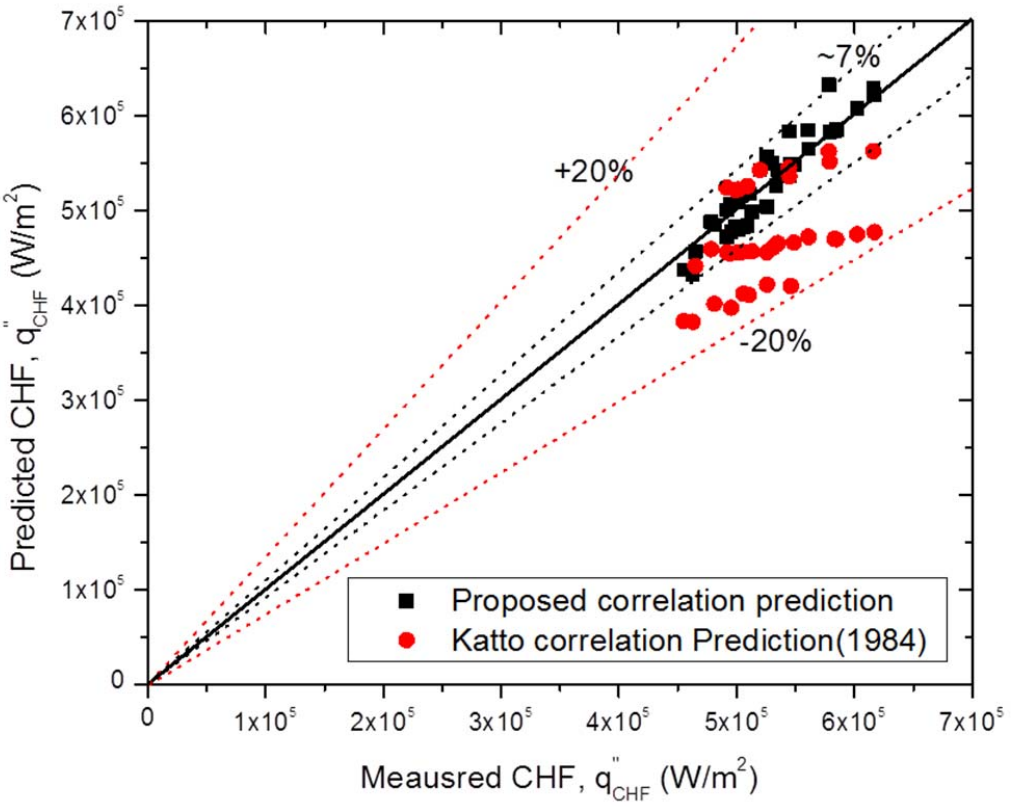


Figure 5.5 The comparative study between proposed correlation prediction and Katto (1984) CHF prediction correlation

Figure 5.5 shows the comparison between the prediction accuracy of proposed correlation and that of Katto CHF correlation. The maximum deviation for both correlations (author, and Katto) under the identical operating input parameters (system pressure, mass flux, inlet sub-cooled enthalpy) are 7% and 20% respectively. In the calculation of proposed correlation, the static contact angle value for copper surface is measured and utilized as 80° in proposed correlation. It is found that the Katto correlation generally under predicts the CHF value in given condition, which is also consistent with other researcher founding (Chang et al., 2005).

For the applicability study in proposed correlation, a total of 105 data points of CHF in flow boiling of either water or R-134a as working fluid were collected from 5 researcher's CHF value in open literature. Experimental CHF measurement data used here are those presented by Lee et al. (2008), Bang et al. (2002), Van Der Mollen et al. (1978), Kim et al. (2009), Kim et al. (2010), and author CHF data. The data used in the present analysis are pre-screen data via heat balance methods, and they are comprised of 25 data from Lee et al. (2008), 12 data from Bang et al. (2004), 12 data from Van Der Mollen et al. (1978), 20 data from Kim et al. (2009), 36 data from author. The ranges of the collected experimental data are 1 bar≤P (pressure)≤20 bar, 100 kg/m^2-s≤G (mass flux)≤2512 kg/m^2-s, 11kJ/kg≤ Δh_i (inlet sub-cooled enthapy)≤249.kJ/kg, respectively. The detail information of range of each group's operating conditions is summarized in Appendix A.

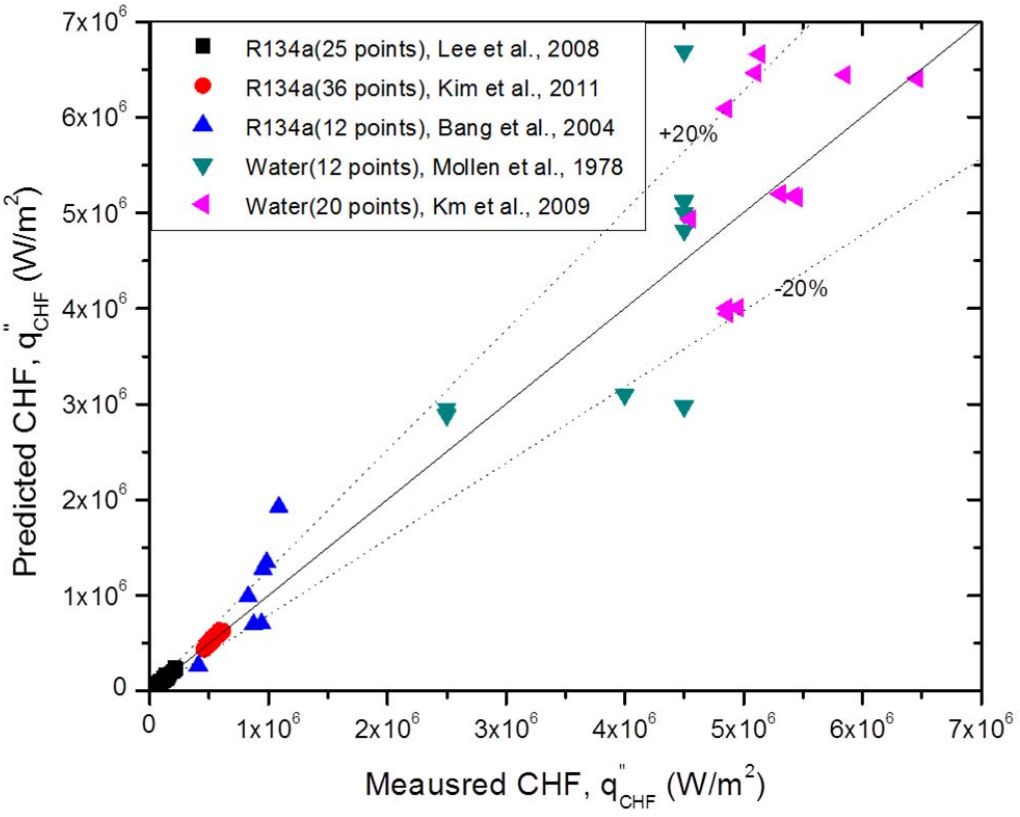


Figure 5.6 The comparison between CHF predictions by proposed correlation and 5 other researcher's CHF measurement (105 CHF data).

To improve feasibility of the proposed CHF correlation, it is required to collect more CHF data points with extended experimental condition as well as, to include static contact angle information in flow boiling condition. Unfortunately a few flow boiling CHF enhancement tests with static contact angle measurements have been found in the literature. The literature of surface modification by nanoparticle deposition in flow boiling condition is in the early stage of investigation of CHF enhancement with surface feature (Kim et al., 2005). The conclusion from

nanoparticle deposition studies in flow boiling condition (Kim et al., 2009) is that addition of nanoparticles in the working fluid provides the nanoparticle deposition by boiling process at the interface between liquid and solid surface and generates a surface with enhanced wettability and reduced the contact angles. Kim et al. (2009) reported the 35~55% CHF enhancement by using nanoparticle inserted fluid of water. In addition static contact angle are measured for experimental CHF test.

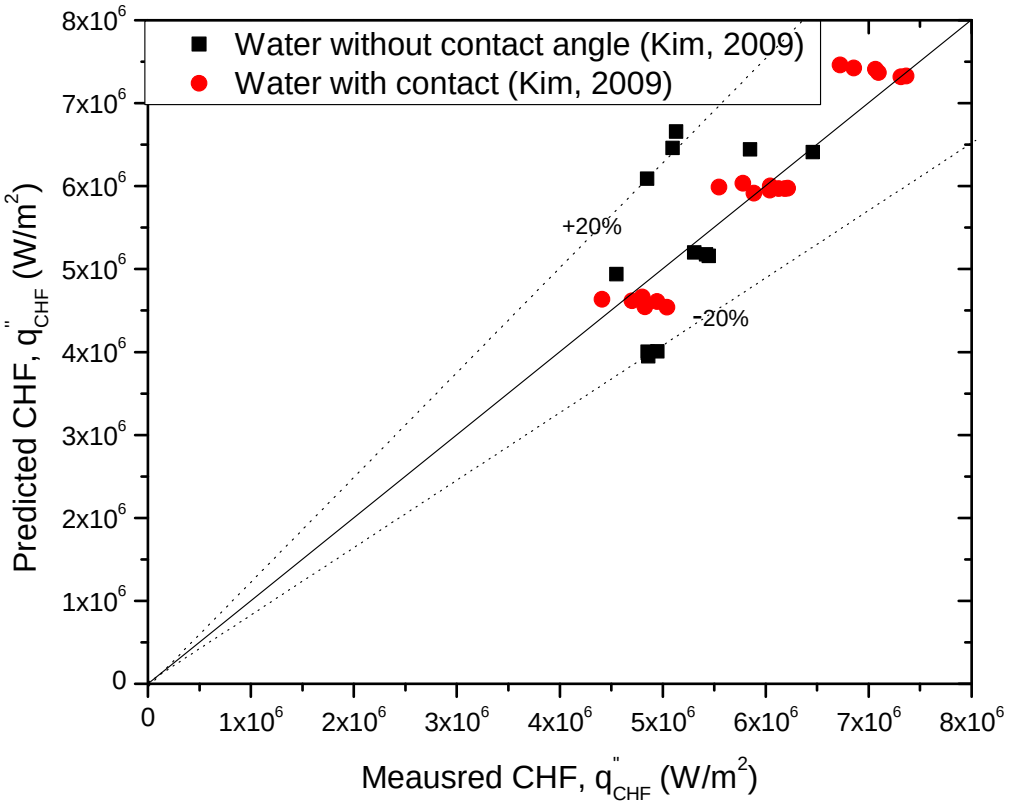


Figure 5.7 The comparative study between CHF prediction by the author's proposed correlation with contact angle and CHF prediction without contact angle.

Therefore, we conduct the validation work of our proposed correlation with Kim et al. (2011) with consideration of surface wettability on CHF enhancement. The figure 5.7 shows the comparison between the CHF prediction by proposed correlation for Kim's CHF data with considering contact angle measurement and without considering contact angle measurement. The maximum deviations of CHF prediction is calculated as 20% without contact angle parameter (inserting the reference contact angle of 80°) and 7% with contact angle parameter (inserting the measured contact angle 10°∼15°). It is found that the proposed correlation shows better prediction accuracy when the surface is modified. Furthermore, the enhancements of CHF results are observed both in experimental result and analytic correlation prediction.

5.3 Enhancement of CHF under Flow Boiling Condition with Surface Modification by AP-Plasma

Atmospheric pressure (AP) plasma coating has been applied for surface modification of copper heating block. The nitrogen gas is fed into the upper-grounded electrode, the lower electrode is connected to the high-voltage power supply and covered with a layer of dielectric, and then a stable plasma spray is formed and blown out into air. Many plasma applications in the surface modification are made at reduced pressure in the order of 1-10 Pa, and many kinds of low-pressure plasma systems have been developed up to now (Cheng et al., 2006; Shenton, et al., 2001). Generally, these plasma systems require vacuum equipment, which make complexity and cost for materials processing. AP-plasma, however, can provide an advantage over the low pressure plasma system because they do not need vacuum equipment and they have been shown

to be of prospect for a number of industrial applications. The AP-plasma gas temperature is only 25℃~30℃, thus thermal damage to treated materials can be easily avoided. For these reasons, they can be easily employed in this experimental setting for modifying surface to hydrophilic. AP-plasma have shown great promise when applied to change the surface properties of metals, and the better hydropilicity of metal surface is achieved (Borcial, et al., 2003; Tanaka, et al., 2001).

5.3.1 Observation on treated surface with SEM image and XPS

In this research, we introduce a state of art technique of atmospheric pressure plasma coating which is excited by a low frequency (30kHz) of 12 kV and 2.8 kW DC power supply, the gas temperature of AP-plasma is almost room temperature 25℃~30℃ , so the plasma jet spray is more suitable for treating vulnerable object. The gap between plasma spray and copper block is fixed as 2.5mm. And AP-plasma treatment time for copper is set as 80 sec for each surface treatment manually. The surface was initially cleaned with air blower and acetone leasing to eliminate any impurity on treated surface. After AP-plasma treatment is completed, the treated surface was sealed by contamination free paper till the test section is remounted into the flow loop. With the AP-plasma, hydrophilic surface fabrication process was conducted by using nitrogen gas with small amount of air or hydrogen insertion. In order to understand the mechanism of surface reaction, the surface morphologies of treated samples were characterized by scanning electron microscopy (SEM) and investigated chemical change on the copper surface by X-ray photoelectron spectroscopy (XPS) shown in figure 5.8.

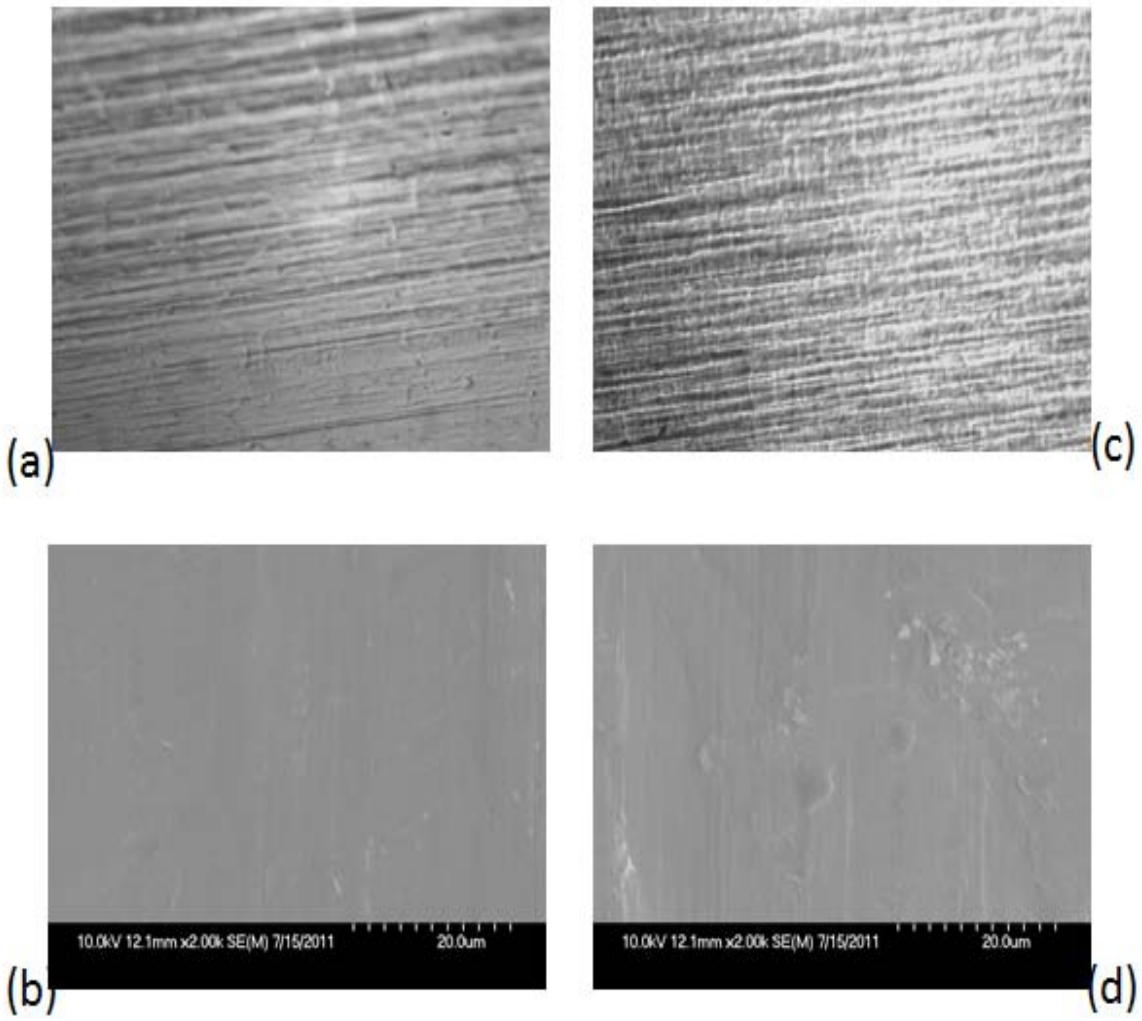


Figure 5.8 Observation of copper surface with and without treatment (a) ×500 optical CCD image on untreated pure Cu surface, (b) SEM image for Cu surface before plasma treatment, (c) ×500 optical CCD image on plasma treated Cu surface, (b) SEM image for Cu surface.

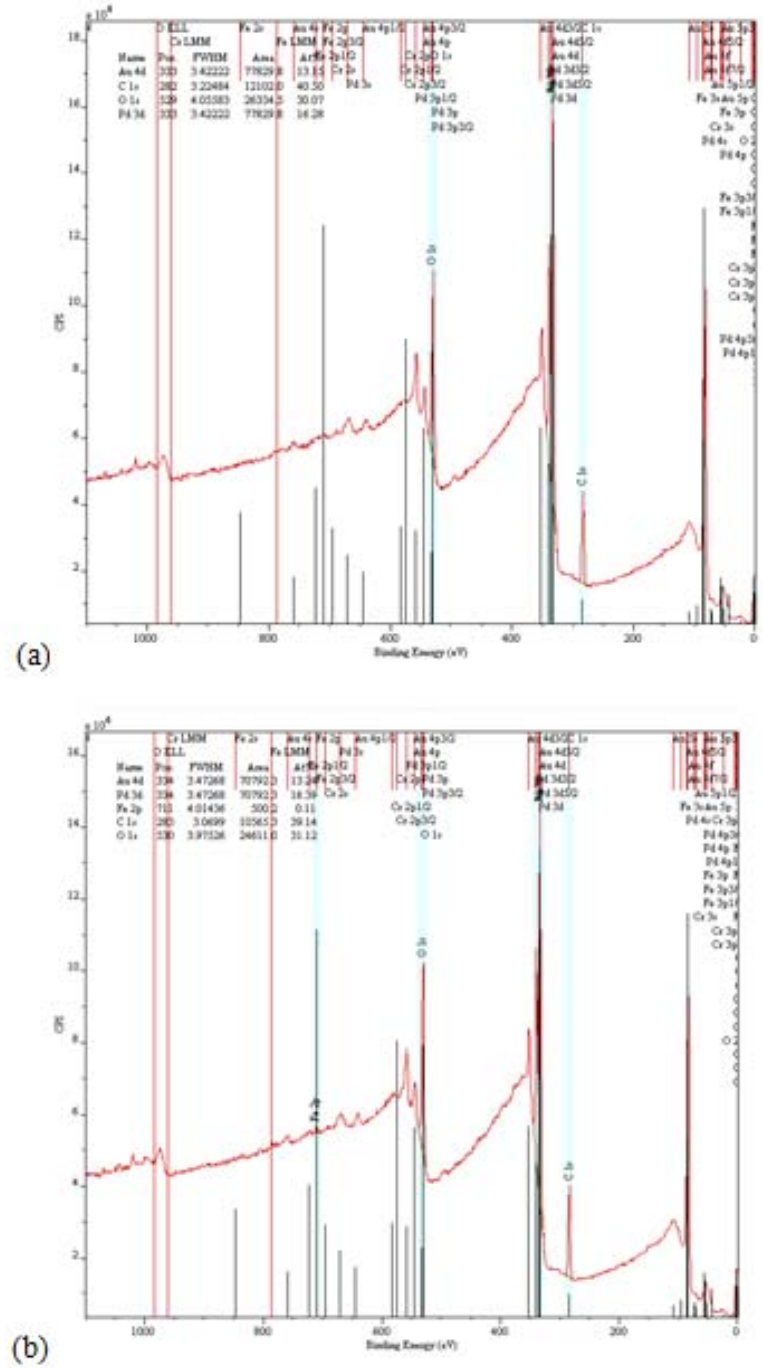


Figure 5.9 The XPS spectra of untreated (a) and AP-plasma treated (b) copper surface.

The XPS spectra of untreated and treated copper surface are shown in Fig. 5.9, and the spectra mainly contains O1s (Oxygen compound) peaks. The magnitude of O1s peak increases in surface of copper block after AP-plasma treatment. These results suggest that the oxygen was incorporated into the surface of copper when treated by AP-plasma treatment. The introduction of oxygen-containing Copper compound (CuO, CuO_2) in surface may be the main reason for the hydrophilic feature improvement. It is considered that the oxidation copper film is generated on top of copper surface by following process. The excited oxygen atoms generated by AP-plasma may be incorporated into surface of copper, or recombine with another oxygen molecule generating ozone and then react with surface.

5.3.2 Surface features measurement (contact angle and coating layer thickness measurement)

In this section, we investigate the surface feature after AP-plasma treatment by using static contact angle measurement with sessile drop method and oxidation layer thickness measurement. In order to conduct several measurement of contact angle and thickness with different Ap-plasma operating time, copper coupons (diameter of 25.4mm with 3mm thickness, like a size of quarter coin), with identical properties to that of the copper test section was prepared. Figure 5.10 and 5.11 demonstrate the contact angle reduction and oxidation layer thickness along with increasing AP-plasma treatment time. The decrease of the water contact angle indicates that the chemical changes have taken place at the copper surface due to atmospheric pressure plasma treatment (Tanaka, et al., 2001). Thus, these changes make the treated copper surfaces more hydrophilic surface compared to the original copper surface. The

water contact angle of treated surface reduced to 15°~ 21°, after 400 second of AP-plasma treatment, from the original contact angle (~80°) of pure copper surface with water liquid drop as shown in figure 5.12. Figure 5.10 shows that overlong time of AP-plasma treatment may not always be good for retaining the most hydrophilic modification in term of contact angle reduction and oxidation layer thickness.

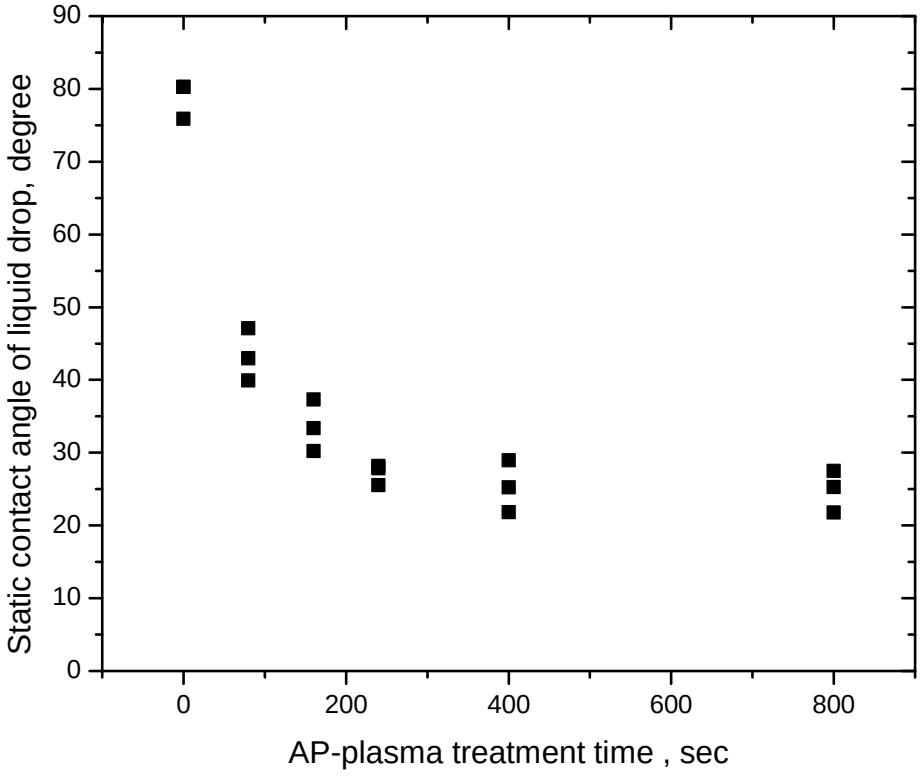


Figure 5.10 The contact angle measurements along with AP-plasma treatment time (80~800Sec)

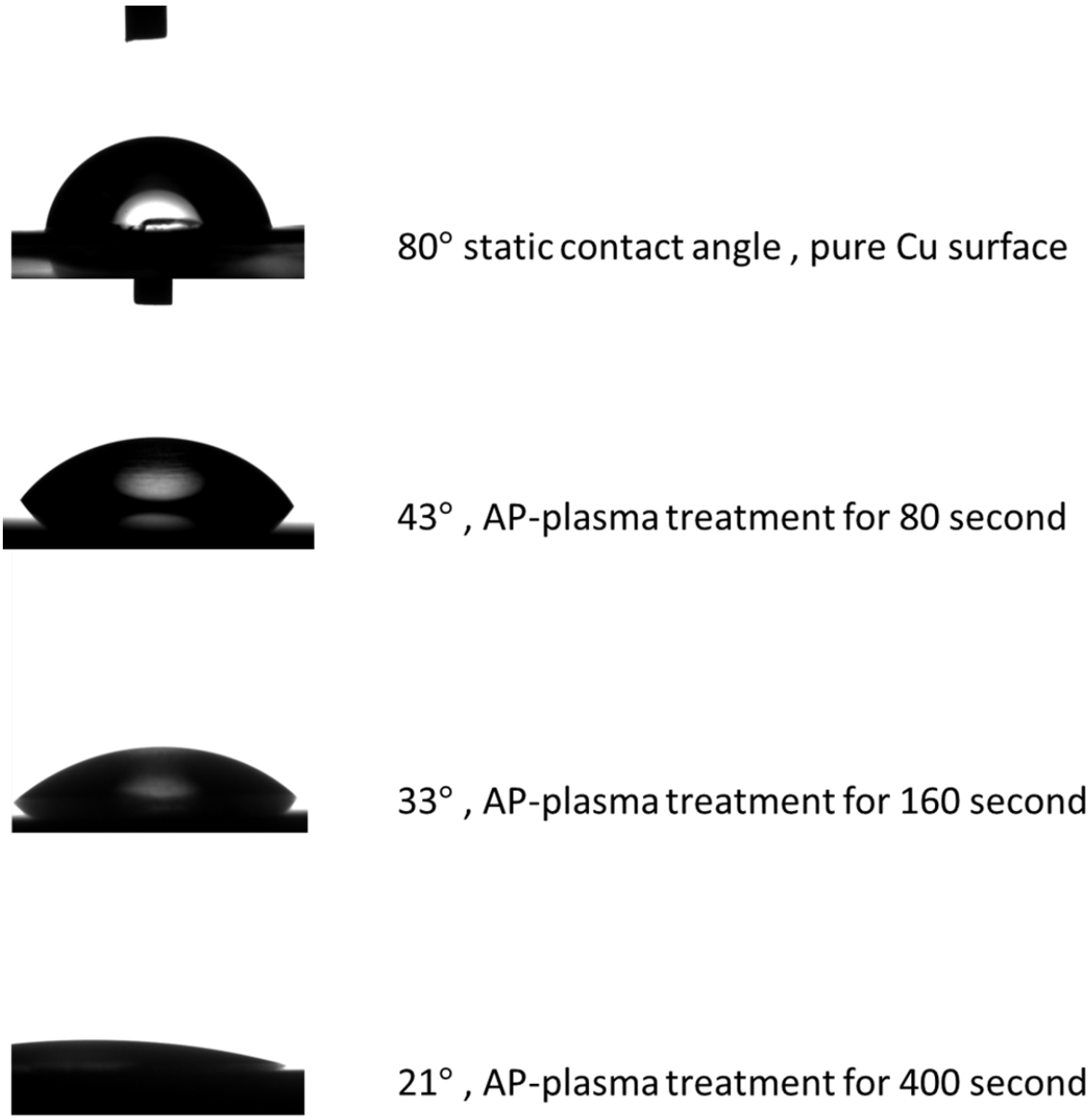


Figure 5.11 A series of picture of reduced contact angle along with increasing AP-plasma time.

The static contact angle is the contact angle that a droplet would form with a given material if the surface of that material were perfectly flat. It is well known that the static contact

angle is an important parameter in determining if a micro-cavity present on the surface can become an active site for bubble nucleation (a nucleation site) or not. Since the actual bubble dynamic contact angle on the heating surface under flow conditions are very hard to observe especially at high flow rate and high heat flux condition, the bubble dynamic contact angle measurements are difficult to achieved. Fortunately, the static contact angle of liquid can be measured from sessile drop method, and it is assumed that the bubble dynamic contact angle can be replaced with static contact angle of liquid drop test (Kandlikar et al., 2001). A schematic of the contact angle of liquid is given in Fig. 5.13. The static contact angle on a perfect smooth surface can be calculated by using Young's equation:

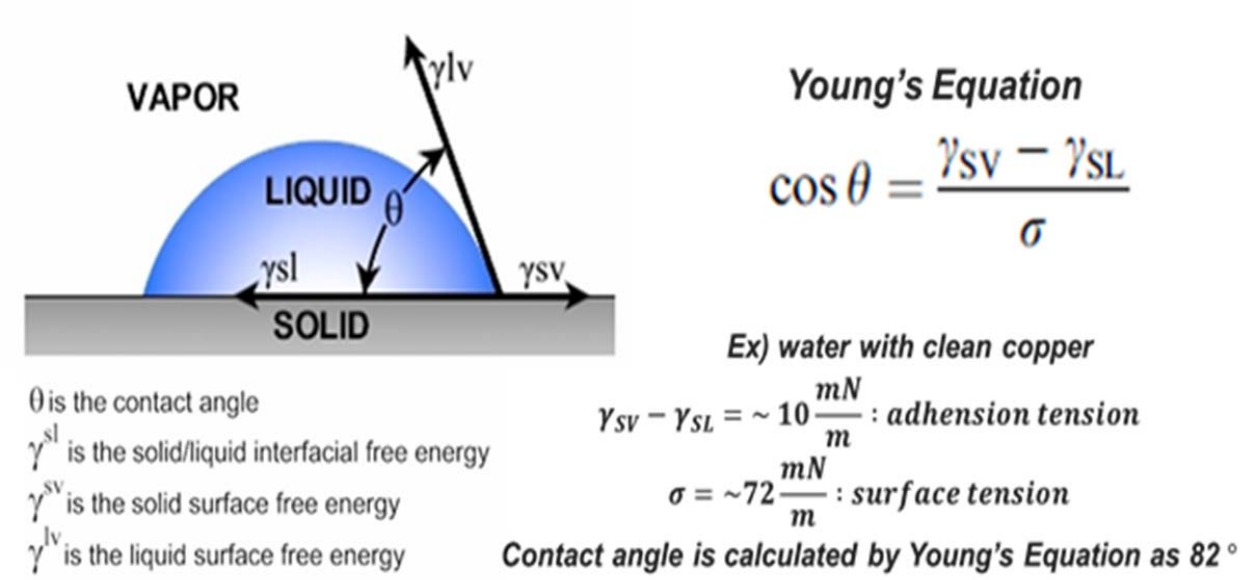


Figure 5.12 A schematic diagram of static contact angle of liquid and calculated contact angle of water on copper surface by Yong's equation.

where, $\theta, \sigma, \gamma_{SV}, \gamma_{SL}$ are the static contact angle, the surface tension at liquid-vapor interface, and the surface energies at the solid-vapor and solid-liquid interfaces, respectively. Note that some scattering on contact angle measurements are observed in the calculated values of θ. For simplicity, therefore, the value of static contact values (θ) was obtained from averaging the several measurements of contact angle on each AP-plasma treatment condition (see fig. 5.10). The corresponding average values of static contact angle are 80, 43, 33, and 21 for water on copper surface with AP-plasma treated time of 0, 80, 160, 400 second, respectively. The oxidation layer thicknesses with different AP-plasma coating conditions are measured by from Dektak3 surface profilometer, and the result is listed in figure 5.11. The thickness of oxidation layer on top of copper surface is saturated to about 3 micron with 400 second of AP-plasma operating condition.

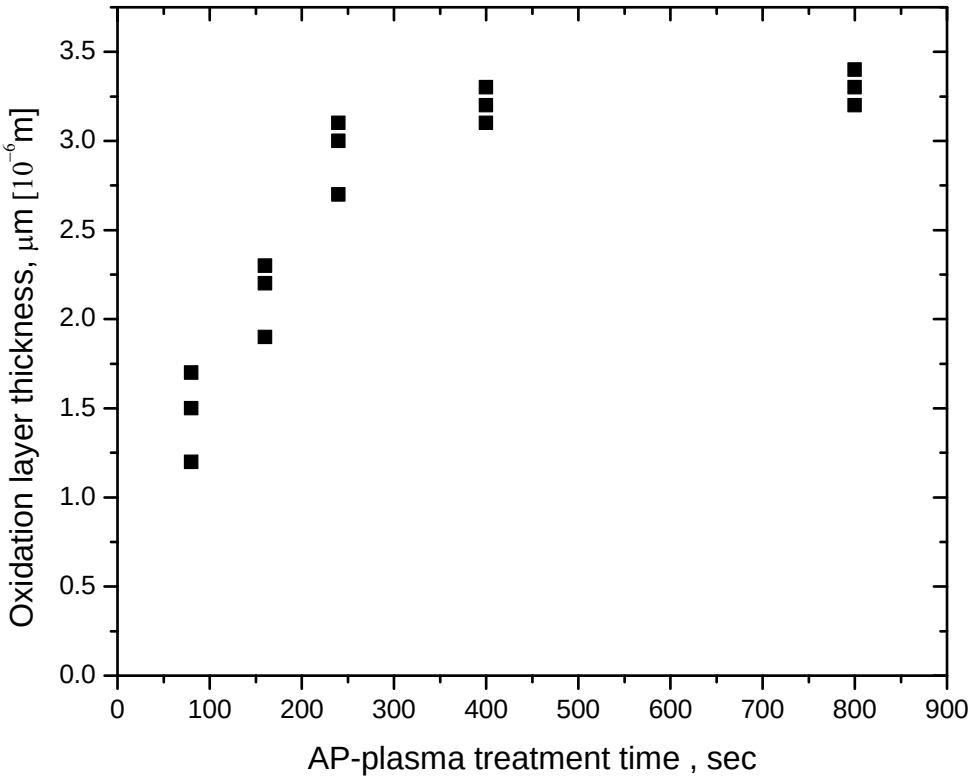


Figure 5.13 The oxidation layer thickness measurements along with AP-plasma treatment time (80~800Sec)

5.3.3 Enhancement of CHF with AP-plasma treated surface under flow boiling condition

Surface modification by AP-plasma treatment provides the reduction of contact angle as discussed in previous section. Unlike nanoparticle deposited flow boiling test in literatures related to nanofluid study, we prepare the surface medication before the flow test is conducted.

Modified surface is remounted into the flow boiling test loop and conducted the CHF measurement test under the condition (Pressure of 4 bar, mass flux of 124 kg/m^2-s and 14 KJ/Kg of inlet sub-cooled enthalpy). The contact angle of modified surface is measured as 18 degree, which is around 60 degree of contact angle reduction compared to contact angle of untreated original copper surface (~80 degree). The measurement of CHF value with untreated copper surface was 495 kw/m^2, however the measurement of CHF with AP-plasma treated copper surface was observed as 584 kW/m^2 under same operating condition (pressure, mass flux, inlet enthalpy is fixed as untreated surface condition). Thus, it was observed that 18 % of CHF enhancement was achieved when the static contact angle was reduced from 80 degree to 18 degree (see fig. 5.14). In order to achieve repeatability, several CHF measurement test were conducted in different operating condition with modified surface by AP-plasma. Enhancement of CHF of around 15 ~ 18% is consistently observed compared to that of untreated surface under identical operating conditions. This experimental observation demonstrates the reduction of contact angle result in the enhancement of CHF under flow boiling condition. In many literature, there has apparent CHF enhancement in pool boiling condition using nanoparticle to make surface hydrophilic (Kim et al., 2009; Bang et al., 2006). It is considered that current experimental result of CHF enhancement with AP-plasma treatment is consistent with previous finding and expands the prospect of CHF enhancement in flow boiling condition.

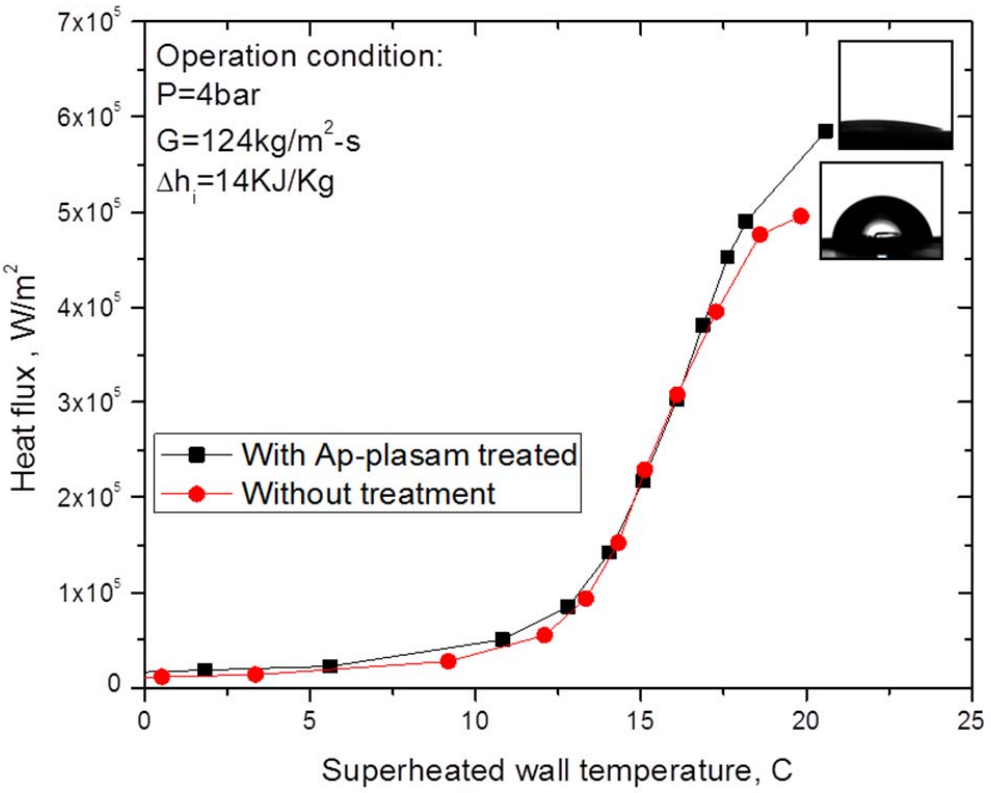


Figure 5.14 Comparison between CHF measurement with AP-plasma treatment and without treatment

In addition to, the experimental finding on CHF enhancement using surface modification, the proposed CHF correlation also predicts that the CHF value will be enhanced with same experimental operating condition only by changing static contact angle. In the proposed correlation, as the static contact angle is reduced from 80 degree to 10 degree under 4 bar of pressure, 124 kg/m^2-s, and 14 KJ/kg condition, the predicted CHF enhancement is calculated as 27% (see fig 5.15).

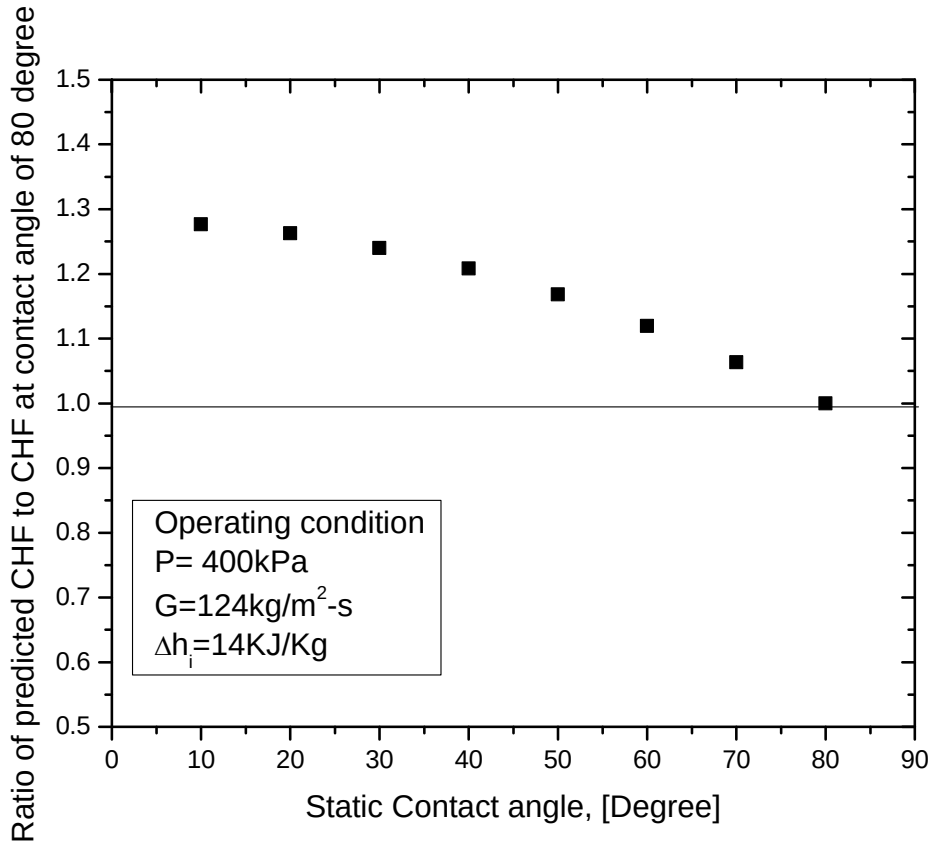


Figure 5.15 Predicted CHF enhancements by proposed correlation along with decreasing contact angle.

In addition to the effect of static contact angle on CHF, other operating parameters (i.e., system pressure, mass flux, and inlet sub-cooled enthalpy) effects on CHF are investigated from the proposed correlation. The effect of mass flux and inlet sub-cooled enthalpy on CHF shows same pattern that already observed in current experimental CHF test as shown in figure 5.16 and 5.17 (i.e., CHF increase as the mass flux increases and inlet sub-cooled enthalpy increases).

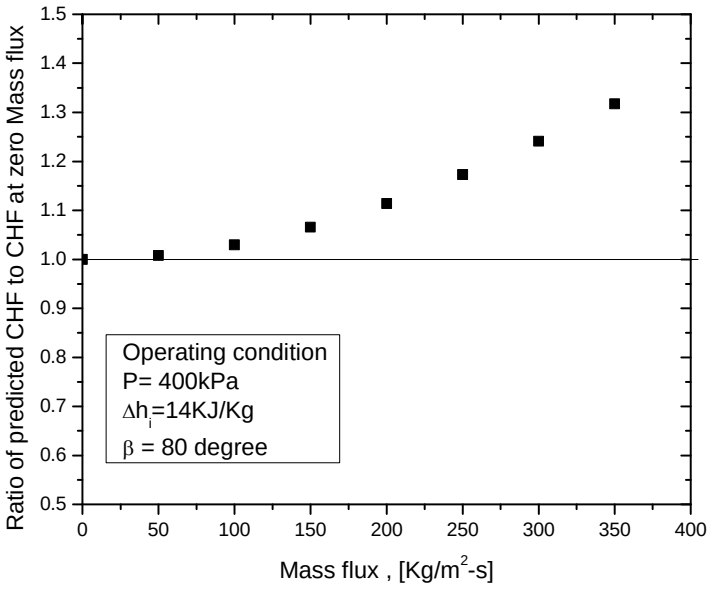


Figure 5.16 The ratio of predicted CHF with different mass flux to CHF value at zero mass flux.

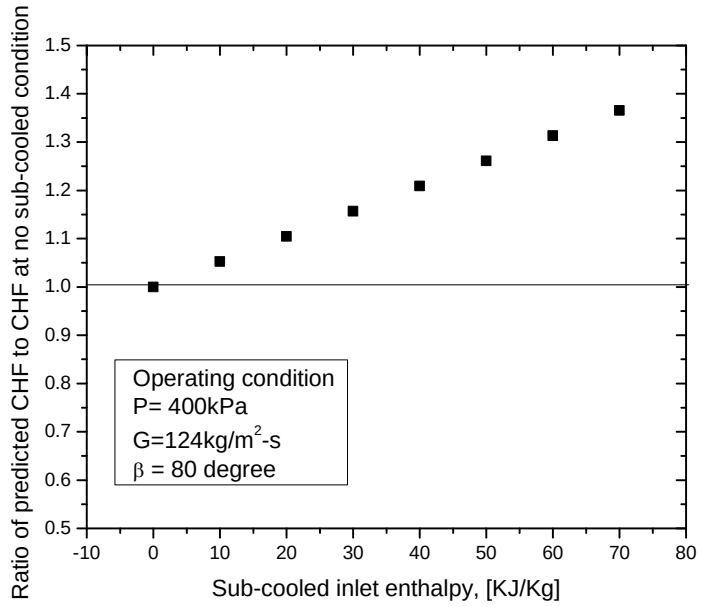


Figure 5.17 The ratio of predicted CHF with different sub-cooled level to CHF value at zero sub-

cooled enthalpy.

The effect of system pressure on CHF capturing by the proposed correlation shows interesting result. The CHF value increase as the system pressure increases till 0.2 reduced pressure (i.e., 8 bar in R-134a case), however as the reduced pressure (8~9 bar in R-134a case) reached to 0.22 the CHF prediction by correlation started to decrease (see fig. 5.18). It could concluded that the optimized system pressure can be determined in terms of maximized CHF value in fixed other operating parameters (i.e., mass flux and inlet sub-cooled enthalpy). This finding induced from the proposed correlation is consistent with the result from the CHF look-up table (see Chapter 4.1.3).

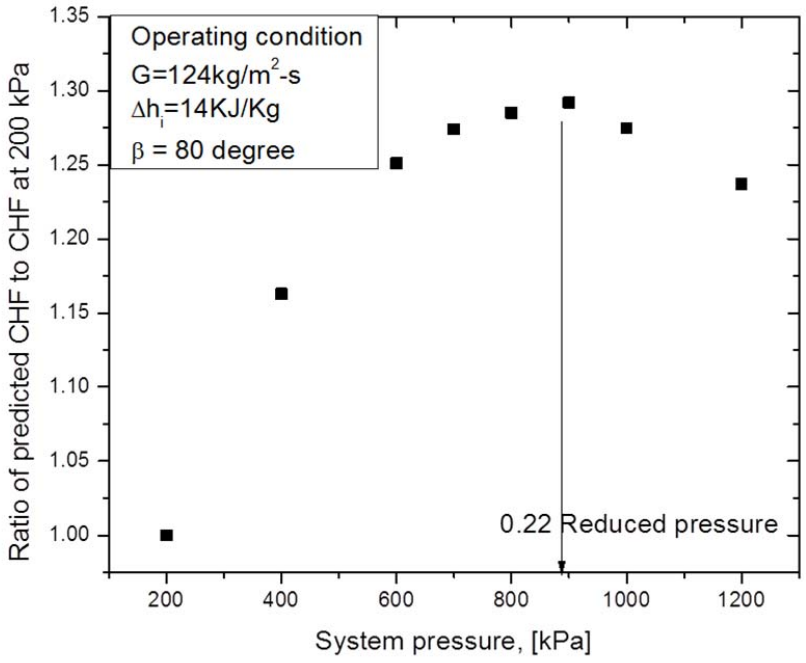


Figure 5.18 The ratio of predicted CHF with different pressure to CHF value at 200kPa.

Nomenclature

English Symbols

C	a constant value for author's correlation
D, D_b	Bubble departure diameter
D	channel diameter
F_S	Surface tension force
F_M	Force by evaporation
F_G	Gravity force
F_I	Inertial force
G	Mass flux [Kg/m^2]
g	Gravitation force (=9.81 m/s^2)
h_{fg}	Heat of vaporization (latent heat)
K	Non-dimensionless parameter in Katto correlation
L, L_h	Heated channel length
n	Non-dimensionless parameter in Bowring correlation
Min	Minimum value
Max	Maximum value
q''	Heat flux
$q''_{CHF,exp}$	Experimental measurement of critical heat flux
$q''_{CHF,pre}$	Prediction of critical heat flux
$q_{CHF,sat,}$	Critical Heat flux at saturation flow condition (q_{co})
$q_{CHF,sub}$	Critical Heat flux at sub-cooled flow condition
V	Bulk fluid vecity
W	Weber number $\left(\mathrm{We} = \frac{G^2 D}{\rho_f \sigma}\right)$

Greek Symbols

σ	Surface tension
β, θ	Static Contact angle at atmospheric pressure condition [°]
ρ_f, ρ_l	Density of fluid
ρ_g, ρ_v	Density of gas
Δh_{in}	Sub-cooled Inlet enthalpy [KJ/Kg]

γ^{sl}	Solid/liquid interfacial free energy
γ^{sv}	Solid surface free energy
γ^{lv}	Liquid surface free energy

Acronyms

AP-	Atmospheric Pressure-
CHF	Critical Heat Flux
M	Modeling fluid
MAD	Mean absolute deviation
P	Prototype fluid

References

Bang, I. C., Chang, S. H., 2004, "Visualization of the sub-cooled flow boiling of R-134a in a vertical rectangular channel with an electrically heated wall", Int. J. of Heat and Mass Transfer, Vol. 47, pp. 4349-4363

Bang, I. C., Chang, S. H., 2006, "Boiling Heat Transfer Performance and Phenomena of A120 3-Water Nano-fluids from a Plain Surface in a Pool", Int. J. of Heat and Mass Transfer, Vol. 48, pp. 2407-2419

Chang, Y. P., 1961, ‘‘An Analysis of the Critical Conditions and Burnout in Boiling Heat Transfer,’’ USAEC Rep. TID-14004, Washington, DC

Katto, Y., et al., “A new hydrodynamic model of critical heat flux, applicable widely to both pool and forced convection boiling on submerged bodies in saturated liquids”, Int. Journal of Heat and Mass Transfer Vol. 26, No. 6. 389-399, 1983

Kandlikar, Satish G. 2002, “A theoretical Model to predict pool boiling CHF incorporating effects of contact angle and orientation”, Journal of Heat Transfer, Vol. 123

Elkassabgi, Y., and Lienhard, J. H., 1988, ‘‘Influence of Subcooling on Burnout of Horizontal Cylindrical Heaters,’’ASME J. Heat Transfer, 110, pp. 479– 486.

Kutateladge, S. S., Leont’ev, A. I., “Turbulent boundary layers in compressible gases”, D.B. Spalding, trans., Academic press, New York, 1964

Bowring, R.W., 1972, “A simple but accurate round tube uniform heat flux, dry-out correlation over the pressure range, 0.7–12 MN/m2 (100–2500 psia)”, AEEW-R789, 1972.

Katto, Y., Ohno, H., “An improved version of the generalized correlation of critical heat flux for the forced convective boiling in uniformly heat vertical tube” Int. J. Heat Mass Transfer, Vol. 27 No 9. 1641-1648, 1984

Shah, M.M., 1987, “Improved general correlation for critical heat flux during upflow in uniformly heated vertical tubes”, Heat Fluid Flow 8 (4), 326–335

Weber, P., Johannsen, K., 1990. Study of critical heat flux condition at convective boiling of water: temperature and power controlled experiments. In: Proceedings of the Ninth International Heat Transfer Conference, 1-BO-11, Jerusalem, Israel, vol. 2, pp. 63–68

Chang, S.H., Baek, W.P., Bae, T.M., 1991. A study of critical heat flux for low flow of water in vertical round tubes under low pressure. Nucl. Eng. Des. 132, 225–237

Baek, W.P., Moon, S.K., Chang, S.H., 1995. A modified CHF correlation for low flow of water at low pressures. In: Proceedings of the First International Symposium on Two-Phase Flow Modeling and Experimentation, Rome, Italy, 9–11 October, pp. 853–858.

Groeneveld, D.C., Leung, L.K.H., Kirillov, P.L., Bobkov, V.P., Smogalev, I.P., Vinogradov, V.N., Huang, X.C., Royer, E., 1996. 'The 1995 look-up table for critical heat flux in tubes", Nucl. Eng. Des. 163, 1–23

Baek, W.P., Kim, H.G., Chang, S.H., 1997. "KAIST critical heat flux correlation for water flow in vertical round tubes", NUTHOS-5, Paper No. AA5

Kim, S.J., 2009 "Subcooled flow boiling heat transfer and critical heat flux in water-based nanofluids at low pressure" PhD Dissertation Thesis, MIT

Chang, J.Y., You, S.M., 2005, "Enhanced boiling heat transfer from micro-porous surfaces: effects of a coating composition and method", Int. J. Heat and Mass Transfer 40 (18) 4449–4466.

Kim, H., Kim, J., Kim, M., 2006, "Experimental study on CHF characteristics of water-TiO 2 nanofluids", Nuclear Engineering and Technology, Vol. 38, No. 1

Kim, H.D. 2011, "enhancement of critical heat flux in nucleate boiling of nanofluids: a state-of-art review", Nanoscale Research Letters, 6:415

Kim, S. J., Bang, I. C., Buongiorno, J., Hu, L. W., 2007, "Surface wettability change during pool boiling of nanofuids and its effect on critical heat flux", Int. J. of Heat and Mass Transfer, Vol. 50, pp. 4105-4116

Lee, K.L., 2008, "The characteristics and visualization of critical heat flux of R-134a flowing in a vertical annular geometry with spacer grids", International Journal of Heat and Mass Tansfer 51 (2008) 91-103

Van Der Molen S.B. and Galjee F.W.B.M, 1978, "The boiling mechanism during durnout phenomena in sub-cooled two-phase water flows" Proc. 6th Int. heat transfer conf., Toronto, Canada, August 7-11, 1978, Vol. !. pp. 381-385

Shenton, M.J., M.C. Lovell-Hoare, G.C. Stevens, J. Phys., D Appl. Phys. 34 (2001) 2754

Cheng, C.H., P. Liu, L. Xu , L.Y. Zhang, R.J. Zhan, W.R. Zhang, 2006, submitted to "Chinese Physics "

Borcia1, G., C.A. Anderson, N.M.D. Brown, 2003, Plasma Sources Sci. Technol. 12 (2003) 335

Tanaka, K., T. Inomata, M. Kogoma, 2001, Thin Solid Films 386 (2001) 217

6. Conclusions and Recommendations

The current research is designed to investigate the sub-cooled flow boiling Critical Heat Flux (CHF) in terms of (1) understanding of its mechanism, (2) development of predictive CHF correlation based on force balance approach, and (3) feasibility of enhancing CHF with surface medications using atmospheric pressure plasma. Chapter 1 gave an introduction and motivation of the current research. Chapter 2 and 3 looked into the mechanism of CHF from literature review and experimental setting for measurement and visualization for CHF. Chapter 4 showed the CHF experimental results under the sub-cooled flow boiling conditions and fluid-to-fluid scaling model to compare with water CHF data. Chapter 5 proposes a novel analytical CHF correlation using force balance including surface wettability concept under the flow boiling condition. Furthermore the validation of proposed correlation with current R-134a flow boiling CHF data and other literature CHF data in various operating condition are performed, and the validation work with surface treated condition CHF data is also conducted. Subsequently, under the sub-cooled flow boiling in R-134a, CHF measurement in various conditions was performed to investigate above three aspects (understanding of CHF, predicting of CHF, enhancing the CHF) with macroscopic operating key parameters effect and microscopic surface feature effect. Conclusions and author's recommendations for the future work are presented in following chapter.

6.1 Conclusions

In this study, a total of 36 CHF data with R-134a flow boiling condition were measured for low pressure (less than 0.2 reduced pressure) and following conditions (D=12.7 mm , Rectangular channel with bottom side only heating, P=400~800 kPa, G=124~248 kg/m2-s , H_{in} = 9~45 kJ/kg , q_{CHF} = 411~713 kW/m^2) to investigate CHF behavior. In addition a CHF prediction correlation is proposed incorporating bubble force balance in flow boiling condition. From the analysis of parametric trends and assessments of current prediction model, the following conclusions can be made:

1. The observed parametric trends of CHF data based on fixed inlet condition agree with those in the previous studies. For low pressure (less than 0.2 reduced pressure, in case of R-134a, it ranges from 1 bar to 8bar) the CHF increases with increase in pressure. A same trend is also found in water CHF data in look-up table (see Chapter 4.1.3).

2. Fluid-to-fluid scaling method of Katto (1978) was utilized to convert the CHF data of R-134a into the equivalent CHF data of water. Then the equivalent CHF data is compared with water CHF look-up table data. The comparison study showed good agreement with less than 25% of deviation (see Chapter 4.2.1).

3. We propose a predictive CHF correlation with bubble force balance in flow boiling condition. Correlation accuracy was validated with current experimental condition with R-134a and other CHF data in literature. It shows very good agreement with a

maximum deviation of 8% from the current 35 CHF value and a maximum deviation of 38% from other 105 CHF value under the different operating condition (see Chapter 5.2).

4. Comparative study between current correlation and Katto's correlation was conducted with R-134a flow boiling test result. Katto's correlation predicted with 8% of mean absolute deviation (MAD) to current experimental CHF data. However, current correlation shows 1.7% mean absolute deviation (MAD) in present experimental condition (see Chapter 5.2).

5. In this study, AP-Plasma technique was applied to modify the heating surface of copper. The surface feature of treated heater was identified by reduction of static contact angle (82 degree to 15 degree) and coating layer thickness measurement (1 micron ~ 3 micron) (see Chapter 5.3.1).

6. The enhancement of CHF with reduction of static contact angle is observed in experimental results. It is found that the CHF value is improved 10~18% by changing surface wettability with AP-Plasma treated heating surface compared to the reference untreated heating surface (see Chapter 5.3.3).

7. In addition, this correlation inherently captures the effect of surface wettability by implementing contact angle in correlation. Thus, CHF correlation analytically demonstrates that CHF is increased as the contact angle is decreased (i.e., the

reduction of contact angle (80 degree to 10 degree) leads to 27% of CHF enhancement, see Chapter 5.3.3).

6.2 Recommendations for Future Work

Although the current study has examined several fundamental parametric effects (i.e., pressure, mass flux and inlet sub-cooled enthalpy) and conditions of surface treatment under sub-cooled flow boiling regarding the enhancement of CHF, there are several recommendations for future works in the following potential research field as summarized below.

First, proposed author's CHF correlation is only applicable when the surface treatment is not producing certain thickness of oxidation layer (50~200 micron) in which there is no wick boiling taking place. However, many of industry vendors are highly interested in the effect of wick boiling or heat transfer under the well-built CRUD condition on CHF or heat transfer coefficient. Future research should aim to correlate the CHF under wick boiling condition (see Figure 6.1).

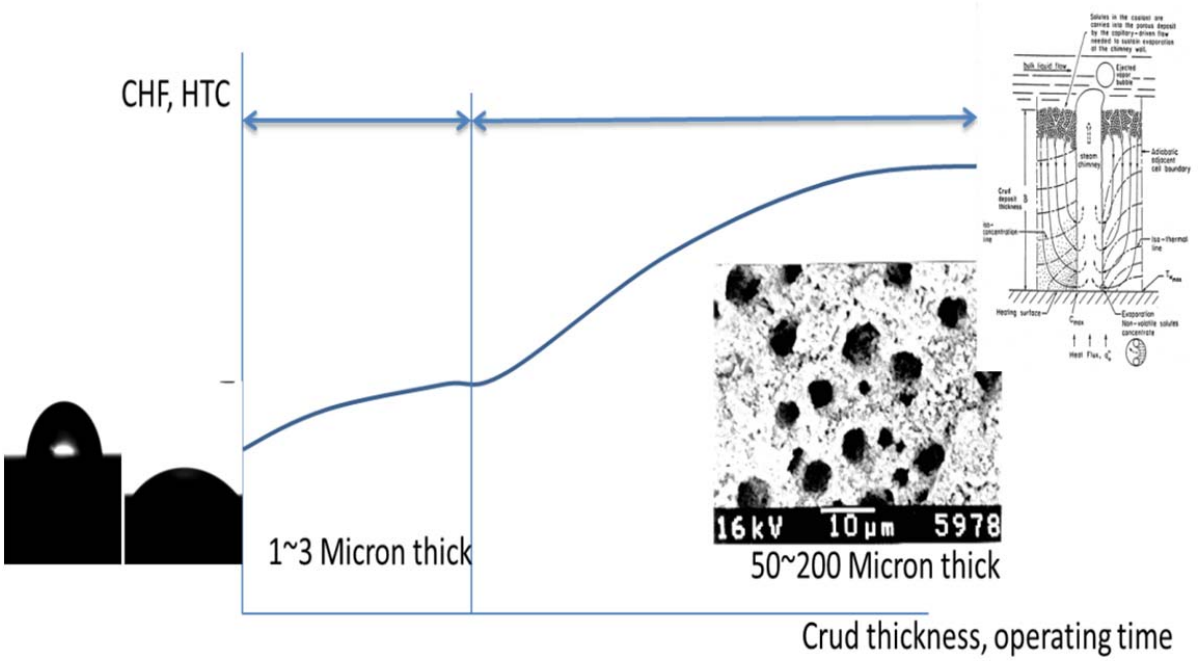


Figure 6.1 A conceptual diagram of surface wettability effect on CHF and CRUD induced wick boiling effect on CHF

Second, we have found confidence that there is significant room for improvement of most two-phase heat-transfer phenomena, especially with regard to AP-Plasma induced hydrophilic surface effect. A further exploitation of engineered hydrophilic surface treatment using AP-plasma or nano-porous structure deposition technique for striking enhancements of CHF in nuclear reactors is highly recommended for future research (see fig 6.2).

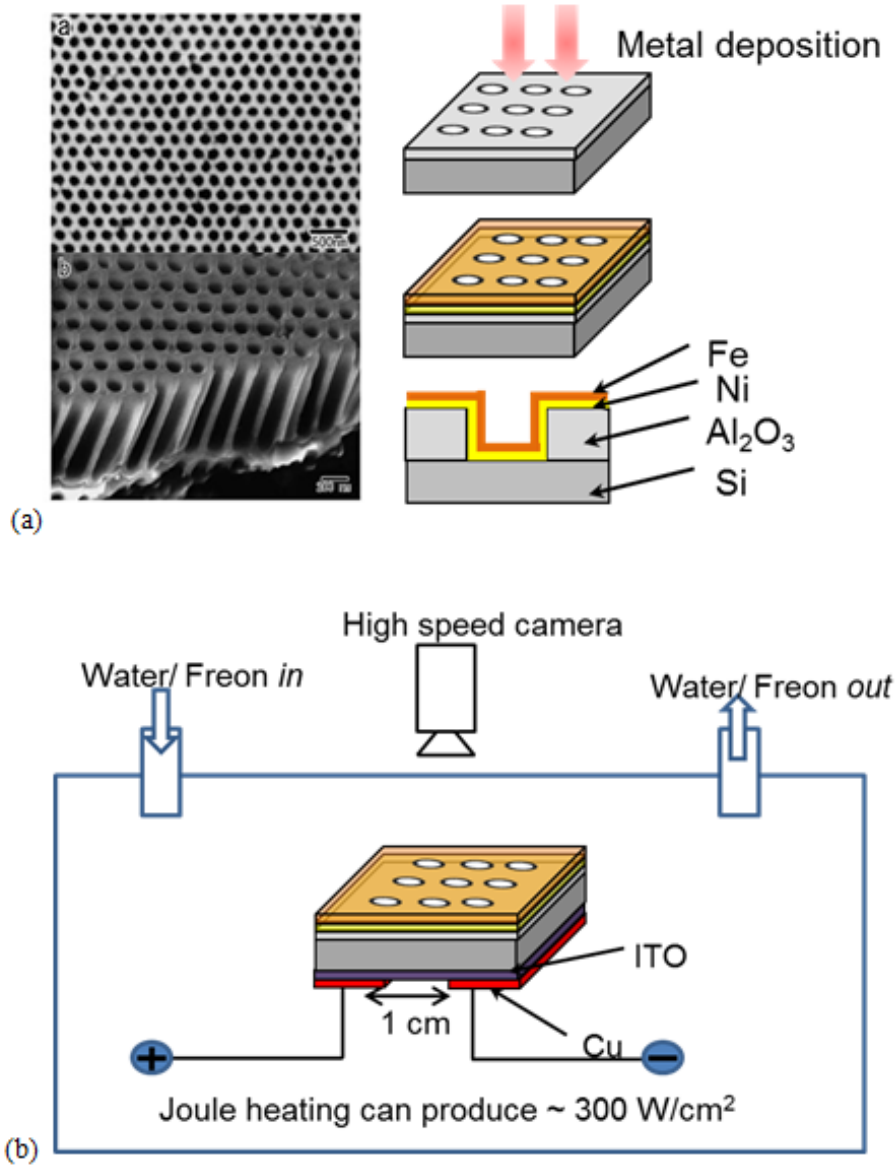


Figure 6.2 (a) SEM image of nano-porous structure and fabrication process, (b) schematic of flow boiling test

Third, current research was limited in operating pressure condition (less than 0.2 reduced pressures) due to visualization purpose and other application. However, it will be very practical to investigate CHF behavior in the high-pressure condition (such as higher than 0.2 reduced pressure, which is much closer to the boiling water reactor operating condition (70 bar, ~0.3 reduced pressure range). This future research would provide the complete system pressure effect on CHF and could suggest an optimal pressure condition for best CHF performance perspective (see fig. 6.3).

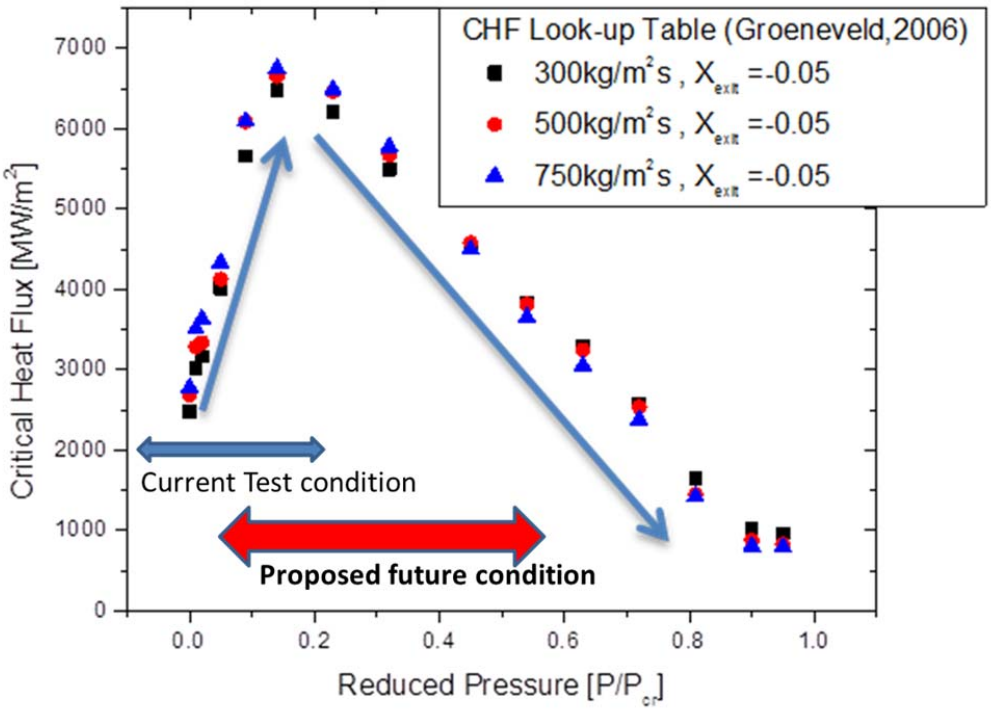


Figure 6.3 The proposed future research pressure condition range (reduced pressure: 0.1 ~ 0.5).

Fourth, proposed correlation shows quite good validation accuracy under current experimental condition and literature CHF data, however. However, it is worthwhile to perform the validation work of proposed CHF correlation with, mostly used in industry with high accuracy, CHF look-up table (about more than 30,000 CHF data) in order to achieve reasonable accuracy over the entire operating condition of boiling heat transfer system. Furthermore, Due to lack of CHF literature data with static contact angle measurement, it is required to investigate more CHF data with various operating conditions including difference surface wettability (i.e. static contact angle). Therefore, the additional validation of proposed correlation for expanded experimental condition including contact angle measurement is also needed in future study. Eventually, this will provide more confidence on author's proposed correlation and also will be applicable for wider operating ranges with practical approach.

APPENDIX A

In experimental measurement, The CHF value is measured with following operating parameter (P, G, Δh_i) condition, the proposed analytic CHF prediction correlation is consisted with following parameter (P, G, Δh_i, and β). The correlation is follows as below, and detail information is reported in following table

$$q''_{CHF,subcooled} = Ch_{fg}\sqrt{\frac{\sigma\rho_g(1+cos\beta)}{D}+\frac{\rho_f\rho_g gD(1+cos\beta)}{2}+\frac{\rho_g G^2}{\rho_f}}\left(1+\frac{\Delta h_i}{h_{fg}}\right)$$

In this present study, 6 group's CHF measurement data sets are reviewed and predicted with proposed author's correlation over the various operating conditions. It is assumed that the contact angle for this validation is 80˚ as reference value due to lack of contact angle measurement. In current test of CHF data (A.1), the contact angle for water drop on copper surface is measured as 80˚ without any surface treatment. The CHF data in flow boiling condition of A.6 also includes the contact angle measurement.

A.1 Present CHF data (experimental Measurement, analytical prediction)

# of	Pressure	Mass flux	enthalpy	Measure CHF	Predicted CHF	Deviation %	Hfg	lo, g	lo,f	cos(beta)	surf. Tension	first term	second term	third term	C value
	Kpa	Kg/m2-s	KJ/Kg	W/m2	W/m2	7.68%	KJ/Kg	kg/m3	kg/m3	80	N/m				0.0396
1	400	124	14.79	462951	432,424	-6.59%	191.6	19.5	1270	0.174	0.01010	2546	11.02	236	0.0424
2	400	248	14.54	509282	483,561	-5.05%	191.6	19.5	1270	0.174	0.01010	2546	11.02	944	0.0418
3	400	248	13.95	498970	482,191	-3.36%	191.6	19.5	1270	0.174	0.01010	2546	11.02	944	0.0410
4	400	248	12.76	501252	479,389	-4.36%	191.6	19.5	1270	0.174	0.01010	2546	11.02	944	0.0415
5	400	248	9.42	491620	471,573	-4.08%	191.6	19.5	1270	0.174	0.01010	2546	11.02	944	0.0413
6	500	124	22.93	495425	476,982	-3.72%	185.97	24.3	1240.8	0.174	0.00930	3003	13.05	301	0.0412
7	500	186	23.20	525567	503,967	-4.11%	185.97	24.3	1240.8	0.174	0.00930	3003	13.05	678	0.0413
8	500	248	22.02	544685	535,662	-1.66%	185.97	24.3	1240.8	0.174	0.00930	3003	13.05	1205	0.0403
9	500	186	21.02	513183	498,701	-2.82%	185.97	24.3	1240.8	0.174	0.00930	3003	13.05	678	0.0408
10	500	186	13.94	505413	481,637	-4.70%	185.97	24.3	1240.8	0.174	0.00930	3003	13.05	678	0.0416
11	600	124	30.67	510625	517,547	1.36%	180.89	29.54	1210	0.174	0.00840	3418	14.92	375	0.0391
12	600	186	30.51	548506	548,085	-0.08%	180.89	29.54	1210	0.174	0.00840	3418	14.92	845	0.0397
13	600	248	28.35	579069	582,660	0.62%	180.89	29.54	1210	0.174	0.00840	3418	14.92	1502	0.0394
14	600	186	28.13	535199	541,925	1.26%	180.89	29.54	1210	0.174	0.00840	3418	14.92	845	0.0392
15	600	186	22.02	533354	526,084	-1.36%	180.89	29.54	1210	0.174	0.00840	3418	14.92	845	0.0402
16	700	124	35.87	546207	548,807	0.48%	176.21	34.35	1199	0.174	0.00780	3804	16.68	441	0.0395
17	700	186	36.49	584638	584,898	0.04%	176.21	34.35	1199	0.174	0.00780	3804	16.68	991	0.0396
18	700	248	35.88	616157	628,212	1.96%	176.21	34.35	1199	0.174	0.00780	3804	16.68	1762	0.0389
19	700	186	35.89	583294	583,264	-0.01%	176.21	34.35	1199	0.174	0.00780	3804	16.68	991	0.0396
20	700	186	29.14	561116	564,690	0.64%	176.21	34.35	1199	0.174	0.00780	3804	16.68	991	0.0394
21	800	186	43.70	617047	621,919	0.79%	171.81	39.22	1181.6	0.174	0.00720	4133	18.21	1148	0.0393
22	800	186	38.68	602688	607,450	0.79%	171.81	39.22	1181.6	0.174	0.00720	4133	18.21	1148	0.0393
23	400	124	17.00	454938	437,069	-3.93%	191.6	19.5	1270	0.174	0.01010	2546	11.02	236	0.0413
24	400	186	15.53	465120	456,331	-1.89%	191.6	19.5	1270	0.174	0.01010	2546	11.02	531	0.0404
25	500	124	26.31	481098	484,683	0.75%	185.97	24.3	1240.8	0.174	0.00930	3003	13.05	301	0.0394
26	500	186	25.01	501414	508,323	1.38%	185.97	24.3	1240.8	0.174	0.00930	3003	13.05	678	0.0391
27	500	186	21.59	491944	500,067	1.65%	185.97	24.3	1240.8	0.174	0.00930	3003	13.05	678	0.0390
28	500	186	16.50	478443	487,813	1.96%	185.97	24.3	1240.8	0.174	0.00930	3003	13.05	678	0.0389
29	500	186	24.38	494291	506,795	2.53%	185.97	24.3	1240.8	0.174	0.00930	3003	13.05	678	0.0387
30	500	248	24.57	519917	542,229	4.29%	185.97	24.3	1240.8	0.174	0.00930	3003	13.05	1205	0.0380
31	600	124	32.38	505704	521,732	3.17%	180.89	29.54	1210	0.174	0.00840	3418	14.92	375	0.0384
32	600	186	30.90	530666	549,106	3.47%	180.89	29.54	1210	0.174	0.00840	3418	14.92	845	0.0383
33	600	248	28.54	544329	583,189	7.14%	180.89	29.54	1210	0.174	0.00840	3418	14.92	1502	0.0370
34	700	124	38.84	525858	556,498	5.83%	176.21	34.35	1199	0.174	0.00780	3804	16.68	441	0.0375
35	700	186	36.31	560809	584,416	4.21%	176.21	34.35	1199	0.174	0.00780	3804	16.68	991	0.0380
36	700	248	37.24	587179	632,253	7.68%	176.21	34.35	1199	0.174	0.00780	3804	16.68	1762	0.0368

A.2 CHF data by Lee et al. (2008)

# of	Pressure	Mass flux	enthalpy	Measure CHF	Predicted CHF	Deviation %	Hfg	lo, g	lo,f	cos(beta)	surf. Tension	first term	second term	third term	C value
	Kpa	Kg/m2-s	KJ/Kg	W/m2	W/m2	37.16%	KJ/Kg	kg/m3	kg/m3	80	N/m				0.0093
1	1160	100	20.51	76230	82,512	8.24%	157.95	57.126	1126.5	0.174	0.00554	5110	22.93	507	0.0057
2	1160	222	27.68	84660	99,840	17.93%	157.95	57.126	1126.5	0.174	0.00554	5110	22.93	2499	0.0052
3	1160	300	38.39	144470	119,031	-17.61%	157.95	57.126	1126.5	0.174	0.00554	5110	22.93	4564	0.0075
4	1160	300	21.66	123620	108,888	-11.92%	157.95	57.126	1126.5	0.174	0.00554	5110	22.93	4564	0.0070
5	1160	403	32.25	151610	135,392	-10.70%	157.95	57.126	1126.5	0.174	0.00554	5110	22.93	8236	0.0069
6	1160	450	19.55	137060	135,619	-1.05%	157.95	57.126	1126.5	0.174	0.00554	5110	22.93	10269	0.0062
7	1160	556	11.41	135440	150,410	11.05%	157.95	57.126	1126.5	0.174	0.00554	5110	22.93	15677	0.0055
8	1160	600	21.27	158030	168,743	6.78%	157.95	57.126	1126.5	0.174	0.00554	5110	22.93	18256	0.0058
9	1160	700	32.77	196220	203,309	3.61%	157.95	57.126	1126.5	0.174	0.00554	5110	22.93	24848	0.0059
10	1300	185	20.54	104780	91,128	-13.03%	152.46	65.29	1104.9	0.174	0.00465	5274	23.88	2022	0.0071
11	1300	255	21.06	115340	102,134	-11.45%	152.46	65.29	1104.9	0.174	0.00465	5274	23.88	3842	0.0070
12	1300	300	20.59	120220	109,773	-8.69%	152.46	65.29	1104.9	0.174	0.00465	5274	23.88	5318	0.0067
13	1300	381	22.53	133050	126,905	-4.62%	152.46	65.29	1104.9	0.174	0.00465	5274	23.88	8578	0.0065
14	1600	250	37.14	127510	116,932	-8.30%	141.93	82.53	1063.8	0.174	0.00450	6372	29.43	4849	0.0067
15	1600	300	43.97	137450	132,403	-3.67%	141.93	82.53	1063.8	0.174	0.00450	6372	29.43	6982	0.0064
16	1600	397	38.02	154580	151,208	-2.18%	141.93	82.53	1063.8	0.174	0.00450	6372	29.43	12227	0.0063
17	1600	450	36.66	161960	163,492	0.95%	141.93	82.53	1063.8	0.174	0.00450	6372	29.43	15710	0.0061
18	1600	534	36.31	173170	185,328	7.02%	141.93	82.53	1063.8	0.174	0.00450	6372	29.43	22122	0.0058
19	1600	600	49.23	211030	218,056	3.33%	141.93	82.53	1063.8	0.174	0.00450	6372	29.43	27929	0.0060
20	2000	259	21.57	100260	107,522	7.24%	128.26	107.76	1011.4	0.174	0.00290	6409	30.56	7148	0.0057
21	2000	300	66.34	158030	151,681	-4.02%	128.26	107.76	1011.4	0.174	0.00290	6409	30.56	9590	0.0064
22	2000	365	25.37	116440	135,866	16.68%	128.26	107.76	1011.4	0.174	0.00290	6409	30.56	14195	0.0053
23	2000	468	24.67	131810	162,467	23.26%	128.26	107.76	1011.4	0.174	0.00290	6409	30.56	23337	0.0050
24	2000	569	61.47	224340	236,334	5.35%	128.26	107.76	1011.4	0.174	0.00290	6409	30.56	34497	0.0058
25	2000	600	55.81	213070	239,853	12.57%	128.26	107.76	1011.4	0.174	0.00290	6409	30.56	38358	0.0055

A.3 CHF data by Bang et al. (2002)

# of	Pressure	Mass flux	enthalpy	Measure CHF	Predicted CHF	Deviation %	Hfg	lo, g	lo,f	cos(beta)	surf. Tension	first term	second term	third term	C value
	Kpa	Kg/m2-s	KJ/Kg	W/m2	W/m2	76.72%	KJ/Kg	kg/m3	kg/m3	80	N/m				0.0386
1	700	1000	26.19	875000	696,487	-20.40%	176.21	34.05	1200.2	0.174	0.00765	3737	16.38	28370	0.0241
2	700	190	26.19	411000	268,589	-34.65%	176.21	34.05	1200.2	0.174	0.00765	3737	16.38	1024	0.0294
3	700	1000	28.89	941000	705,778	-25.00%	176.21	34.05	1200.2	0.174	0.00765	3737	16.38	28370	0.0256
4	700	2000	28.89	983000	1,348,297	37.16%	176.21	34.05	1200.2	0.174	0.00765	3737	16.38	113481	0.0140
5	700	2000	17.9	955000	1,276,050	33.62%	176.21	34.05	1200.2	0.174	0.00765	3737	16.38	113481	0.0144
6	1450	1000	43.04	830000	991,805	19.49%	147.14	73.715	1084	0.174	0.00446	5751	26.29	68003	0.0161
7	1450	2000	43.04	1089000	1,924,485	76.72%	147.14	73.715	1084	0.174	0.00446	5751	26.29	272011	0.0109

A.4 CHF data by Van der Mollen et al. (1978)

# of	Pressure	Mass flux	enthalpy	Measure CHF	Predicted CHF	Deviation %	Hfg	lo, g	lo,f	cos(beta)	surf. Tension	first term	second term	third term	C value
	Kpa	Kg/m2-s	KJ/Kg	W/m2	W/m2	48.57%	KJ/Kg	kg/m3	kg/m3	80	N/m				0.0438
1	100	1000	131.50	2500000	2,952,134	18.09%	2257.44	0.59	956.6	0.174	0.05899	163	0.69	617	0.0375
2	100	1000	249.50	4000000	3,097,953	-22.55%	2257.44	0.59	956.6	0.174	0.05899	163	0.69	617	0.0571
4	100	2500	126.50	4500000	6,685,455	48.57%	2257.44	0.59	956.6	0.174	0.05899	163	0.69	3855	0.0298
5	100	1000	82.50	2500000	2,891,582	15.66%	2257.44	0.59	956.6	0.174	0.05899	163	0.69	617	0.0382
6	100	1000	157.50	4500000	2,984,264	-33.68%	2257.44	0.59	956.6	0.174	0.05899	163	0.69	617	0.0667
8	100	2500	84.50	4500000	5,111,001	13.58%	2257.44	0.59	956.6	0.174	0.05899	163	0.69	3855	0.0303
9	100	1000	73.50	2500000	2,880,461	15.22%	2257.44	0.59	956.6	0.174	0.05899	163	0.69	617	0.0384
10	100	1000	141.50	4500000	5,124,741	13.88%	2257.44	0.59	956.6	0.174	0.05899	163	0.69	617	0.0672
12	100	2500	87.50	4500000	4,812,111	6.94%	2257.44	0.59	956.6	0.174	0.05899	163	0.69	3855	0.0303
13	100	1000	77.50	2500000	2,885,404	15.42%	2257.44	0.59	956.6	0.174	0.05899	163	0.69	617	0.0383
14	100	1000	149.50	4500000	2,974,378	-33.90%	2257.44	0.59	956.6	0.174	0.05899	163	0.69	617	0.0669
16	100	2500	96.50	4500000	4,995,121	11.00%	2257.44	0.59	956.6	0.174	0.05899	163	0.69	3855	0.0302

A.5 CHF data by Kim et al. (2009)

# of	Pressure	Mass flux	enthalpy	Measure CHF	Predicted CHF	Deviation %	Hfg	lo, g	lo,f	cos(beta)	surf. Tension	first term	second term	third term	C value
	Kpa	Kg/m2-s	KJ/Kg	W/m2	W/m2	29.75%	KJ/Kg	kg/m3	kg/m3	80	N/m				0.0464
1	100	1538.7	87.50	4951000	4,005,781	-19.09%	2257.44	0.59	956.6	0.174	0.05899	163	0.69	1460	0.0524
2	100	1535.2	91.00	4853000	4,003,554	-17.50%	2257.44	0.59	956.6	0.174	0.05899	163	0.69	1454	0.0514
3	100	1510.4	92.50	4863000	3,947,986	-18.82%	2257.44	0.59	956.6	0.174	0.05899	163	0.69	1407	0.0522
4	100	2012.5	109.50	5422000	5,176,629	-4.53%	2257.44	0.59	956.6	0.174	0.05899	163	0.69	2498	0.0444
5	100	2011.1	102.50	5448000	5,157,949	-5.32%	2257.44	0.59	956.6	0.174	0.05899	163	0.69	2495	0.0448
6	100	1987.1	26.50	4552000	4,935,955	8.43%	2257.44	0.59	956.6	0.174	0.05899	163	0.69	2435	0.0391
7	100	2007.4	124.50	5306000	5,197,045	-2.05%	2257.44	0.59	956.6	0.174	0.05899	163	0.69	2485	0.0433
8	100	2502.3	137.50	5851000	6,441,627	10.09%	2257.44	0.59	956.6	0.174	0.05899	163	0.69	3862	0.0385
9	100	2505.6	141.50	5099000	6,460,550	26.70%	2257.44	0.59	956.6	0.174	0.05899	163	0.69	3872	0.0335
10	100	2512.6	115.50	6459000	6,407,661	-0.79%	2257.44	0.59	956.6	0.174	0.05899	163	0.69	3894	0.0427
11	100	2483.4	22.50	4852000	6,087,884	25.47%	2257.44	0.59	956.6	0.174	0.05899	163	0.69	3804	0.0338
12	100	2545.9	177.50	5132000	6,658,732	29.75%	2257.44	0.59	956.6	0.174	0.05899	163	0.69	3998	0.0327

A.6 CHF data by Kim et al. (2010)

# of	Pressure	Mass flux	enthalpy	Measure CHF	Predicted CHF	Deviation %	Hfg	lo, g	lo,f	cos(beta)	surf. Tension	first term	second term	third term	C value
	Kpa	Kg/m2-s	KJ/Kg	W/m2	W/m2	10.96%	KJ/Kg	kg/m3	kg/m3	80	N/m				0.0489
1	100	1538	87.50	4702000	4,615,986	-1.83%	2257.44	0.59	956.6	0.174	0.05899	163	0.69	1459	0.0498
2	100	1519	122.50	4411000	4,632,871	5.03%	2257.44	0.59	956.6	0.174	0.05899	163	0.69	1423	0.0465
3	100	2496	110.50	6858000	7,422,392	8.23%	2257.44	0.59	956.6	0.951	0.05899	271	0.69	3842	0.0452
4	100	2496	122.50	6723000	7,460,007	10.96%	2257.44	0.59	956.6	0.951	0.05899	271	0.69	3842	0.0440
5	100	2024	103.50	6045000	6,000,149	-0.74%	2257.44	0.59	956.6	0.276	0.05899	177	0.69	2527	0.0492
6	100	2010	106.50	6126000	5,968,955	-2.56%	2257.44	0.59	956.6	0.276	0.05899	177	0.69	2492	0.0502
7	100	1554	97.50	4801000	4,662,049	-2.89%	2257.44	0.59	956.6	0.087	0.05899	151	0.69	1489	0.0503
8	100	1540	89.50	4945000	4,608,234	-6.81%	2257.44	0.59	956.6	0.087	0.05899	151	0.69	1463	0.0524
9	100	2002	97.50	5888000	5,916,277	0.48%	2257.44	0.59	956.6	0.225	0.05899	170	0.69	2472	0.0486
10	100	2020	100.50	6214000	5,973,651	-3.87%	2257.44	0.59	956.6	0.225	0.05899	170	0.69	2517	0.0508
11	100	2517	91.50	7068000	7,408,017	4.81%	2257.44	0.59	956.6	0.848	0.05899	256	0.69	3907	0.0466
12	100	2502	91.50	7095000	7,366,602	3.83%	2257.44	0.59	956.6	0.848	0.05899	256	0.69	3861	0.0471
13	100	2493	82.50	7364000	7,325,706	-0.52%	2257.44	0.59	956.6	0.946	0.05899	270	0.69	3833	0.0491
14	100	2505	68.50	7313000	7,314,621	0.02%	2257.44	0.59	956.6	0.946	0.05899	270	0.69	3870	0.0489
15	100	2001	78.50	6184000	5,967,544	-3.50%	2257.44	0.59	956.6	0.891	0.05899	262	0.69	2470	0.0506
16	100	1998	74.50	6041000	5,949,254	-1.52%	2257.44	0.59	956.6	0.891	0.05899	262	0.69	2462	0.0496
17	100	2003	84.50	5547000	5,988,276	7.96%	2257.44	0.59	956.6	0.891	0.05899	262	0.69	2474	0.0453
18	100	2000	105.50	5781000	6,033,793	4.37%	2257.44	0.59	956.6	0.891	0.05899	262	0.69	2467	0.0468
19	100	1521	77.50	4829000	4,543,795	-5.91%	2257.44	0.59	956.6	0.139	0.05899	158	0.69	1427	0.0519
20	100	1521	74.50	5041000	4,537,957	-9.98%	2257.44	0.59	956.6	0.139	0.05899	158	0.69	1427	0.0543

APPENDIX B

The effect of several operating parameter on enhancement of CHF is demonstrated by using author's proposed correlation. The detail parameter and CHF prediction are tabulated in following table (B.1, B.2, B.3, and B.4)

B.1 27% of CHF enhancement (80˚→10 ˚ reduction of contact angle): 4bar, 124kg/m^2-s, 14.79 KJ/kg

# of	Pressure, Kpa	Mass flux, Kg/m2-s	sub-cooled enthalpy, KJ/Kg	**contact angle**	**Ratio**	**Predicted CHF, W/m2**	Hfg, KJ/Kg	lo,g	lo,f	cos(beta)	surf. Tension, N/m
1	400	124	14.79	**80**	**100.00%**	10907871	191.6	19.5	1270	0.174	0.01010
2	400	124	14.79	**70**	**106.34%**	11599172	191.6	19.5	1270	0.342	0.01010
3	400	124	14.79	**60**	**111.96%**	12212272	191.6	19.5	1270	0.500	0.01010
4	400	124	14.79	**50**	**116.81%**	12741056	191.6	19.5	1270	0.643	0.01010
5	400	124	14.79	**40**	**120.83%**	13180462	191.6	19.5	1270	0.766	0.01010
6	400	124	14.79	**30**	**124.01%**	13526410	191.6	19.5	1270	0.866	0.01010
7	400	124	14.79	**20**	**126.29%**	13775750	191.6	19.5	1270	0.940	0.01010
8	400	124	14.79	**10**	**127.67%**	13926247	191.6	19.5	1270	0.985	0.01010

B.2 22% of CHF enhancement (80 ˚ →10 ˚ reduction of contact angle): 4bar, 248kg/m^2-s, 9.42 KJ/kg

# of	Pressure, Kpa	Mass flux, Kg/m2-s	sub-cooled enthalpy, KJ/Kg	**contact angle**	**Ratio**	**Predicted CHF, W/m2**	Hfg, KJ/Kg	lo,g	lo,f	cos(beta)	surf. Tension, N/m
1	400	248	9.42	**80**	**100.00%**	11895394	191.6	19.5	1270	0.174	0.01010
2	400	248	9.42	**70**	**105.09%**	12500459	191.6	19.5	1270	0.342	0.01010
3	400	248	9.42	**60**	**109.64%**	13042679	191.6	19.5	1270	0.500	0.01010
4	400	248	9.42	**50**	**113.61%**	13514052	191.6	19.5	1270	0.643	0.01010
5	400	248	9.42	**40**	**116.92%**	13908108	191.6	19.5	1270	0.766	0.01010
6	400	248	9.42	**30**	**119.54%**	14219731	191.6	19.5	1270	0.866	0.01010
7	400	248	9.42	**20**	**121.43%**	14445037	191.6	19.5	1270	0.940	0.01010
8	400	248	9.42	**10**	**122.58%**	14581300	191.6	19.5	1270	0.985	0.01010

B.3 29% of CHF enhancement (80 ˚ →10 ˚ reduction of contact angle): 4bar, 0kg/m^2-s, 14.79 KJ/kg

# of	Pressure, Kpa	Mass flux, Kg/m2-s	sub-cooled enthalpy, KJ/Kg	**contact angle**	**Ratio**	**Predicted CHF, W/m2**	Hfg, KJ/Kg	lo,g	lo,f	cos(beta)	surf. Tension, N/m
1	400	0	14.79	**80**	**100.00%**	10436728	191.6	19.5	1270	0.174	0.01010
2	400	0	14.79	**70**	**106.90%**	11157260	191.6	19.5	1270	0.342	0.01010
3	400	0	14.79	**60**	**113.00%**	11793356	191.6	19.5	1270	0.500	0.01010
4	400	0	14.79	**50**	**118.24%**	12340104	191.6	19.5	1270	0.643	0.01010
5	400	0	14.79	**40**	**122.58%**	12793289	191.6	19.5	1270	0.766	0.01010
6	400	0	14.79	**30**	**125.99%**	13149427	191.6	19.5	1270	0.866	0.01010
7	400	0	14.79	**20**	**128.45%**	13405781	191.6	19.5	1270	0.940	0.01010
8	400	0	14.79	**10**	**129.93%**	13560384	191.6	19.5	1270	0.985	0.01010

B.4 4.8% of CHF enhancement (80 ˚ →10 ˚ reduction of contact angle): 4bar, 1000kg/m^2-s, 14.79 KJ/kg

# of	Pressure, Kpa	Mass flux, Kg/m2-s	sub-cooled enthalpy, KJ/Kg	**contact angle**	**Ratio**	**Predicted CHF, W/m2**	Hfg, KJ/Kg	lo,g	lo,f	cos(beta)	surf. Tension, N/m
1	400	1000	14.79	**80**	**100.00%**	27621615	191.6	19.5	1270	0.174	0.01010
2	400	1000	14.79	**70**	**101.01%**	27901842	191.6	19.5	1270	0.342	0.01010
3	400	1000	14.79	**60**	**101.96%**	28162237	191.6	19.5	1270	0.500	0.01010
4	400	1000	14.79	**50**	**102.80%**	28395537	191.6	19.5	1270	0.643	0.01010
5	400	1000	14.79	**40**	**103.53%**	28595394	191.6	19.5	1270	0.766	0.01010
6	400	1000	14.79	**30**	**104.11%**	28756491	191.6	19.5	1270	0.866	0.01010
7	400	1000	14.79	**20**	**104.54%**	28874613	191.6	19.5	1270	0.940	0.01010
8	400	1000	14.79	**10**	**104.80%**	28946716	191.6	19.5	1270	0.985	0.01010

B.5 Mass flux effect on CHF (0 kg/m^2-s → 350 kg/m^2-s): 4bar, 14.79 KJ/kg, 80 ˚ of contact angle

# of	Pressure, Kpa	Mass flux, Kg/m2-s	sub-cooled enthalpy, KJ/Kg	contact angle	Ratio	Predicted CHF, W/m2	Hfg, KJ/Kg	lo,g	lo,f	cos(beta)	surf. Tension, N/m
1	400	0	14.79	80	100.00%	10438286	191.6	19.5	1270	0.174	0.01010
2	400	50	14.79	80	100.75%	10516315	191.6	19.5	1270	0.174	0.01010
3	400	100	14.79	80	102.96%	10747004	191.6	19.5	1270	0.174	0.01010
4	400	150	14.79	80	106.54%	11120857	191.6	19.5	1270	0.174	0.01010
5	400	200	14.79	80	111.36%	11624068	191.6	19.5	1270	0.174	0.01010
6	400	250	14.79	80	117.27%	12240694	191.6	19.5	1270	0.174	0.01010
7	400	300	14.79	80	124.11%	12954550	191.6	19.5	1270	0.174	0.01010
8	400	350	14.79	80	131.73%	13750501	191.6	19.5	1270	0.174	0.01010

B.6 Sub-cooled enthalpy effect on CHF (0 KJ/Kg →70 KJ/kg): 4bar, 124 kg/m^2-s, 80 ˚ of contact angle

# of	Pressure, Kpa	Mass flux, Kg/m2-s	sub-cooled enthalpy, KJ/Kg	contact angle	Ratio	Predicted CHF, W/m2	Hfg, KJ/Kg	lo,g	lo,f	cos(beta)	surf. Tension, N/m
1	400	124	0.00	80	100.00%	10127727	191.6	19.5	1270	0.174	0.01010
2	400	124	10.00	80	105.22%	10656314	191.6	19.5	1270	0.174	0.01010
3	400	124	20.00	80	110.44%	11184901	191.6	19.5	1270	0.174	0.01010
4	400	124	30.00	80	115.66%	11713488	191.6	19.5	1270	0.174	0.01010
5	400	124	40.00	80	120.88%	12242075	191.6	19.5	1270	0.174	0.01010
6	400	124	50.00	80	126.10%	12770662	191.6	19.5	1270	0.174	0.01010
7	400	124	60.00	80	131.32%	13299249	191.6	19.5	1270	0.174	0.01010
8	400	124	70.00	80	136.53%	13827836	191.6	19.5	1270	0.174	0.01010

B.7 Pressure effect on CHF (200 kPa →1200 kPa): 124 kg/m^2-s, 14.79 KJ/kg , 80 ˚ of contact angle

# of	Pressure, Kpa	Mass flux, Kg/m2-s	sub-cooled enthalpy, KJ/Kg	**contact angle**	**Ratio**	Predicted CHF, W/m2	Hfg, KJ/Kg	lo,g	lo,f	cos(beta)	surf. Tension, N/m
1	200	124	14.79	**80**	**100.00%**	9391483	206.02	10.01	1327	0.174	0.01303
2	400	124	14.79	**80**	**116.28%**	10920233	191.61	19.53	1264	0.174	0.01010
3	600	124	14.79	**80**	**125.09%**	11747558	180.89	29.16	1219	0.174	0.00854
4	700	124	14.79	**80**	**127.40%**	11964612	176.21	34.16	1200	0.174	0.00785
5	800	124	14.79	**80**	**128.51%**	12069256	171.81	39.03	1182	0.174	0.00724
6	900	124	14.79	**80**	**129.19%**	12132656	167.65	44.08	1165	0.174	0.00670
7	1000	124	14.79	**80**	**127.48%**	11972715	161.11	49.22	1149	0.174	0.00620
8	1200	124	14.79	**80**	**123.67%**	11614109	149.75	59.82	1119	0.174	0.00534

APPENDIX C: CHF prediction using Katto correlation

# of	pressure,kpa	surf.tension(N/m)	L/D	G(kg/m2s)	lo,g/lo,f	W	del_hi	Hfg	Min. value of qco	Max. value of K	qc(Katto),w/m2	CHF_Exp,w/m2	deviation,%
1	400	0.0101	8.5	124	0.015354	0.00772	14.79	213.5	0.011232239	1.285601634	382206	462951	-17.44
2	400	0.0101	8.5	248	0.015354	0.00193	14.54	214.6	0.006522182	1.513491037	525345	509282	3.15
3	400	0.0101	8.5	248	0.015354	0.00193	13.95	213.1	0.006522182	1.513491037	521575	498970	4.53
4	400	0.0101	8.5	248	0.015354	0.00193	12.76	213.2	0.006522182	1.513491037	521965	501252	4.13
5	400	0.0101	8.5	248	0.015354	0.00193	9.42	214.0	0.006522182	1.513491037	523850	491620	6.56
6	500	0.0093	8.5	124	0.019584	0.00695	22.93	221.4	0.011203678	1.291462652	397142	495425	-19.84
7	500	0.0093	8.5	186	0.019584	0.00309	23.20	221.9	0.008255669	1.337290316	455566	525567	-13.32
8	500	0.0093	8.5	248	0.019584	0.00174	22.02	221.1	0.006435101	1.517830954	535692	544685	-1.65
9	500	0.0093	8.5	186	0.019584	0.00309	21.02	222.4	0.008255669	1.337290316	456702	513183	-11.01
10	500	0.0093	8.5	186	0.019584	0.00309	13.94	222.2	0.008255669	1.337290316	456231	505413	-9.73
11	600	0.0084	8.5	124	0.024413	0.00612	30.67	230.3	0.011063737	1.298530081	410344	510625	-19.64
12	600	0.0084	8.5	186	0.024413	0.00272	30.51	231.4	0.008046669	1.344608533	465600	548506	-15.11
13	600	0.0084	8.5	248	0.024413	0.00153	28.35	230.4	0.00627219	1.537614787	551020	579069	-4.84
14	600	0.0084	8.5	186	0.024413	0.00272	28.13	231.1	0.008046669	1.344608533	465136	535199	-13.09
15	600	0.0084	8.5	186	0.024413	0.00272	22.02	230.2	0.008046669	1.344608533	463332	533354	-13.13
16	700	0.0078	8.5	124	0.028649	0.00563	35.87	236.4	0.010995455	1.303186289	419970	546207	-23.11
17	700	0.0078	8.5	186	0.028649	0.00250	36.49	235.8	0.007928736	1.349429967	469327	584638	-19.72
18	700	0.0078	8.5	248	0.028649	0.00141	35.88	237.2	0.006180264	1.547549761	562526	616157	-8.70
19	700	0.0078	8.5	186	0.028649	0.00250	35.89	236.1	0.007928736	1.349429967	469811	583294	-19.46
20	700	0.0078	8.5	186	0.028649	0.00250	29.14	237.0	0.007928736	1.349429967	471558	561116	-15.96
21	800	0.0072	8.5	186	0.033192	0.00228	43.70	243.8	0.007760785	1.354933919	476798	617047	-22.73
22	800	0.0072	8.5	186	0.033192	0.00228	38.68	242.7	0.007760785	1.354933919	474619	602688	-21.25
23	400	0.0101	8.5	124	0.015354	0.00772	17.00	213.9	0.011232239	1.285601634	382943	454938	-15.83
24	400	0.0101	8.5	186	0.015354	0.00343	15.53	212.9	0.008367387	1.331221319	441111	465120	-5.16
25	500	0.0093	8.5	124	0.019584	0.00695	26.31	223.5	0.011203678	1.291462652	400967	481098	-16.66
26	500	0.0093	8.5	186	0.019584	0.00309	25.01	221.8	0.008255669	1.337290316	455511	501414	-9.15
27	500	0.0093	8.5	186	0.019584	0.00309	21.59	221.9	0.008255669	1.337290316	455760	491944	-7.36
28	500	0.0093	8.5	186	0.019584	0.00309	16.50	223.5	0.008255669	1.337290316	458918	478443	-4.08
29	500	0.0093	8.5	186	0.019584	0.00309	24.38	221.216	0.008255669	1.337290316	454264	494291	-8.10
30	500	0.0093	8.5	248	0.019584	0.00174	24.57	223.9	0.006435101	1.517830954	542457	519917	4.34
31	600	0.0084	8.5	124	0.024413	0.00612	32.38	231.3	0.011063737	1.298530081	412037	505704	-18.52
32	600	0.0084	8.5	186	0.024413	0.00272	30.90	228.6	0.008046669	1.344608533	459999	530666	-13.32
33	600	0.0084	8.5	248	0.024413	0.00153	28.54	227.7	0.00627219	1.537614787	544688	544329	0.07
34	700	0.0078	8.5	124	0.028649	0.00563	38.84	237.3	0.010995455	1.303186289	421579	525858	-19.83
35	700	0.0078	8.5	186	0.028649	0.00250	36.31	237.3	0.007928736	1.349429967	472284	560809	-15.79
36	700	0.0078	8.5	248	0.028649	0.00141	37.24	237.0	0.006180264	1.547549761	562206	578179	-2.76

APPENDIX D: Empirical CHF correlation calculation

pressure, Bar	G,kg/m2	X,exit	delat Hi(Hf-Hi)	Measured CHF, Kw/m2	Predicted CHF by f(P,G,H)	Predicted CHF by f(P,G,H)
4	124	-0.0017	14.79	462.95	447.48	445.84
4	248	-0.0029	14.54	509.28	498.93	499.64
4	248	-0.0026	13.95	498.97	498.62	499.71
4	248	-0.0033	12.76	501.25	497.97	499.56
4	248	-0.0033	9.42	491.62	496.17	499.56
5	124	-0.0045	22.93	495.42	480.29	479.02
5	186	-0.0038	23.20	525.57	506.23	506.22
5	248	-0.0024	22.02	544.69	531.38	533.55
5	186	-0.0022	21.02	513.18	505.05	506.55
5	186	-0.0045	13.94	505.41	501.22	506.06
6	124	-0.0075	30.67	510.63	512.88	512.16
6	186	-0.0046	30.51	548.51	538.58	539.84
6	248	-0.0134	28.35	579.07	563.20	564.92
6	186	-0.0075	28.13	535.20	537.30	539.19
6	186	-0.0053	22.02	533.35	533.99	539.69
7	124	-0.012	35.87	546.21	544.09	544.98
7	186	-0.006	36.49	584.64	570.22	573.33
7	248	-0.0406	35.88	616.16	595.68	592.76
7	186	-0.0115	35.89	583.29	569.89	572.12
7	186	-0.0071	29.14	561.12	566.24	573.08
8	186	-0.0347	43.70	617.05	602.52	600.81
8	186	-0.0129	38.68	602.69	599.80	605.61
4	124	-0.003	17.00	454.94	448.68	445.54
4	186	-0.0008	15.53	465.12	473.68	473.08
5	124	-0.0067	26.31	481.10	482.12	478.53
5	186	-0.0029	25.01	501.41	507.21	506.41
5	186	-0.0004	21.59	491.94	505.35	506.95
5	186	-0.0029	16.50	478.44	502.60	506.41
5	186	-0.003	24.38	494.29	506.86	506.38
5	248	-0.0229	24.57	519.92	532.76	529.03
6	124	-0.0062	32.38	505.70	513.80	512.44
6	186	-0.0053	30.90	530.67	538.79	539.69
6	248	-0.039	28.54	544.33	563.31	559.29
7	124	-0.009	38.84	525.86	545.70	545.64
7	186	-0.0393	36.31	560.81	570.12	565.99
7	248	-0.0681	37.24	578.18	596.42	586.70